2019

Development of absorption-coefficient-based narrow-band model and its application to the calculation of radiative heat transfer in one and two-dimensional enclosures

Annette Fisher

DEVELOPMENT OF ABSORPTION-COEFFICIENT-BASED NARROW-BAND MODEL AND ITS APPLICATION TO THE CALCULATION OF RADIATIVE HEAT TRANSFER IN ONE- AND TWO-DIMENSIONAL ENCLOSURES

Annette Fisher

A DISSERTATION

Submitted in partial fulfillment of the requirements
for the degree of Doctor of Philosophy
in
The Department of Mechanical and Aerospace Engineering
to
The Graduate School
of
The University of Alabama in Huntsville
May 2019

Approved by:

Dr. Sarma Rani, Research Advisor and Committee Chair
Dr. Kader Frendi, Committee Member
Dr. Jason Cassibry, Committee Member
Dr. Sivaguru Ravindran, Committee Member
Dr. Babak Shotorban, Committee Member
Dr. Brent Webb, Committee Member
Dr. D. Keith Hollingsworth, Department Chair
Dr. Shankar Mahalingam, College Dean
Dr. Jon Hakkila, Graduate Dean

Abstract

DEVELOPMENT OF ABSORPTION-COEFFICIENT-BASED NARROW-BAND MODEL AND ITS APPLICATION TO THE CALCULATION OF RADIATIVE HEAT TRANSFER IN ONE- AND TWO-DIMENSIONAL ENCLOSURES

Annette S. Fisher

A dissertation submitted in partial fulfillment of the requirements for the degree of Doctor of Philosophy

The Department of Mechanical and Aerospace Engineering

The University of Alabama in Huntsville
May 2019

A narrow band model (NBM) with the absorption coefficient as the fundamental radiative property is investigated so that numerical solution methods compatible with the differential form of the radiative transfer equation (RTE) may be employed. The advantage of a NBM based on the absorption coefficient rather than the transmissivity is that the expression for the mean absorption coefficient is independent of the functional form of the probability density function for spectral line intensities, $\boldsymbol{P(S)}$. Accordingly, it is seen that the narrow-band mean absorption coefficient $\overline{\boldsymbol{\kappa}}_{\boldsymbol{\eta}} = \frac{\overline{\boldsymbol{S}}}{\boldsymbol{d}}$, where $\overline{\boldsymbol{S}}$ and $\boldsymbol{d}$ are the mean line intensity and mean line spacing, respectively, consists of a narrow band. The mean absorption coefficient $\overline{\boldsymbol{\kappa}}_{\boldsymbol{\eta}}$ may be directly used in solving the differential RTE without having to specify a path length. Two approaches were considered for obtaining the ratio of $\overline{\boldsymbol{S}}$ and $\boldsymbol{d}$. The first, referred to here as NBM with EM2C data, involves using $\frac{\overline{\boldsymbol{S}}}{\boldsymbol{d}}$ values tabulated in the EM2C narrow-band property database. In the second approach,

denoted as NBM with spectral averaging, $\bar{\kappa}_\eta$ is evaluated by directly averaging the line-by-line absorption coefficients over the narrow band. Accuracy of the two NBM approaches is investigated through comparison with three other methods for calculating spectral radiative properties: (1) line-by-line (LBL) calculations that serve as the benchmark, with the spectral absorption coefficients obtained from the HITEMP 2010 database, (2) spectral line-based weighted sum of gray gases (SLW) method, and (3) wavenumber-selective line-by-line (WS-LBL) calculations wherein the absorption coefficients are directly picked from the LBL spectrum at discrete wavenumbers separated by an interval equal to the width of the narrow band. The five spectral approaches — NBM with EM2C data, NBM with spectral averaging, LBL, SLW, and WS-LBL — are applied to compute the radiative fluxes and flux divergences in a number of 1-D and 2-D non-gray enclosures. The enclosure cases were chosen to study the effects of medium optical depth, as well as inhomogeneities in medium temperature and species concentrations, on the accuracy of the narrow band models.

Acknowledgements

First, I would like to sincerely thank my advisor, Dr. Sarma L. Rani, for his guidance and mentorship, and for allowing me to be his student. Dr. Rani is an extraordinary advisor with remarkable intelligence, ingenuity in problem solving, and a genuine desire to see each of his students succeed. I am forever grateful to have Dr. Rani as my advisor and mentor.

I would also like to thank my dissertation committee, Dr. Kader Frendi, Dr. Jason Cassibry, Dr. Babak Shotorban, Dr. Sivaguru Ravindran, and Professor Brent Webb. Each committee member offered expert guidance and encouragement throughout my academic studies. I am especially grateful for Professor Webb at BYU for his willingness to meet with me, provide valuable insight, and give his amazing support and encouragement in my research.

I want to thank my friends that have offered continuous encouragement, support, and guidance along the journey. Without them, I would not have made it this far.

Finally, none of this would be possible without the love and support from my family, especially Charlie and Lucy, who offered continuous, unwavering support. Most of all, I am especially grateful for my husband, David, who has supported and encouraged me to achieve anything I wanted to, even the challenge of getting a Ph.D. He makes me a better person everyday and I could not have done this without him.

Lastly, I am grateful to God for all the blessings He has given me in this life.

To David

Table of Contents

List of Figures

List of Tables

Chapter 1. Absorption Coefficient-Based Narrow Band Model and Its Application to the Calculation of Radiative Heat Transfer in One-Dimensional Enclosures

1.1 Introduction

Radiative heat transfer is a key component of the thermal energy balance in applications ranging from atmospheric processes to combustion systems. Modulation of solar radiation in the atmosphere plays an essential role in regulating earth's energy budget [1]. Radiative transfer is an important mechanism driving the spread of wildfires upon the ignition of combustible fuels [2]. In propulsion systems, accounting for radiation from the hot combustion gases is crucial to accurately determining the flame temperature, as well as to calculating the overall thermal load on combustor walls [3]. Radiative intensity field in a gaseous medium is a strong function of the optical properties of the medium, principally the spectral absorption coefficient κ_η or the spectral transmissivity τ_η. The most accurate way to calculate κ_η or τ_η is from the detailed line structure of the gas absorption/emission spectrum, referred to as the line-by-line (LBL) method. However, in most practical (2-D and 3-D) problems, the LBL method is computationally prohibitive, motivating the development of approximate spectral models for gas radiative properties. Gas radiation is also a key mode of heat transfer in high-temperature industrial systems such as furnaces and gas burners [4]. In the current study, a narrow band model (NBM) with the absorption coefficient as the fundamental radiative property is

investigated. Such an NBM facilitates the application of numerical methods suitable for solving the differential form of the radiative transfer equation (RTE).

Computational modeling of radiative transport entails two principal steps. The first step is to develop a numerical solution methodology for the RTE, as exact analytical solutions to the RTE can only be derived for simple 1-D enclosures without scattering. The second and critical step in modeling radiative transport is the specification of spectral radiative properties of the participating medium that are inputs to the RTE. To this end, one resorts to spectral approaches such as the line-by-line (LBL) method or spectral models such as the band models. In the LBL approach, the absorption coefficients (or transmissivities) are calculated for each of the spectral lines in a spectroscopic property database such as the HITRAN, HITEMP and CDSD databases [5]. The RTE, in conjunction with the spectral property model, is then solved for the radiative intensities, which are then used to calculate the radiative fluxes and source terms.

The LBL absorption coefficients calculated from the spectroscopic databases vary rapidly and randomly as a function of wavelength (or wavenumber). Further, the LBL spectrum of a species may comprise hundreds of thousands to millions of lines. For example, the HITRAN database [6] contains several hundred-thousand absorption lines for CO_2, whereas the more recent HITEMP 2010 database [7] contains more than 11 million lines for CO_2. These attributes of the gas absorption spectra — the extreme wavenumber dependency and the large number of spectral lines — make LBL calculations of radiative heat transfer severely computationally intensive and essentially impractical except for simple 1-D enclosures. This has

motivated the development of approximate spectral models, which may be broadly classified into three types [8]: (1) narrow band models (NBMs); (2) wide band models (WBMs); and (3) global models. The NBMs involve averaging the gas absorption spectrum over a "narrow" range of wavenumbers within a band, while WBMs perform averaging over an entire vibration-rotation band. In global models, broadly speaking, the LBL spectrum is replaced by the cumulative distribution function of a small number of absorption coefficient values.

The conceptual basis for developing a NBM is that in a sufficiently narrow wavenumber range, the Planck function for the blackbody spectral intensity does not vary appreciably [8]. Accordingly, when the RTE is averaged over a narrow band, the mean emission term may be approximated as $\overline{\kappa_\eta I_{b\eta}} \approx \bar{\kappa}_\eta \overline{I_{b\eta}}$, where $\bar{\kappa}_\eta$ is the mean absorption coefficient over the narrow band, and $\overline{I_{b\eta}}$ is the mean spectral blackbody intensity. Among the well-known narrow band models are the Elsasser NBM [9], Goody NBM [10], and the Malkmus NBM [11]. The Elsasser NBM is a deterministic model since it assumes that all spectral lines in a narrow band are equally spaced and have the same intensity. Both approximations are dispensed with in the Goody and Malkmus narrow band models. Specifically, the line intensities S are regarded as random variables characterized by a probability density function (PDF), $P(S)$. As a result, the Goody and Malkmus models are known as statistical NBMs. In the Goody NBM, $P(S)$ has an exponential distribution, whereas in the Malkmus NBM, $P(S)$ is considered to be an exponential-tailed $1/S$ distribution.

The Elsasser, Goody and Malkmus NBMs regard the narrow band transmissivity as the fundamental radiative property, and *not* the narrow band absorption coefficient.

Consequently, these NBMs are inherently suited to solving the RTE in its integral form. Applying these models when solving the differential RTE would require that an equivalent absorption coefficient be calculated from transmissivity, which, in turn, would entail the specification of a mean beam length. However, the beam length is not a naturally defined length scale when solving the RTE in its differential form. As a result, coupling these NBMs with the differential RTE would introduce significant uncertainty into the radiative intensity calculations (through the arbitrariness of the beam length). Furthermore, the expressions for narrow-band transmissivities differ dramatically based on the form of $P(S)$ assumed to characterize line intensity distribution.

The fundamental principle underlying the development of transmissivity-based NBMs is the approximation of the true line spectrum by a modeled arrangement of spectral lines in a narrow band of width $\Delta\eta$. An alternative approach based on using the true absorption coefficient spectrum gives rise to models referred to as the mean absorption coefficient methods. In these methods, one begins by spectrally integrating the RTE over a narrow band. The radiative energy loss due to gas absorption in the RTE then becomes $\kappa_{\eta,a}\,\bar{I}_\eta$, where the overbar denotes averaging over a narrow band of width $\Delta\eta$ and $\kappa_{\eta,a}$ is the radiation-intensity-weighted absorption coefficient, given by

$$\kappa_{\eta,a} = \frac{\int_{\Delta\eta}\kappa_\eta I_\eta\, d\eta}{\int_{\Delta\eta} I_\eta\, d\eta} = \frac{\overline{\kappa_\eta I_\eta}}{\bar{I}_\eta} \quad . \tag{1.1}$$

Chien [12] developed a model for $\kappa_{\eta,a}$ by substituting into equation (1.1) the exact analytical solution to the non-scattering RTE, and then approximating the variation in κ_η with pathlength using a truncated Taylor series expansion. The integrals over path length that then arise in $\kappa_{\eta,a}$ were evaluated by numerical quadrature. The final expression for $\kappa_{\eta,a}$ contained band properties such as the total-band absorptance A and total-band

intensity S, which are functions of the local thermodynamic state and path length. In Chien [12], both A and S were evaluated using the exponential wide-band model parameter quantified by Edwards [13]. The weighted absorption coefficient $\kappa_{\eta,a}$ in equation (1.1) should be distinguished from the mean absorption coefficient $\bar{\kappa}_\eta$ in a band of width $\Delta\eta$, defined as

$$\bar{\kappa}_\eta = \frac{1}{\Delta\eta}\int_{\Delta\eta} \kappa_\eta \, d\eta \quad . \tag{1.2}$$

The distinction arises because when the RTE is spectrally averaged over a narrow band, *i.e,*. $\frac{1}{\Delta\eta}\int_{\Delta\eta}(\text{RTE})d\eta$, the gas emission and absorption terms become $\bar{\kappa}_\eta\overline{I_{b\eta}}$ and $-\kappa_{\eta,a}\,\overline{I_\eta}$, respectively. In Section 1.3, it is shown, from first principles, that $\bar{\kappa}_\eta \approx \frac{\bar{S}}{d}$, where $\bar{S}$ and d are the mean line intensity and mean spacing of a narrow band, respectively. This expression for $\bar{\kappa}_\eta$ was earlier obtained by André and Vaillon [14] in their narrow band $k-$moment method for nonuniform gaseous paths and may also be found in Young [15].

André and Vaillon [14] developed the $k-$moment method for the narrow band modeling of radiative intensities in inhomogeneous non-isothermal media. As in transmissivity-based NBMs, the $k-$moment NBM too considers the transmissivity form of the RTE, which when averaged over a spectral interval $\Delta\eta$ gives

$$\bar{I}_\eta(s) = \bar{I}_{b\eta}(0)\,\bar{\zeta}_\eta(0,s) + \int_0^s \bar{I}_{b\eta}(s')\,\frac{\partial\bar{\zeta}_\eta(s',s)}{\partial s'}\,ds' \,, \tag{1.3}$$

where $\bar{\zeta}_\eta(s',s)$ is the narrow-band spectral average of the transmission function of the gas path between s' and s, given by

$$\bar{\zeta}_\eta(s',s) = \frac{1}{\Delta\eta}\int_{\Delta\eta}\exp\left[-\int_{s'}^{s}\kappa_\eta(\tilde{s})\,d\tilde{s}\right]d\eta \quad . \tag{1.4}$$

To model $\bar{\zeta}_\eta(s', s)$, André and Vaillon perform a series expansion of $\exp\left[-\int_{s'}^{s} \kappa_\eta(\tilde{s})\, d\tilde{s}\right]$. In this expansion, excepting the first term (which is unity), the rest of the terms contain increasing order moments of the path-averaged absorption coefficient. To develop closures for the absorption coefficient moments, the spectral absorption coefficients are written as the sum of the contributions of N Lorentz lines. In the second (and higher moments), the pathlength and spectral dependencies of the Lorentz line parameters are assumed separable when evaluating the integrals. In fact, the first moment gives us the aforementioned result $\bar{\kappa}_\eta \approx \frac{\bar{S}}{d}$.

In the current study, an absorption-coefficient-based NBM that is compatible with numerical solution methods for the differential RTE is investigated. It is shown that a generalized NBM, independent of the functional form of $P(S)$, may be obtained by considering the absorption coefficient as the basic radiative property. The mean line-intensity to mean line-spacing ratio needed to compute the mean absorption coefficient $\bar{\kappa}_\eta$ is obtained using two approaches — from the EM2C database, and by averaging the LBL spectrum over the narrow band. Two NBM forms with three RTE solution methods are coupled, namely the Discrete Ordinates Method (DOM) [8], Control-Angle Discrete Ordinates Method (CA-DOM) [16], as well as the 1-D exact analytical solution where available. Both DOM and CA-DOM are well-established numerical methods that are based on the discretization of directional space at a given spatial location, while the exact solution allows us to evaluate the accuracy of DOM and CA-DOM. To study the predictive capabilities of the current NBM, three additional spectral approaches are considered, *i.e.*, LBL calculations, the spectral line weighted sum of gray gases (SLW) method, and a wavenumber-selective LBL (WS-

LBL) method. The LBL calculations serve as the reference for evaluating the accuracy of all other spectral models. The WS-LBL method involves selecting absorption coefficients from the LBL spectrum at discrete wavenumbers separated by the same interval as the narrow-band width. The three RTE solution methods coupled with the five spectral approaches are applied to calculate radiative transfer in 1-D enclosures containing CO_2, or H_2O, or a mixture of the two species.

The organization of this paper is as follows. Section 1.2 presents the derivation of the absorption-coefficient-based NBM, as well as a discussion of the two NBM forms. The steps for calculating the LBL absorption coefficients from the HITEMP 2010 database are outlined in Section 1.3. The SLW method for solving the non-gray RTE is presented in Section 1.4. In Section 1.5, the three solution methods for the RTE are discussed. Section 1.5.1 presents the exact solution for a 1-D plane-parallel medium. Section 1.5.2 outlines the 1-D DOM method, while Section 1.5.3 summarizes the CA-DOM method. Results obtained for the various 1-D enclosures considered are presented in Section 1.6. Finally, the Conclusions section summarizes the study.

1.2 Narrow-Band Model Formulation

The radiative transfer equation for a non-scattering medium is [8]

$$\frac{dI_\eta}{ds} = \kappa_\eta I_{b\eta} - \kappa_\eta I_\eta \ , \tag{1.5}$$

where $I_\eta(s)$ is the spectral and directional radiative intensity, η is the wavenumber, s is the path length along a given direction, $I_{b\eta}$ is the spectral (and diffuse) blackbody intensity, and κ_η is the spectral absorption coefficient of the participating medium. Averaging the RTE over a narrow band of width $\Delta\eta$, provides

$$\frac{d\overline{I_\eta}}{ds} \approx \bar{\kappa}_\eta \overline{I_{b\eta}} - \bar{\kappa}_\eta \overline{I_\eta} \quad , \tag{1.6}$$

where $I_{b\eta}$ varies slowly over $\Delta\eta$, as compared to κ_η and I_η, allowing us to write $\overline{\kappa_\eta I_{b\eta}} \approx \bar{\kappa}_\eta \overline{I_{b\eta}}$. More significantly, $\overline{\kappa_\eta I_\eta} \approx \bar{\kappa}_\eta \overline{I_\eta}$, with the implication that the correlation of fluctuations in κ_η and I_η over a narrow band has been neglected. It will be shown in a subsequent analysis that the optical depth of the medium has a strong effect on the accuracy of this approximation. Insights from the optical depth analysis are confirmed numerically by comparing the NBM predictions of radiative fluxes and source terms (flux divergences) with the results from LBL and WS-LBL calculations. In the WS-LBL approach, the spectral absorption coefficients are picked from the LBL spectrum at discrete wavenumbers separated by the same interval as the narrow-band width $\Delta\eta$. However, as WS-LBL does not involve averaging the RTE, the term containing the correlation of κ_η and I_η does not arise. Thus, the WS-LBL calculations may be regarded as a spectrally coarse form of LBL calculations, but with the same resolution as that of the NBM, thereby providing an efficient means to evaluate the effects of neglecting the correlation of fluctuations in κ_η and I_η. Next, the accuracy of the approximation $\overline{\kappa_\eta I_\eta} \approx \bar{\kappa}_\eta \overline{I_\eta}$ in optically thick and optically thin media will be analyzed.

1.2.1 NBM in an Optically Thick Medium

The exact analytical solution to the RTE (1.5) in a non-scattering medium is

$$I_\eta\left(\tau_\eta(s)\right) = I_{b\eta}(0)\, e^{-\tau_\eta} + \int_0^{\tau_\eta} I_{b\eta}\left(\tilde{\tau}_\eta\right)\, e^{-(\tau_\eta - \tilde{\tau}_\eta)}\, d\tilde{\tau}_\eta \tag{1.7}$$

$$\tau_\eta(s) = \int_0^s \kappa_\eta(\tilde{s})\, d\tilde{s} \quad . \tag{1.8}$$

In an optically thick layer with $\tau_\eta(s) \gg 1$, the integral (second term) on the right-hand side (RHS) of equation (1.7) becomes $\ll 1$ when $\tilde{\tau}_\eta$ deviates even by a small amount

from $\tilde{\tau}_\eta = \tau_\eta$. Therefore, this integral may be well approximated by evaluating it for $\tilde{\tau}_\eta$ such that $\xi = (\tau_\eta - \tilde{\tau}_\eta) \ll 1$. Writing $I_{b\eta}(\tilde{\tau}_\eta) = I_{b\eta}(\tau_\eta - \xi)$, and performing a Taylor-series expansion about τ_η, providing

$$I_{b\eta}(\tilde{\tau}_\eta) = I_{b\eta}(\tau_\eta) - \frac{dI_{b\eta}}{d\tau_\eta}\,\xi + O(\xi^2) \quad . \tag{1.9}$$

Substituting equation (1.9) into (1.7) yields

$$I_\eta(\tau_\eta) \approx I_{b\eta}(0)\, e^{-\tau_\eta} + I_{b\eta}(\tau_\eta) \int_0^{\tau_\eta} e^{-\xi}\, d\xi - \frac{dI_{b\eta}}{d\tau_\eta} \int_0^{\tau_\eta} \xi e^{-\xi}\, d\xi \quad . \tag{1.10}$$

In an optically thick domain, for locations far away from the boundary with $\tau_\eta(s) \gg 1$, the upper limits of the integrals on the RHS of equation (1.10) may be changed from τ_η to ∞. With the change in limits, the integrals in (1.10) can be evaluated exactly, yielding

$$I_\eta(\tau_\eta) \approx I_{b\eta}(0)\, e^{-\tau_\eta} + I_{b\eta}(\tau_\eta) - \frac{dI_{b\eta}}{d\tau_\eta} \tag{1.11}$$

multiplying with κ_η and averaging over a narrow band, providing

$$\overline{\kappa_\eta I_\eta} = \overline{I_{b\eta}}(0)\, \overline{\kappa_\eta e^{-\tau_\eta}} + \bar{\kappa}_\eta \overline{I_{b\eta}}(s) - \bar{\kappa}_\eta \frac{d\overline{I_{b\eta}}}{d\tau_\eta} \quad . \tag{1.12}$$

In arriving at equation (1.12), the approximation that analogous to $I_{b\eta}$ is used, $\frac{dI_{b\eta}}{d\tau_\eta}$ is also a weak function of wavenumber η (relative to the extreme wavenumber dependence of κ_η). The first term on the RHS of (1.12) contains $\overline{\kappa_\eta e^{-\tau_\eta}}$ that can be further resolved as

$$\overline{\kappa_\eta e^{-\tau_\eta}} \approx \frac{1}{s}\overline{\tau_\eta e^{-\tau_\eta}} = \frac{1}{s}\overline{(\bar{\tau}_\eta + \tau'_\eta) e^{-\tau_\eta}} \approx \frac{1}{s}\bar{\tau}_\eta \overline{e^{-\tau_\eta}} = \bar{\kappa}_\eta\, \overline{e^{-\tau_\eta}} \quad ,$$

where τ'_η is the fluctuation in optical thickness ($\kappa_\eta = \frac{\tau_\eta}{s}$ is exact for a homogeneous and isothermal medium). Since $\tau_\eta(s) \to \infty$, τ'_η may be regarded to be smaller than $\bar{\tau}_\eta$, $\overline{\tau'_\eta e^{-\tau_\eta}}$ may be dropped. Equation (1.12) can now be written as

$$\overline{\kappa_\eta I_\eta} \approx \overline{I_{b\eta}}(0)\, \bar{\kappa}_\eta\, \overline{e^{-\tau_\eta}} + \bar{\kappa}_\eta \overline{I_{b\eta}}(s) - \bar{\kappa}_\eta \frac{d\overline{I_{b\eta}}}{d\tau_\eta} = \bar{\kappa}_\eta \bar{I}_\eta \tag{1.13}$$

demonstrating that the approximation $\overline{\kappa_\eta I_\eta} \approx \bar{\kappa}_\eta \bar{I}_\eta$ is reasonable in an optically thick domain.

1.2.2 NBM in an Optically Thin Medium

Referring to equation (1.7), in an optically thin medium with $\tau_\eta(s) \ll 1$, $(\tau_\eta - \tilde{\tau}_\eta) < \tau_\eta$ with $e^{-(\tau_\eta - \tilde{\tau}_\eta)}$ very nearly equal to unity. Therefore, equation (1.7) now becomes

$$I_\eta\left(\tau_\eta(s)\right) = I_{b\eta}(0)\, e^{-\tau_\eta} + \int_0^{\tau_\eta} I_{b\eta}\left(\tilde{\tau}_\eta\right)\, d\tilde{\tau}_\eta \quad . \tag{1.14}$$

Multiplying equation (1.14) with κ_η and averaging over a narrow band gives us

$$\begin{aligned} \overline{\kappa_\eta I_\eta} &\approx \overline{I_{b\eta}}(0)\, \overline{\kappa_\eta e^{-\tau_\eta}} + \bar{\kappa}_\eta \int_0^{\tau_\eta} \overline{I_{b\eta}}\left(\tilde{\tau}_\eta\right)\, d\tilde{\tau}_\eta \\ &\approx \overline{I_{b\eta}}(0)\, \bar{\kappa}_\eta\, \overline{e^{-\tau_\eta}} + \bar{\kappa}_\eta \int_0^{\tau_\eta} \overline{I_{b\eta}}\left(\tilde{\tau}_\eta\right)\, d\tilde{\tau}_\eta = \bar{\kappa}_\eta \bar{I}_\eta \quad , \end{aligned} \tag{1.15}$$

where it employed the approximation $\overline{\kappa_\eta e^{-\tau_\eta}} \approx \bar{\kappa}_\eta\, \overline{e^{-\tau_\eta}}$, whose accuracy depends on whether $\overline{\kappa'_\eta e^{-\tau_\eta}}$ is small or not. It can be postulated that the smoother the spectrum of κ_η, the smaller the magnitude of κ'_η and thereby that of $\overline{\kappa'_\eta e^{-\tau_\eta}}$. One way to make the κ_η spectrum smooth is to consider higher temperatures so that the spectral lines are both broader due to the thermal Doppler effect and more numerous due to the greater number of excited quantum states and transitions. To investigate the validity of this postulate, the accuracy of the NBM will be compared in domains with a given size but differing gas temperatures.

1.2.3 Narrow-Band Mean Absorption Coefficient

Consider a narrow band of width $\Delta\eta$ centered at the wavenumber η and comprising N spectral lines with mean line-spacing d. The mean absorption coefficient over the narrow band, $\bar{\kappa}_\eta$, is defined as [8, 10]:

$$\bar{\kappa}_\eta = \frac{1}{\Delta\eta}\int_0^\infty \int_0^\infty \cdots \int_0^\infty P(S_1)P(S_2)\cdots P(S_N)\, dS_1 dS_2 \cdots dS_N \int_{\eta-\frac{\Delta\eta}{2}}^{\eta+\frac{\Delta\eta}{2}} \kappa_\eta(S_1, S_2, \cdots, S_N)\, d\eta \ , \tag{1.16}$$

where S_i with $i = 1, 2, \cdots$, and N are the intensities of the N lines contained in the narrow band. The line intensities S_i are considered to be independent random variables [10], allowing us to express their joint PDF as the product of the PDFs of individual line intensities $P(S_i)$. In equation (1.16), $P(S_i)\, dS_i$ represents the probability that the intensity of the ith spectral line lies in the range $[S_i, S_i + dS_i)$. The net absorption coefficient κ_η at the wavenumber η due to contributions from the N lines in a narrow band is given by [8]

$$\kappa_\eta(S_1, S_2, \cdots, S_N) = \sum_{i=1}^{N} \frac{S_i}{\pi} \frac{\gamma_L}{(\eta_i - \eta)^2 + \gamma_L^2} \ , \tag{1.17}$$

where η_i is the wavenumber at which the ith line is located and γ_L is the Lorentz broadening term. The PDF of the intensity of the ith line, $P(S_i)$, can be assumed to have one of a number of functional forms that were considered in prior NBMs [9, 10]. For instance, in the Goody NBM [10], $P(S_i)$ is exponentially distributed as

$$P(S_i) = \frac{1}{\bar{S}} \exp\left(-\frac{S_i}{\bar{S}}\right) \tag{1.18}$$

with $\bar{S}$ being the mean line intensity of the narrow band. In the Malkmus NBM, $P(S_i)$ has an exponential-tailed $1/S$ distribution, given by [10]

$$P(S_i) = \frac{1}{\ln(R)}\frac{1}{\bar{S}}\left[\exp\left(-\frac{(R-1)}{\mathrm{R}\ln(R)}\frac{S_i}{\bar{S}}\right) - \exp\left(-\frac{(R-1)}{\ln(R)}\frac{S_i}{\bar{S}}\right)\right] \quad , \tag{1.19}$$

where the terms involving R were introduced by Malkmus so that the PDF satisfies the following two normalization criteria:

$$\int_0^\infty P(S_i)\, dS_i = 1 \tag{1.20}$$

$$\int_0^\infty S_i\, P(S_i)\, dS_i = \bar{S} \ . \tag{1.21}$$

Both the Goody and Malkmus NBMs assume the lines in a narrow band to have the same PDF. Substituting (1.17) into (1.16) and utilizing either the Goody PDF (1.18) or the Malkmus PDF (1.19) yields

$$\bar{\kappa}_\eta = \frac{N}{\Delta\eta}\frac{\bar{S}\ tan^{-1}\frac{\Delta\eta}{2\gamma_L}}{\left(\frac{\pi}{2}\right)} \ . \tag{1.22}$$

The advantage of equation (1.22) is that any normalized PDF $P(S_i)$ would yield an identical expression for $\bar{\kappa}_\eta$. Considering a narrow band of thickness 25 cm^{-1} the ratio $\frac{\Delta\eta}{2\gamma_L} \sim O(100-1000)$ can be calculated for CO_2 and H_2O so that $\bar{\kappa}_\eta \approx \frac{\bar{S}}{d}$, where $d = \frac{\Delta\eta}{N}$ is the mean line spacing of the narrow band.

Two approaches were adopted to calculate the narrow-band mean absorption coefficient $\bar{\kappa}_\eta = \frac{\bar{S}}{d}$. The first is based on using the narrow-band properties generated by Soufiani, Taine, Riviere and coworkers at the EM2C Laboratory [17, 18, 19]. In the second approach, $\bar{\kappa}_\eta$ can be calculated by averaging the LBL absorption coefficients in a narrow band of width $\Delta\eta$. The EM2C database was developed to provide the narrow-band parameters needed to calculate the transmissivities in the Malkmus NBM. Among the tabulated parameters in this database is the ratio of the mean line intensity to mean spacing, $\frac{\bar{S}}{d}$, which is utilized in the current study. It may be noted that for a given species,

the EM2C properties were tabulated only as a function of temperature, and not of species mole fraction. The initial versions of the EM2C database were obtained using HITRAN [6], but the more recent versions were generated based on HITEMP 2010 [7].

1.3 Line-By-Line (LBL) Absorption Coefficient Calculations

In the study, LBL absorption coefficients κ_η of H_2O and CO_2 were obtained using the HITEMP 2010 spectroscopic database. Calculation of κ_η from HITEMP 2010 involves a number of steps [5], the most important of which are outlined in the following discussion. The key inputs to κ_η are the absorption cross-sections of the individual spectral lines in the database. The absorption cross-section of the jth spectral line, $C_{\eta,j}$ is a function of wavenumber η, total pressure p, temperature T, and mole fraction Y_i of species i. For both H_2O and CO_2, $C_{\eta,j}$ is generated for spectral lines in the wavenumber range 0.005 cm^{-1} to 25000 cm^{-1}, at an interval of 0.005 cm^{-1}. In calculating $C_{\eta,j}$, the Voigt line profile was considered that combines the effects of both Lorentz and Doppler broadening, as follows [8]:

$$C_{\eta,j}(p,T,Y_i) = \frac{S_j(p,T)\gamma_{L,j}(p,T)}{\pi^{3}/_{2}} \times \int_{-\infty}^{\infty} \frac{e^{-x^2}dx}{\left[\eta-\eta_{0,j}(p)-\left(\frac{x\gamma_{D,j}(p,T)}{\sqrt{ln}}\right)\right]^2+\gamma^2{}_{L,j}(p,T)} \tag{1.23}$$

$$x = \nu\sqrt{M_i/_{2kT}} \quad , \tag{1.24}$$

where $S_j(p,T)$ is the line intensity, $\eta_{0,j}(p)$ is the center of the jth line at vacuum conditions, $\gamma_{L,j}(p,T)$ is the line half-width at half-maximum due to Lorentz broadening, $\gamma_{D,j}(p,T)$ is the line half-width at half-maximum due to Doppler broadening, T is the gas temperature, M_i is the molecular mass of species i, and k is the Boltzmann's constant.

The Lorentz broadening half-width $\gamma_{L,j}$ is calculated as [5, 8, 20]

$$\gamma_{L,j}(p,T) = p\left(\frac{T_0}{T}\right)^{n_{air}}\left[\gamma_{air}(1-Y_i)+\gamma_{self}Y_i\right] \ , \tag{1.25}$$

where n_{air} is the coefficient of temperature dependence for air-broadening, and γ_{air} and γ_{self} are the line half-widths at half-maximum for air-broadening and self-broadening, respectively. These parameters were obtained from HITEMP 2010. The Doppler broadening is calculated from [8] as:

$$\gamma_{D,j}(p,T) = \frac{\eta_0}{c}\sqrt{\frac{2kT}{M_i}ln2} \tag{1.26}$$

and the line intensity S_j is obtained using

$$S_j(p,T) = S(T_0)\frac{Q(T_0)}{Q(T)}exp\left[\frac{hcE''}{k}\left(\frac{1}{T_0}-\frac{1}{T}\right)\right]\frac{1-exp\left[-hc\eta_0/kT\right]}{1-exp\left[-hc\eta_0/kT_0\right]} \ , \tag{1.27}$$

where Q is the internal partition function of the absorbing gas, E'' is the lower state energy of the transition, h is the Planck constant, c is the speed of light in a vacuum, $T_0 = 296$ K is the reference gas temperature, and k is the Boltzmann's constant. These inputs to the line intensity S_j are also obtained from HITEMP 2010.

The effective absorption cross-section C_η at the wavenumber η is then obtained by summing the contributions of all spectral lines, as follows:

$$C_\eta(p,T,Y_i) = \sum_{j=1}^{N} C_{\eta,j}(p,T,Y_i) \ , \tag{1.28}$$

where N is the total number of lines in the HITEMP database. The absorption coefficient is now calculated using

$$\kappa_\eta(p,T,Y_i) = (pN_A/R_uT)Y_iC_\eta \ , \tag{1.29}$$

where N_A is Avogadro's number, R_u is the universal gas constant, and Y_i is the mole fraction of species i. It may be noted that $C_{\eta,j}$ has a strong dependence on mole fraction Y_i for H_2O, but only a weak dependence on Y_i for CO_2. The effects of Y_i on $C_{\eta,j}$ are

therefore neglected for CO_2 (this can be achieved by setting $Y_i = 0$ for CO_2 in equation (1.25). However, for both H_2O and CO_2, Y_i is included in equation (1.29) for calculating κ_η.

1.4 SLW Method

1.4.1 Isothermal and Homogeneous Media

The classical SLW method, developed by Denison and Webb [21, 22], is a global spectral method for predicting radiative transfer in isothermal, homogeneous media. The fundamental idea of the SLW method is to replace the spectral radiative intensities I_η by a small number of aggregate intensities I_j. Each I_j is obtained by first integrating I_η over all such wavenumber intervals wherein the spectral absorption cross-section lies between two prescribed values of absorption cross-section, and next summing all the integrated intensities.

The spectral absorption cross-section C_η and absorption coefficient κ_η are related through $\kappa_\eta = NYC_\eta(Y, T, p)$, where Y is the species mole fraction, and N, T and p are the gas molar density, temperature and total pressure, respectively. In the SLW method, a set of supplemental absorption cross-sections $\{\tilde{C}_0, \tilde{C}_1, \dots, \tilde{C}_n\}$ are chosen, where $\tilde{C}_0$ and $\tilde{C}_n$ are the minimum and maximum cross-section values. The gray-gas absorption cross-sections $C_j, j = 1,2, \dots, n$, are then selected such that $\tilde{C}_{j-1} < C_j < \tilde{C}_j$, for example, $C_j = \sqrt{\tilde{C}_{j-1}\,\tilde{C}_j}$. In an isothermal, homogeneous domain, the gray-gas absorption coefficients are related to the C_j's as $\kappa_j = NYC_j$. Thus, the C_η spectrum, comprising a large number of randomly oscillating spectral lines, is replaced by a smooth histogram with a much smaller number

of C_j's. The histogram is referred to as the absorption line blackbody distribution function (ALBDF). The ALBDF, $F(C_j, p, T, T_b, Y)$, quantifies the fraction of the blackbody body emissive power ($E_b = \sigma T_b^4$) contained in the wavenumber ranges where the spectral cross-section C_η at the gas temperature is below a prescribed C_j [22, 23, 24]. It is expressed as

$$F(C_j, p, T, T_b, Y) = \frac{1}{\sigma T_b^4} \int_{\{\eta:\, C_\eta(p,T,Y) \le C_j\}} E_{b\eta}(T_b, \eta) d\eta \ . \tag{1.30}$$

The RTE for the aggregate intensity I_j of the jth gray gas in a homogeneous, isothermal medium is then given by [21]

$$\frac{d}{ds} I_j(s) = -\kappa_j I_j(s) + a_j \kappa_j I_b(T) \ , \tag{1.31}$$

where κ_j is the absorption coefficient of the jth gray gas, a_j is the corresponding blackbody weight, and $I_b = \frac{\sigma T^4}{\pi}$ is the diffuse blackbody emissive power [5, 25]. The blackbody weight a_j is calculated from the ALBDF of two neighboring supplementary cross-sections as [13]

$$a_j = F(\tilde{C}_j, p_g = p, T_g = T, Y, T_b = T) - F(\tilde{C}_{j-1}, p_g = p, T_g = T, Y, T_b = T) \ , \tag{1.32}$$

where $j = 1,2, \dots, n$, T_g is the gas temperature, T_b is the blackbody temperature and T is the medium temperature.

1.4.2 Non-Isothermal and Inhomogeneous Media

Denison and Webb [22] extended the SLW method to media with spatial inhomogeneities in gas temperature, pressure and species concentrations. The modified method, referred to as the SLW reference approach, is fundamentally based on the assumption that the absorption cross-section is separable as $C_\eta(p, T, Y_s) =$

$\phi(p, T, Y_s)\,\psi(\eta)$. The implication of this equation is that the absorption cross-section spectrum of a given species has the same spectral dependence irrespective of the thermodynamic state of the medium. The key steps in the modified SLW method are as follows.

1. Reference temperature T_{ref}, reference total pressure $p_{T,\text{ref}}$, and references species mole fraction $Y_{s,\text{ref}}$ are determined by spatially averaging the respective variables over the entire domain.
2. The local blackbody weights $a_j(s)$ are calculated by setting the gas temperature, total pressure and species mole fraction to the respective reference values, as below:

$$a_j(s) = F_s\big(\tilde{C}_j, T_b = T_{\text{loc}}, T_g = T_{\text{ref}}, Y_s = Y_{s,\text{ref}}, p_T = p_{T,\text{ref}}\big) - F_s\big(\tilde{C}_{j-1}, T_b = T_{\text{loc}}, T_g = T_{\text{ref}}, Y_s = Y_{s,\text{ref}}, p_T = p_{T,\text{ref}}\big), \quad j = 1,2,\dots,n \quad , \tag{1.33}$$

   where n is the number of gray gases and T_{loc} is the local gas temperature.
3. The local gray-gas absorption coefficients are computed as

$$\kappa_j(s) = N\big(T_{\text{loc}}, p_{T,\text{loc}}, Y_{s,\text{loc}}\big)\, Y_{s,\text{loc}}\, C_{\text{abs},j}\big(T_{\text{loc}}, p_{T,\text{loc}}, Y_{s,\text{loc}}\big) \quad , \tag{1.34}$$

   where $C_{\text{abs},j}\big(T_{\text{loc}}, p_{T,\text{loc}}, Y_{s,\text{loc}}\big)$ is determined from the implicit relation

$$F_s\big(C_{\text{abs},j}, T_b = T_{\text{ref}}, T_g = T_{\text{loc}}, Y_s = Y_{s,\text{loc}}, p_T = p_{T,\text{ref}}\big) = F_s\big(C_{\text{abs},j,\text{ref}}, T_b = T_{\text{ref}}, T_g = T_{\text{ref}}, Y_s = Y_{s,\text{ref}}, p_T = p_{T,\text{ref}}\big) \tag{1.35}$$

$$C_{\text{abs},j,\text{ref}} = \exp\left[\frac{ln(\tilde{C}_j)+ln(\tilde{C}_{j-1})}{2}\right] \quad . \tag{1.36}$$

4. The gray gas RTE is then solved using the parameters determined in the above steps.

1.4.3 Gas Mixtures

For the SLW modeling of a mixture of gases, the direct spectral integration approach of Solovjov and Webb [26] was adopted, originally developed for a mixture of two gases by Denison and Webb [27]. In the direct spectral integration approach, the RTE for the aggregate intensities of a gas mixture of m species is given by

$$\frac{d}{ds} I_{i_1 i_2 \dots i_m}(s) = -\kappa_{i_1 i_2 \dots i_m}(s)\, I_{i_1 i_2 \dots i_m}(s) + a_{i_1 i_2 \dots i_m}(s)\, \kappa_{i_1 i_2 \dots i_m}(s)\, I_b(T)\,, \tag{1.37}$$

where $i_1,\ i_2, \dots\ i_m$ are the gray gas indices of species $1, 2, \dots, m$, respectively. The blackbody weight $a_{i_1 i_2 \dots i_m}$ is defined as the fraction of blackbody energy in the spectrum where the effective absorption cross-sections of species $1, 2, \dots, m$ are C_{abs,i_1}, $C_{\mathrm{abs},i_2}, \dots, C_{\mathrm{abs},i_m}$ respectively.

Based on the approximation that the joint ALBDF of the gas mixture may be expressed as the product of the individual species ALBDF's, it can be shown that the joint weight $a_{i_1 i_2 \dots i_m}$ may be expressed as

$$a_{i_1 i_2 \dots i_m} \approx a_{i_1} a_{i_2} \dots a_{i_m} \tag{1.38}$$

with the normalization condition

$$\sum_{i_1} \sum_{i_2} \dots \sum_{i_m} a_{i_1} a_{i_2} \dots a_{i_m} = 1\ . \tag{1.39}$$

The gray-gas absorption coefficients are written as the molar-density-weighted sum of the species absorption cross-sections [26, 28] as

$$\kappa_{i_1 i_2 \dots i_m} = N_1 C_{i_1} + N_2 C_{i_2} + \dots + N_m C_{i_m}\ , \tag{1.40}$$

where $N_1, N_2, \dots N_m$ are the molar densities of species $1, 2, \dots, m$ respectively.

Using HITEMP 2010, Pearson *et al.* [23, 24] recently derived efficient and accurate functional representations (or correlations) for the ALBDF's of H_2O, CO_2, and CO. Furthermore, Pearson *et al.* [15] tabulated the ALBDF data as a function of variable

temperature, mole fraction, and total pressure for H_2O, CO_2, and CO. These tabulated ALBDF data were utilized for the SLW simulations undertaken in this study.

1.5 RTE Solution Methodologies

Three solution methods for the RTE were considered — the first is an analytical solution for a non-scattering medium and the other two are numerical approaches, namely the Discrete Ordinates Method (DOM) and the Control-Angle Discrete Ordinates Method (CA-DOM). The analytical solution can be evaluated exactly (without numerical quadrature) only for 1-D domains with simplified spatial profiles for the species mole fraction and medium temperature. A brief outline of the three solution methods will now be presented.

1.5.1 Exact Solution of RTE in a 1-D Domain

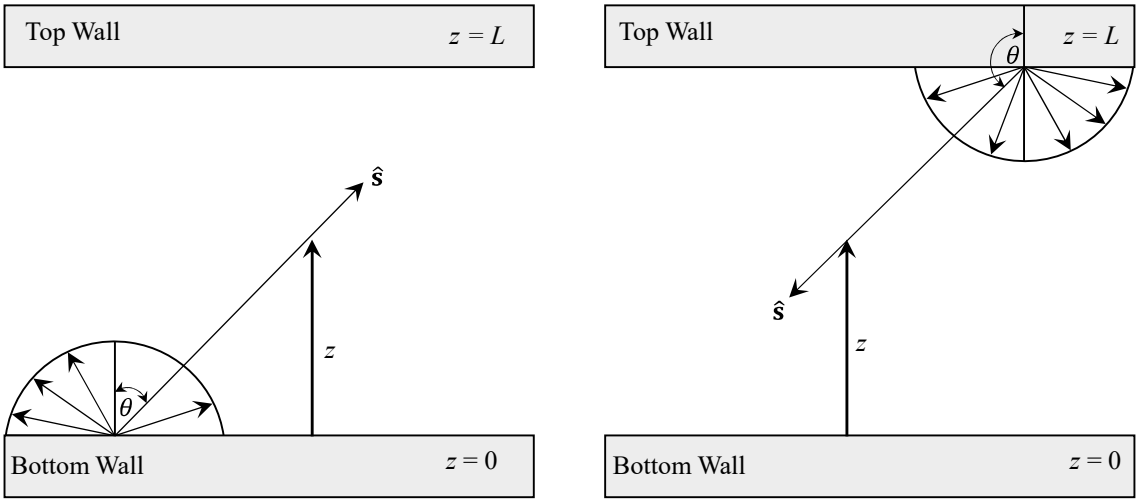

Figure 1.1 Schematic of 1-D plane-parallel medium for the exact solution of RTE [8].

Considering a 1-D plane-parallel medium bounded by two walls, shown in Figure 1.1, the net radiative flux and its divergence at an interior point in the domain contain are determined by the intensities emanating from the bottom and top walls, I_η^+ and I_η^-,

respectively. For an emitting, absorbing and non-scattering medium, the RTE (equation (1.5)) is solved for I_η^+ and I_η^- as functions of the wall-normal coordinate z and polar angle θ, yielding

$$I_\eta^+(z,\theta) = e^{-\frac{1}{cos\theta}\tau_\eta(0\to z)}\, I_\eta^+(0,\theta) + \frac{1}{cos\theta}\int_0^z e^{-\frac{1}{cos\theta}\left[\tau_\eta(0\to z)-\tau_\eta(0\to z')\right]}\,\kappa_\eta(z')\, I_{b\eta}(z')\, dz', \quad \text{for } 0 < \theta < \frac{\pi}{2} \quad , \tag{1.41}$$

where $\tau_\eta(0\to z) = \int_0^z \kappa_\eta(z)\, dz$, and

$$I_\eta^-(z,\theta) = e^{-\frac{1}{cos\theta}\tau_\eta(L\to z)}\, I_\eta^-(0,\theta) + \frac{1}{cos\theta}\int_L^z e^{-\frac{1}{cos\theta}\left[\tau_\eta(L\to z)-\tau_\eta(L\to z')\right]}\,\kappa_\eta(z')\, I_{b\eta}(z')\, dz', \quad \text{for } \frac{\pi}{2} < \theta < \pi \ , \tag{1.42}$$

where $\tau_\eta(L\to z) = \int_L^z \kappa_\eta(z)\, dz$.

1.5.2 DOM in a 1-D Domain

The discrete ordinates method (DOM) is based on discretizing the direction-vector space $\hat{\mathbf{s}}$ into a finite number of direction vectors or ordinates $\hat{\mathbf{s}}_i$, $i = 1, 2, \cdots, N$. Further, DOM entails replacing integrations over solid angle by numerical quadrature, as follows [8]:

$$\int_{4\pi} f(\hat{\mathbf{s}})\, d\Omega = \sum_{i=1}^{n} w_i\ f(\hat{\mathbf{s}}_i) \ , \tag{1.43}$$

where w_i are the quadrature weights associated with the ordinates $\hat{\mathbf{s}}_i$. Expressing $\hat{\mathbf{s}}_i$ in terms of direction cosines, $\hat{\mathbf{s}}_i = \mu_i\, \mathbf{i} + \eta_i\, \mathbf{j} + \xi_i\, \mathbf{k}$, the RTE for each ordinate i can be written as [29]

$$\mu_i \frac{\partial I_{\eta,i}}{\partial x} + \eta_i \frac{\partial I_{\eta,i}}{\partial y} + \xi_i \frac{\partial I_{\eta,i}}{\partial z} = \kappa_\eta I_{b\eta} - \kappa_\eta I_{\eta,i} \ . \tag{1.44}$$

Equation (1.44) can be reduced to 1-D domains by dropping the second and third terms on the left-hand side of the equation. Each of the direction cosines μ_i, η_i, and ξ_i assumes a positive or negative value as the solid angle direction $\hat{\mathbf{s}}_i$ is varied**.**

Analogous to the analytical solution of the RTE in a 1-D plane-parallel medium, the spectral directional intensities in DOM, $I_{\eta,i}$ $(i = 1, 2, \cdots, N)$, can be classified into intensities emanating from each of the two walls bounding the 1-D domain. The intensities $I_{\eta,i}$ $(i = 1, 2, \cdots, N)$ can, therefore, be replaced by $\frac{N}{2}$ intensities $(I^+_{\eta,1}, I^+_{\eta,2}, \cdots, I^+_{\eta,\frac{N}{2}})$ with $\mu_i > 0$, and $\frac{N}{2}$ intensities $(I^-_{\eta,\frac{N}{2}+1}, I^-_{\eta,\frac{N}{2}+2}, \cdots, I^-_{\eta,N})$ with $\mu_i < 0$. The RTE (1.44) is then spatially discretized using finite differencing to yield the cell-center intensities [29],

$$I^p_{\eta,i} = \frac{(\mu_i / \gamma)\, I^w_{\eta,i} + \kappa_\eta\, I_{b\eta,i}\, \Delta x}{(\mu_i / \gamma) + \kappa_\eta\, \Delta x} \qquad \mu_i > 0 \tag{1.45}$$

$$I^p_{\eta,i} = \frac{(|\mu_i| / \gamma)\, I^e_{\eta,i} + \kappa_\eta\, I_{b\eta,i}\, \Delta x}{(|\mu_i| / \gamma) + \kappa_\eta\, \Delta x} \qquad \mu_i < 0 \quad , \tag{1.46}$$

where γ is a weighting factor that relates the cell-center intensity $I^p_{\eta,i}$ to the intensities at the west and east faces of the cell, $I^w_{\eta,i}$ and $I^e_{\eta,i}$, respectively, as follows:

$$I^i_{p,\eta} = \gamma\, I^i_{e,\eta} + (1 - \gamma)\, I^i_{w,\eta} \quad . \tag{1.47}$$

In this study, $\gamma = 0.5$ was considered.

1.5.3 CA-DOM in 1-D Domains

The control-angle discrete ordinates method (CA-DOM) is also based on the discretization of directional or solid-angle space. However, there are important differences between DOM and CA-DOM. In DOM, the direction space is discretized into a finite number of direction vectors or ordinates $\hat{\mathbf{s}}_i$, whereas CA-DOM draws its

inspiration from the finite volume method (FVM). In FVM, the spatial domain is discretized into control volumes known as finite volumes, followed by the integration of the governing equation over a control volume. Analogously, in CA-DOM, the 4π solid angle space is divided into control angles $\Delta\Omega^i$, with each control angle $\Delta\Omega^i$ enveloping or surrounding the corresponding direction vector $\hat{\mathbf{s}}$. Secondly, in DOM, finite differencing is employed for spatial discretization, whereas in CA-DOM, the standard finite volume method is utilized. Thus, in CA-DOM, the RTE is integrated over the spatial control volume, as well as the control angle $\Delta\Omega^i$, where as no such integration is warranted in DOM.

For 1-D domains, the CA-DOM form of the spatio-directional intensity in a control volume p and control angle i is given by [30]

$$I_{\eta,i}^{p} = \frac{D_{x,i}^{-}\, I_{\eta,i}^{w} + \kappa_\eta\ \Delta x\ \Delta\Omega^i I_{b\eta,i}}{D_{x,i}^{+}\ + \kappa_\eta\, \Delta x\ \Delta\Omega^i} \quad , \tag{1.48}$$

where $\Delta\Omega^i$ is the control angle (or, the solid angle), $I_{\eta,i}^{w}$ is the intensity in the control volume that lies on the upstream side (west in 1-D) of the current control volume p. The factors $D_{x,i}^{+}$ and $D_{x,i}^{-}$ are given by [30]

$$D_{x,i}^{+} = \int_{\Delta\Omega^i} \mathbf{s}^i \bullet \mathbf{n}^j\, d\Omega, \qquad \mathbf{s}^i \bullet \mathbf{n}^j > 0 \tag{1.49}$$

$$D_{x,i}^{-} = \int_{\Delta\Omega^i} |\mathbf{s}^i \bullet \mathbf{n}^j|\, d\Omega, \qquad \mathbf{s}^i \bullet \mathbf{n}^j < 0 \ , \tag{1.50}$$

where $\mathbf{n}^j$ is the outward unit normal vector to the jth face of the control volume. In equation (1.48), the factor $\Delta\Omega^i$ arises from the integration of the RTE over the ith control angle.

1.6 Results

Table 1.1 lists the 1-D enclosure cases considered in this study. For each case, five spectral approaches were considered: (1) NBM with EM2C data, (2) NBM with spectral averaging, (3) LBL absorption coefficient spectra calculated from HITEMP 2010, (4) SLW method, and (5) wavenumber-selective LBL (WS-LBL) calculations. The LBL calculations serve as the benchmark, while the WS-LBL calculations help infer the effects of the approximation $\overline{\kappa_\eta I_\eta} \approx \bar{\kappa}_\eta \bar{I}_\eta$ on NBM predictions. Both DOM and CA-DOM methods for solving the RTE are considered for all cases in Table 1.1. The exact analytical solution to the RTE is also considered for Cases 1a, 1b, 1c, 2 and 3. The 1-D enclosure is divided into 200 spatial control volumes or grid cells. When solving the RTE using DOM, 36 quadrature points were used, while for the CA-DOM method, the polar angle space $\theta \in [0, \pi]$ was divided into 36 control angles. For the SLW simulations, 20 gray gases were used.

The cases in Table 1.1 were chosen to exercise the NBM over a broad parametric space consisting of various domain sizes (or optical thicknesses), isothermal or non-isothermal media, homogeneous or inhomogeneous species mole fractions, and single participating species (H_2O or CO_2) or a mixture of H_2O and CO_2. Consideration of enclosures with H_2O or CO_2 is also equivalent to varying the optical thickness of the medium, as it is known that CO_2 is optically thicker than H_2O. The temperature profile in Case 4 is illustrated in Figure 1.2, while the temperature and mole fraction profiles for Cases 5 and 6 are shown in Figure 1.3. Two quantitative measures of radiative transfer for the cases are presented and listed in Table 1.1, namely the radiative heat flux along x-direction, $q_x = \mathbf{q} \bullet \hat{\mathbf{e}}_x$ ($\mathbf{q}$ is the heat flux vector and $\hat{\mathbf{e}}_x$ is the unit vector

along x), and the radiative source term in the energy equation or the negative of flux divergence, $-\nabla \cdot \mathbf{q} = -\frac{dq_x}{dx}$ in 1-D.

Table 1.1 List of 1-D enclosure cases considered. Cases 1a, 1b, 2, 4 and 5 were all adopted from Chu *et al.* [3]. In Case 3, L is the domain length.

Case	Medium	Domain Length	Domain Temperature	Wall Temperature (K)	Pressure (atm)	Wall Emissivity	H_2O Mole Fraction	CO_2 Mole Fraction
1a	H_2O	0.1	1000	300, 300	1.0	1.0, 1.0	1.0	--
1b	H_2O	1.0	1000	300, 300	1.0	1.0, 1.0	1.0	--
1c	H_2O	0.1	3000	300, 300	1.0	1.0, 1.0	1.0	--
2	CO_2	0.1	2000	300, 300	1.0	1.0, 1.0	--	0.5
3	CO_2	1.0	1000	300, 300	1.0	1.0, 1.0	--	$4(1-x/L)x$
4	H_2O	0.2	variable	1500, 300	1.0	1.0, 1.0	1.0	--
5	$H_2O + CO_2$	0.5	variable	300, 300	1.0	1.0, 1.0	variable	variable

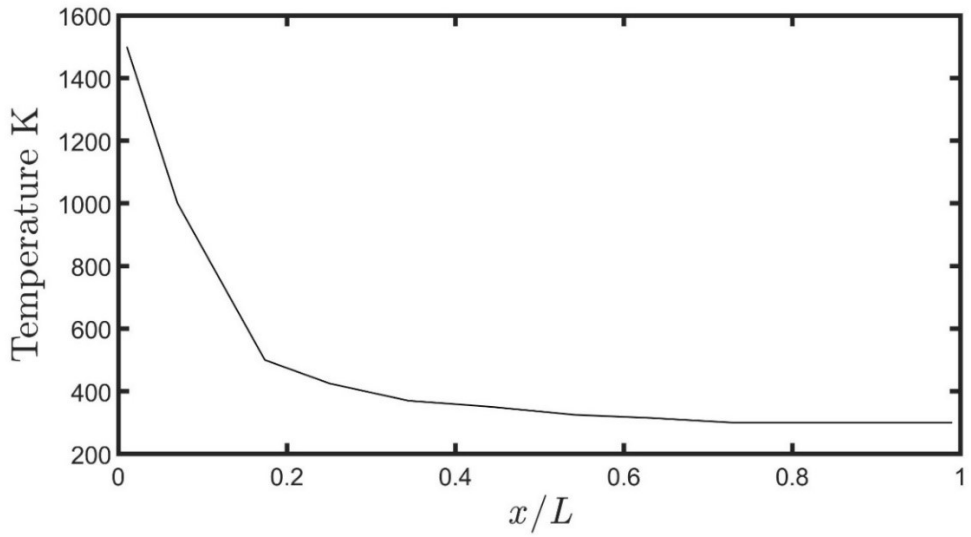

Figure 1.2 Non-isothermal temperature profile in Case 4 [31].

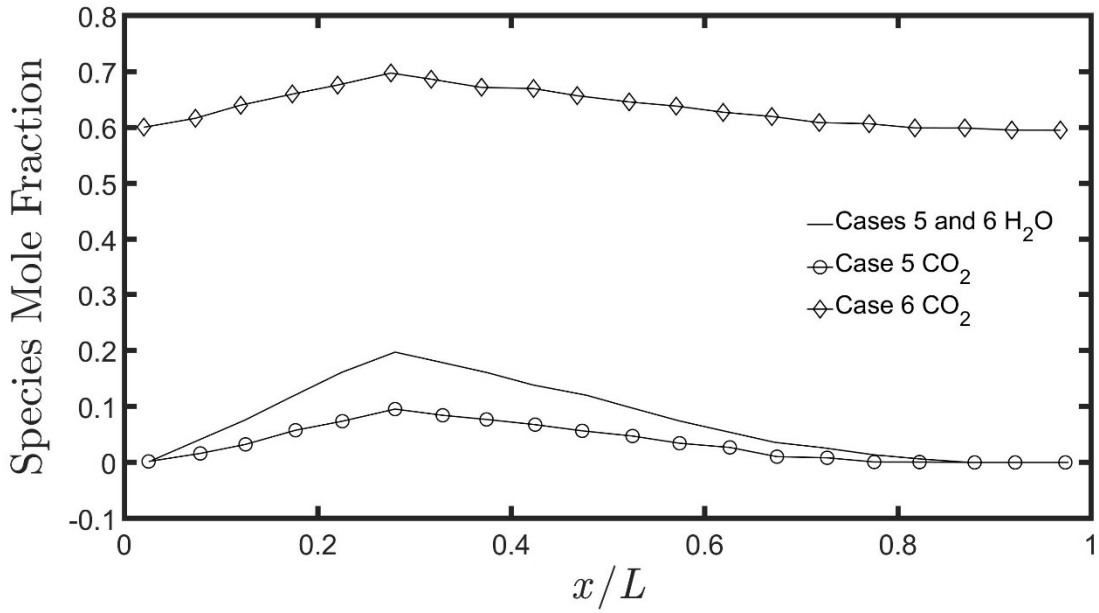

(a)

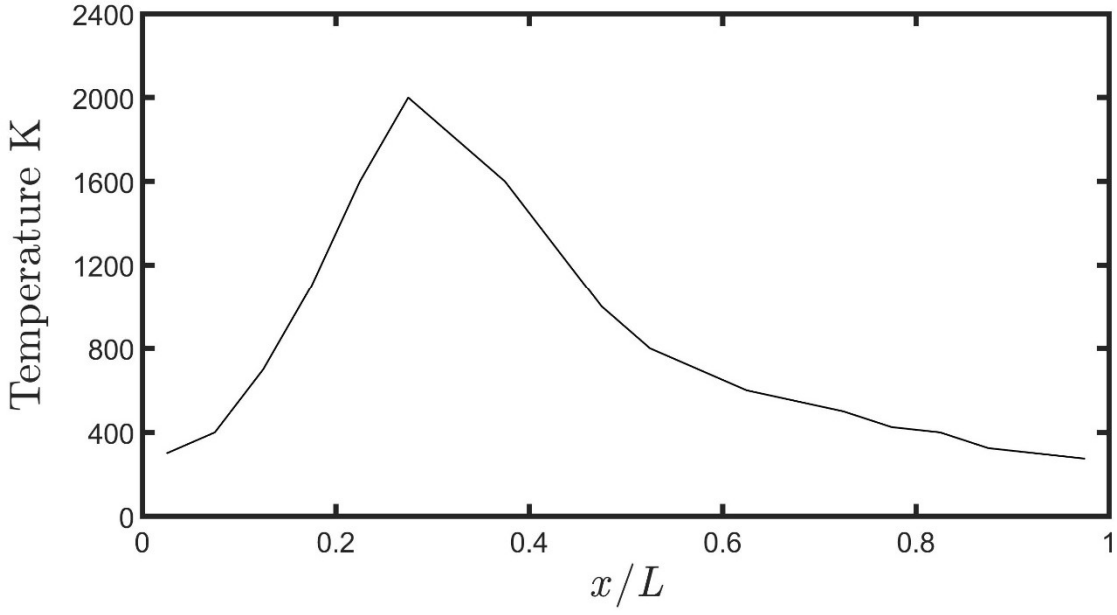

(b)

Figure 1.3 For Case 5: (a) inhomogeneous mole fraction profile and (b) non-isothermal temperature profile [3, 31].

1.6.1 Cases 1a and 1b

The enclosures in Cases 1a and 1b are isothermal and homogeneous with lengths $L = 0.1$ m and 1 m, respectively. In both cases, the participating species is H_2O with mole fraction unity and temperature 1000 K. The domain is bounded to the left and right by black walls at 300 K. The objective in varying the domain length from Case 1a to Case 1b is to study the effects of medium optical depth on the performance of the NBM.

For Case 1a, in Figures 1.4 (a) and (b) the radiative flux and the radiative source are compared, respectively, obtained using the three solution methods — DOM, CA-DOM and the exact solution of the RTE — in combination with the LBL absorption coefficients. The DOM and CA-DOM results for the flux and source term are observed to be in excellent agreement with those calculated using the exact solution. In Figure 1.4 (a), the negative flux at $x = 0$ and the positive flux at $x = L$ are indicative of radiative transport from the hotter medium at 1000 K to the cooler boundaries at 300 K. The flux magnitude decreases as it moves away from the boundaries, with the flux direction reversing as it crosses the center of the enclosure. The reversal of flux direction indicates that the radiative flux q_x from the gas situated on the left/right of the domain center is directed toward the left/right wall. The direction and magnitude of the fluxes are also supported by the trends in the radiative source term, $\left(-\frac{dq_x}{dx}\right)$, in Figure 1.4 (b). A negative value of $\left(-\frac{dq_x}{dx}\right)$ is indicative of net radiative flux leaving a location or control volume, *i.e.*, the gas in the control volume is a net emitter of radiative energy. As the walls are significantly cooler than the medium, Figure 1.4 (b) shows that the gas is a net emitter of radiative energy throughout the domain. Analogous to the radiative fluxes, the magnitude of the source term is the highest at the walls and decreases as it moves inward

into the medium (*i.e.*, away from the two boundaries). Since the profile of the flux q_x becomes steeper as it approaches the wall, the magnitude of the gradient $\frac{dq_x}{dx}$ also increases correspondingly.

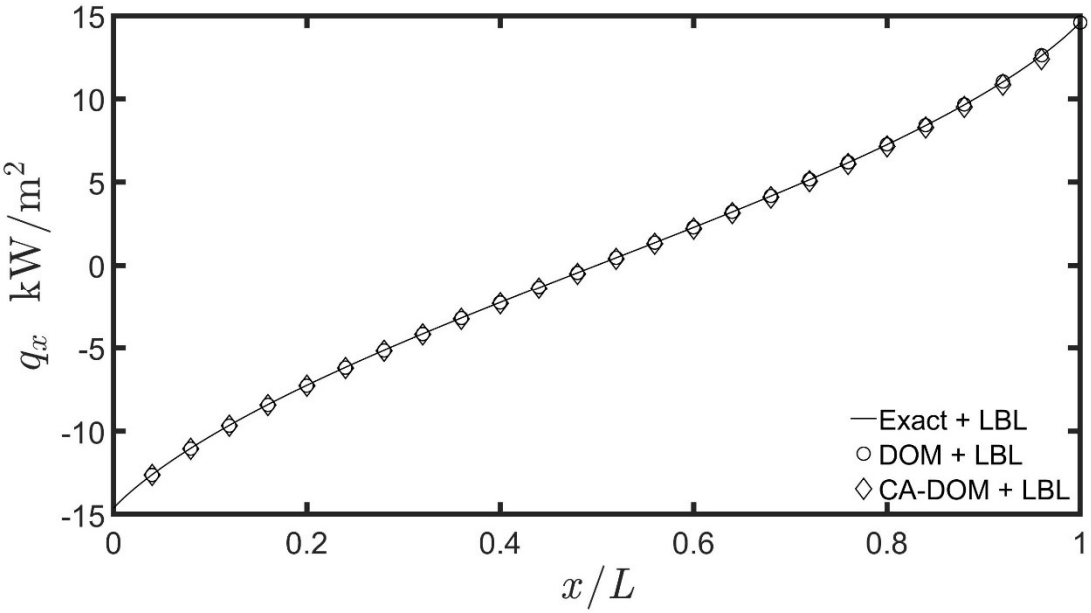

(a)

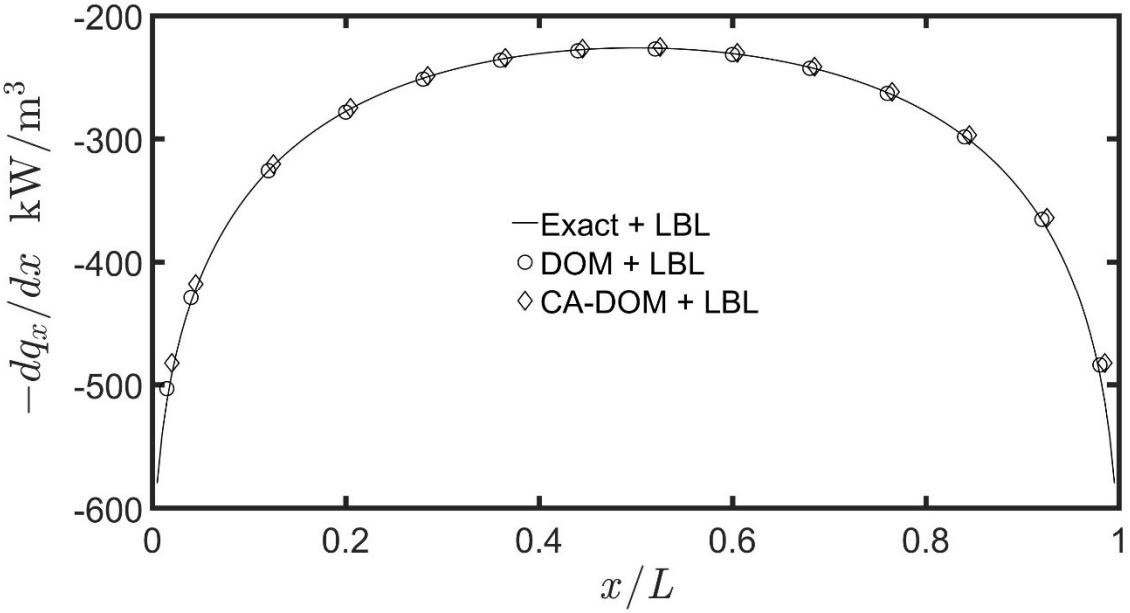

(b)

Figure 1.4 Comparison of 1-D exact analytical, DOM and CA-DOM solution methods for Case 1a. (a) radiative fluxes q_x, and (b) radiative source terms $(-dq_x/dx)$.

Having assessed the three solution methods for Case 1a, the fluxes and source terms computed using the five spectral approaches are compared. In Figures 1.5 (a) and 1.5 (b), the exact solution to the RTE is considered for all spectral approaches except SLW that uses DOM. It can be seen in Figure 1.5 that the SLW and WS-LBL predictions are in excellent agreement with the LBL results. The two NBM forms, NBM with EM2C and NBM with spectral averaging, are in good agreement with each other, but differ noticeably from LBL. Using the exact solution with the LBL absorption coefficients as the benchmark, the errors in SLW, WS-LBL and the two NBM predictions are shown in Figure 1.6. Specifically, errors in q_x and $\left(-\frac{dq_x}{dx}\right)$ as a function of x are shown in Figures 1.6 (a) and 1.6 (b), respectively. Evidently, the errors are the highest for the two NBM forms. The WS-LBL method, however, performs significantly better than both NBM forms, suggesting that the errors in NBM due to the approximation $\overline{\kappa_\eta I_\eta} \approx \bar{\kappa}_\eta \bar{I}_\eta$ are higher in a smaller domain with a correspondingly lower optical depth. It is anticipated that the higher optical depth of a longer domain would mitigate the errors arising from this approximation. It can also be seen that the errors in SLW model predictions are close to zero.

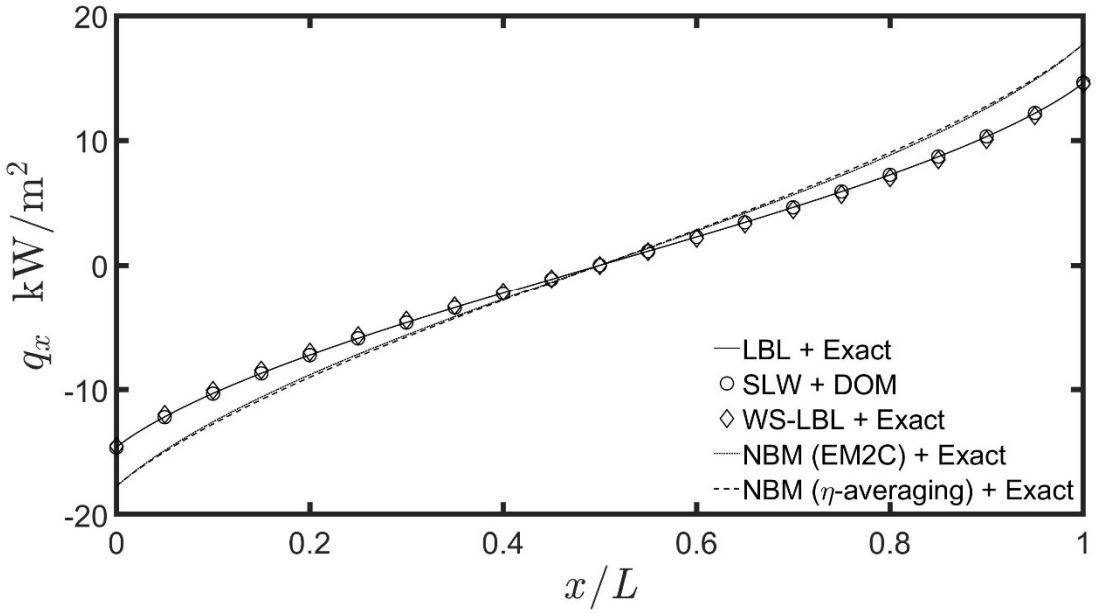

(a)

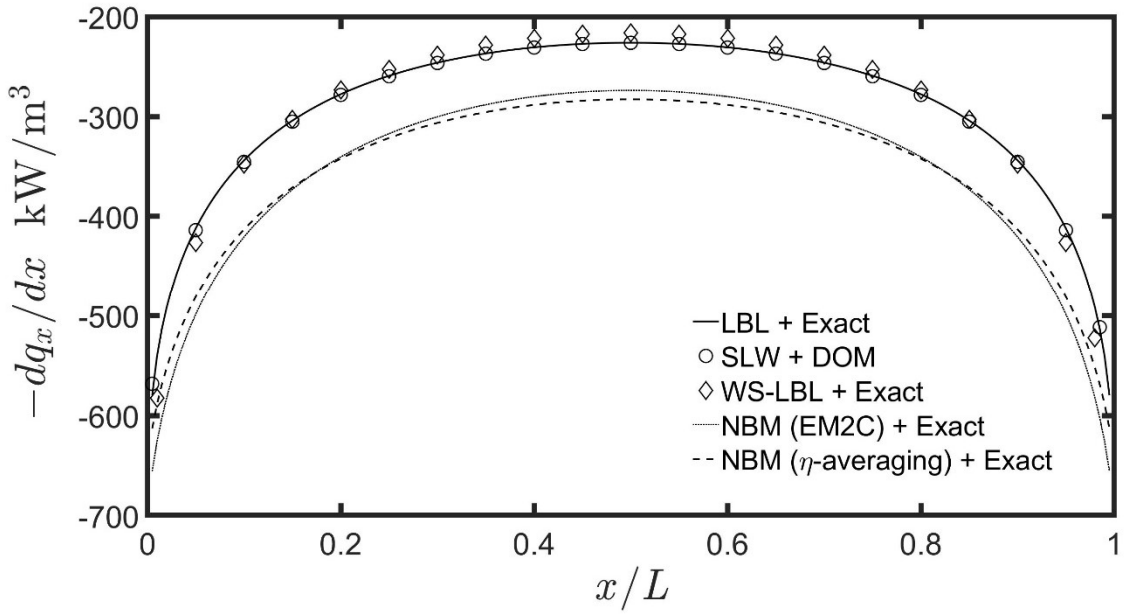

(b)

Figure 1.5 Comparison of 1-D LBL, SLW, WS-LBL and two NBM forms in combination with the exact solution for Case 1a. (a) radiative fluxes q_x, and (b) radiative source terms $(-dq_x/dx)$.

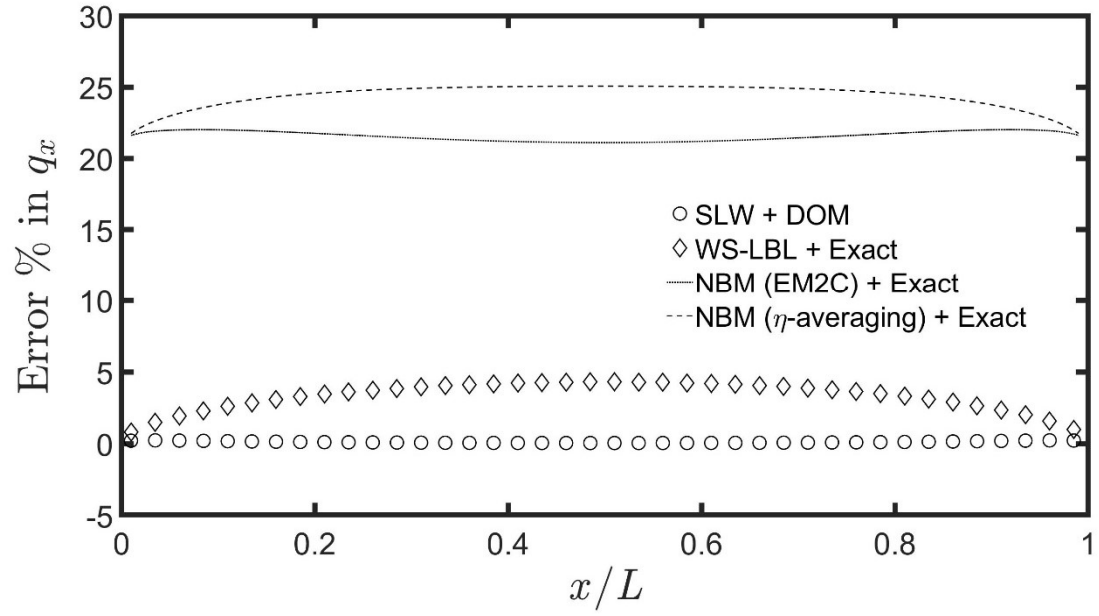

(a)

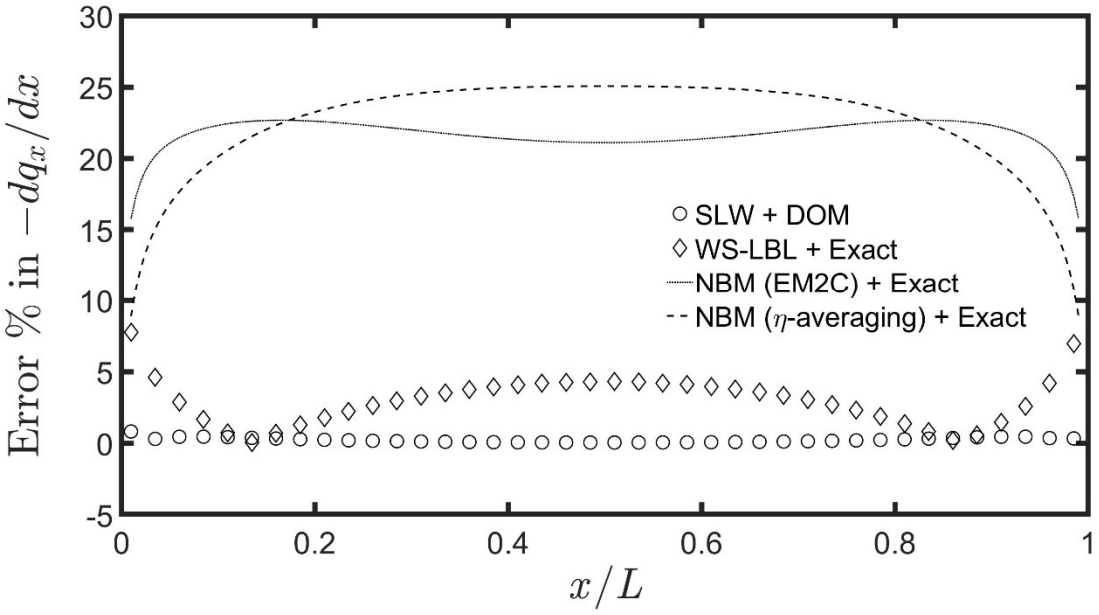

(b)

Figure 1.6 Errors in SLW, WS-LBL and the two NBM forms relative to the Exact-LBL solution for Case 1a. (a) radiative fluxes q_x, and (b) radiative source terms $(-dq_x/dx)$.

To investigate the effects of optical depth, Case 1b with the same species properties as Case 1a is considered, but with a longer domain length $L = 1$ m. For this case, Figures 1.7 (a) and 1.7 (b) present the radiative fluxes and source terms, respectively. In these figures, DOM, CA-DOM and the exact solution are compared when coupled with LBL absorption coefficients. It can be seen that the predictions of DOM and CA-DOM are in excellent agreement with those of the exact solution. Figure 1.4 and 1.7 illustrate the qualitative similarities in the flux and source term profiles for Cases 1a and 1b. However, there are important quantitative differences between the two cases. The magnitudes of radiative fluxes for Case 1b are higher than those in Case 1a, particularly in regions close to the two boundaries. Due to the longer domain, the boundaries in Case 1b receive higher radiative energy from the medium, as there is lot more gas that acts as an emitter to the walls. Interestingly, the source term in Case 1b, shown in Figure 1.7 (b), is approaching zero near the center of the domain. This is to be expected because the gas in the center of the domain is neither a net emitter nor a net absorber. In order for this behavior to be apparent, a longer domain is needed as in Case 1b.

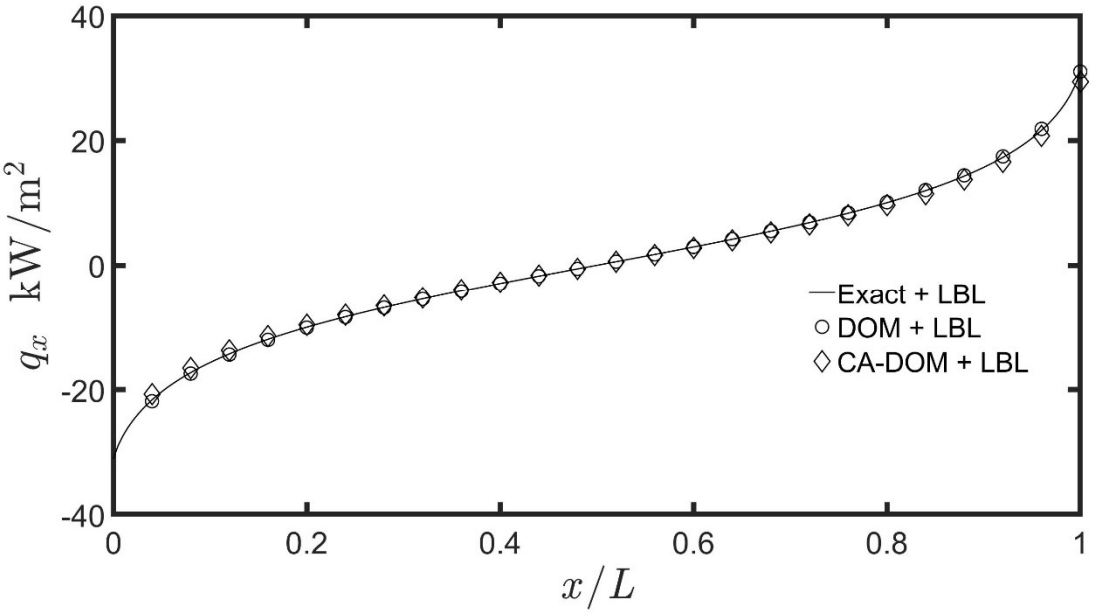

(a)

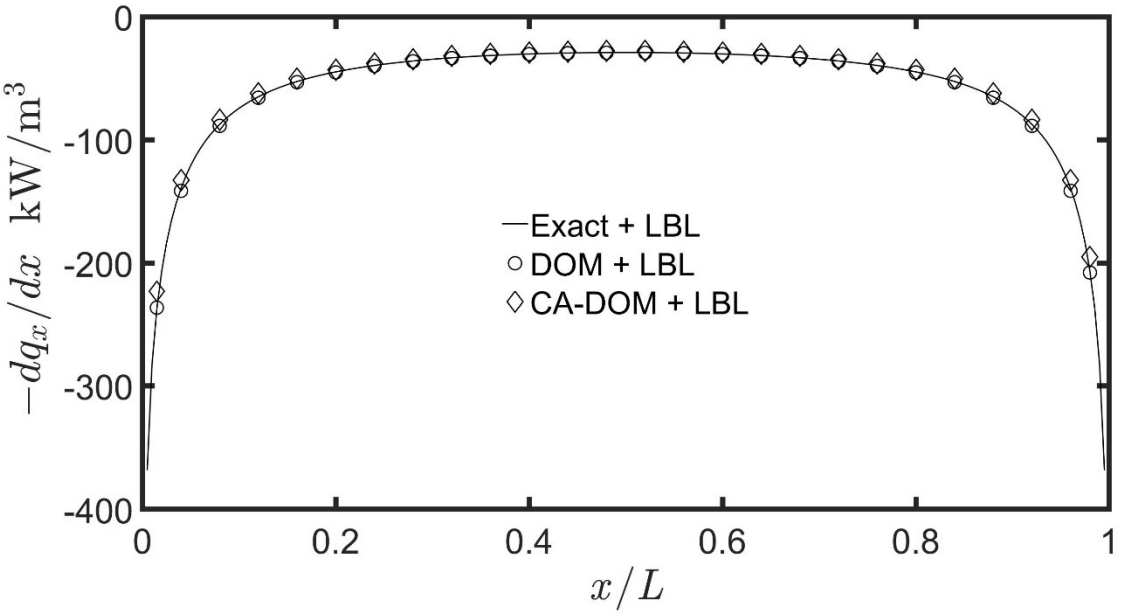

(b)

Figure 1.7 Comparison of 1-D exact analytical, DOM and CA-DOM solution methods for Case 1b. (a) radiative fluxes q_x, and (b) radiative source terms $(-dq_x/dx)$.

Figures 1.8 (a) and 1.8 (b) show a comparison of fluxes and source terms obtained using the various spectral approaches coupled with the exact solution of the RTE, except for SLW, which is based on DOM. As in Case 1a, both the SLW and WS-LBL predictions are observed to be in excellent agreement with the LBL data. However, in contrast to Case 1a, the performance of the two NBM forms is significantly improved for Case 1b. The improved accuracy of the two NBM forms can be seen in Figures 1.9 (a) and 1.9 (b) that show the errors in q_x and $\left(-\frac{dq_x}{dx}\right)$, respectively, as a function of x. In Case 1a, the errors in the NBM predictions were in the 20-25% range, whereas in Case 1b, they are reduced to ~10% (away from the boundaries). Since the domain length is the only parameter varied from Case 1a to 1b, the improvement in NBM results may be attributed to the increased optical thickness arising from the higher domain length. As in Case 1a, the WS-LBL performs well here too and the SLW method predictions are essentially identical to those of LBL (as seen from the errors in SLW being nearly zero).

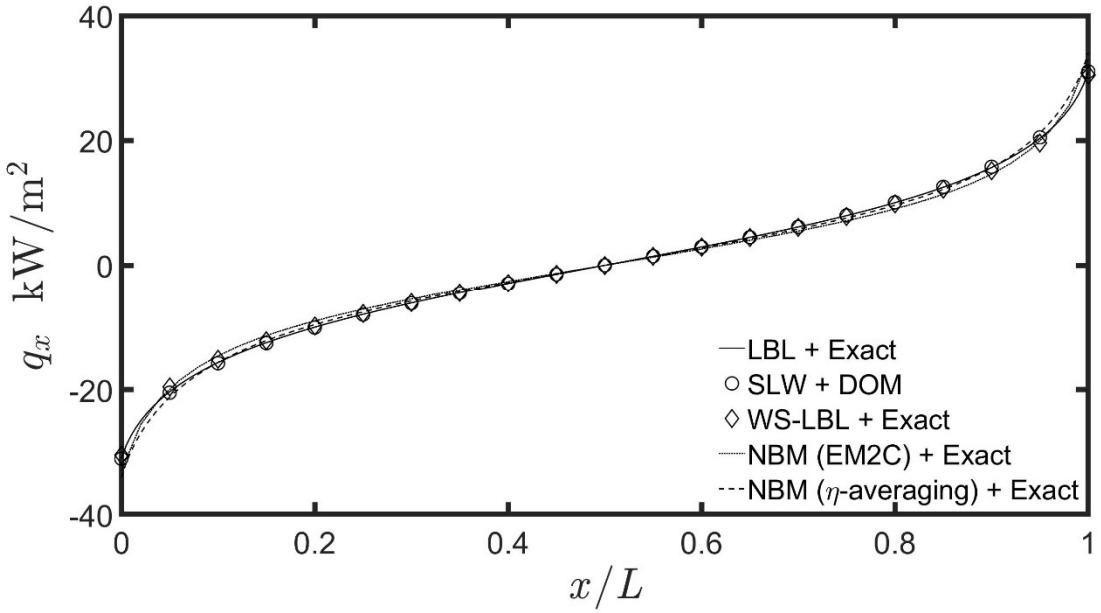

(a)

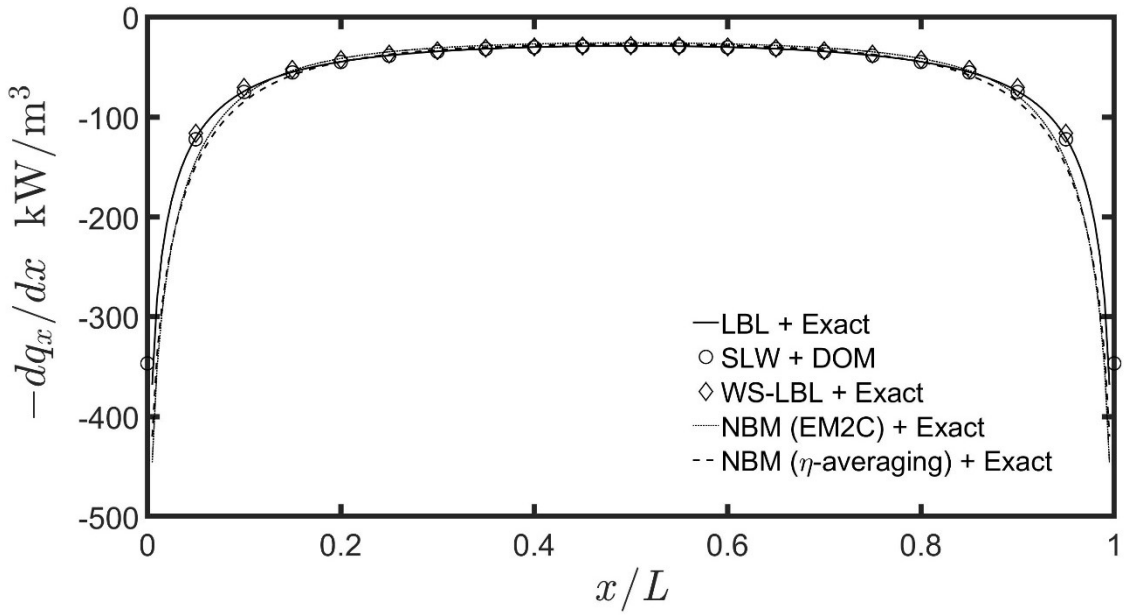

(b)

Figure 1.8 Comparison of 1-D LBL, SLW, WS-LBL and two NBM forms in combination with the exact solution for Case 1b. (a) radiative fluxes q_x, and (b) radiative source terms $(-dq_x/dx)$.

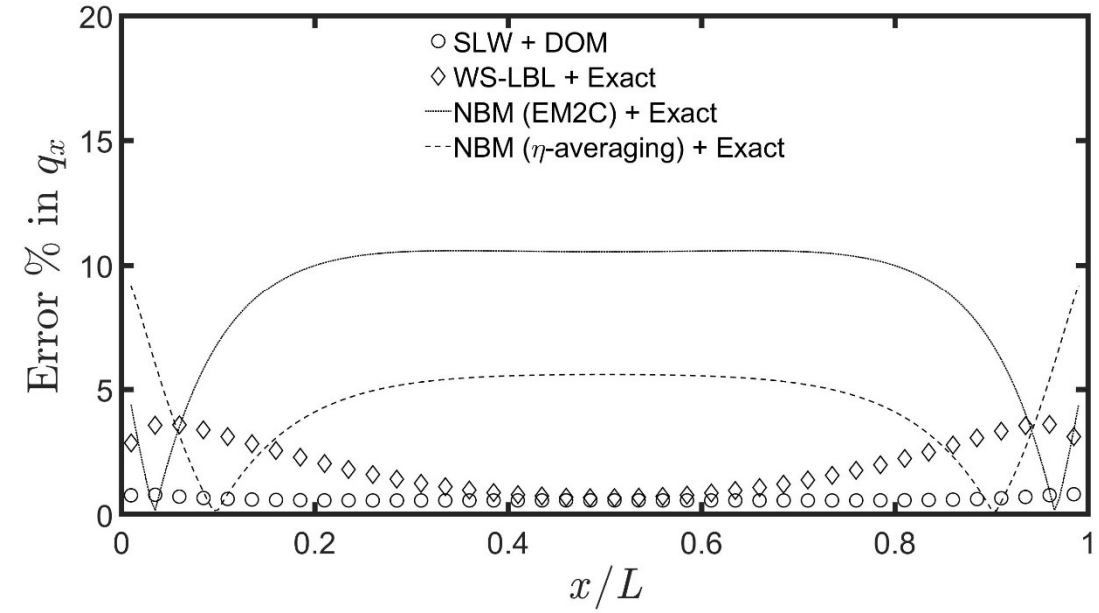

(a)

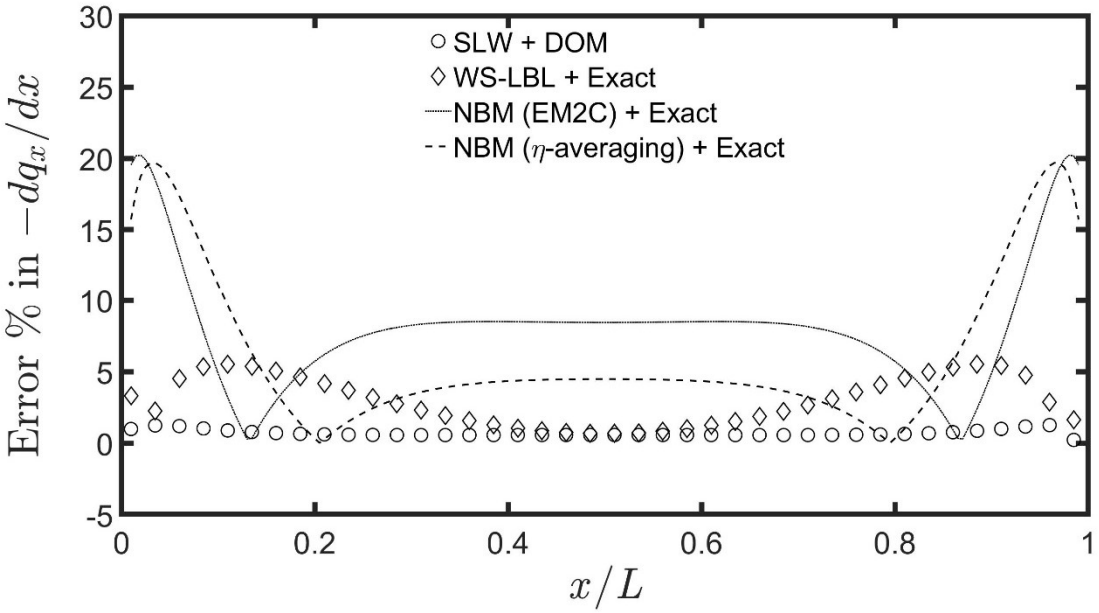

(b)

Figure 1.9 Errors in SLW, WS-LBL and the two NBM forms relative to the Exact-LBL solution for Case 1b. (a) radiative fluxes q_x, and (b) radiative source terms $(-dq_x/dx)$.

1.6.2 Case 1c

Case 1c consists of an isothermal and homogeneous 1-D enclosure with length $L = 0.1$ m. The participating species is H_2O with a mole fraction of unity and a temperature of 3000 K. The domain is bounded to the left and right by black walls at 300 K. The only difference between Case 1a and Case 1c is that their domain temperatures are 1000 K and 3000K, respectively. Through Case 1c, it will be demonstrated that in a domain with lower optical thickness (*i.e.*, smaller domain size compared to Case 1b), the consideration of higher medium temperatures will mitigate the errors arising from the approximation $\overline{\kappa_\eta I_\eta} \approx \bar{\kappa}_\eta \bar{I}_\eta$. The fluxes and source terms in Figures 1.10 (a) and 1.10 (b) are compared, respectively. The corresponding errors in the predictions of the four spectral models relative to LBL calculations are shown in Figures 1.11 (a) and 1.11 (b), respectively. The errors in fluxes and source terms for NBM with spectral averaging are in the 3 to 4 % range, while those for NBM with EM2C data are in the 4 to 5% range. In Case 1a, these errors were in the 20 to 25 % range. Thus, a significant decrease in errors is realized when applying the NBM at higher temperatures in domains with smaller size.

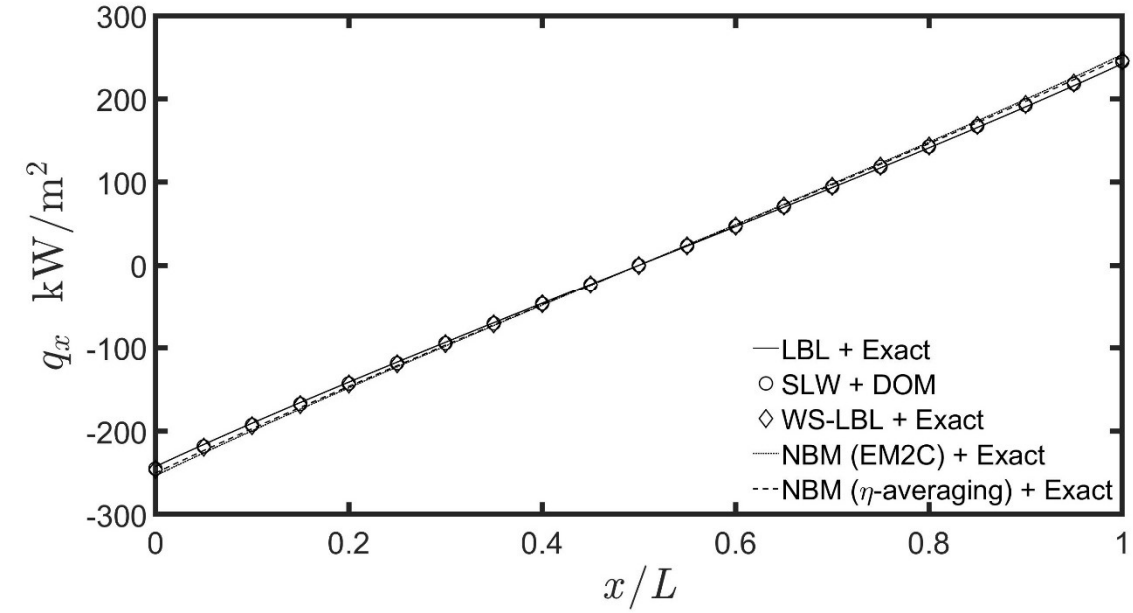

(a)

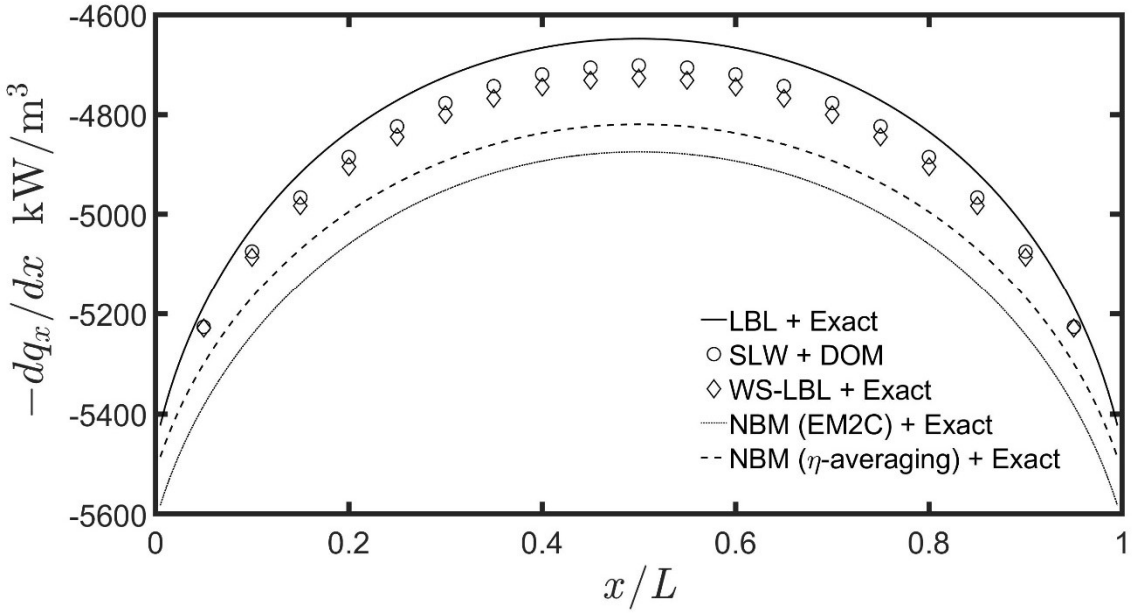

(b)

Figure 1.10 Comparison of 1-D LBL, SLW, WS-LBL and two NBM forms in combination with the exact solution for Case 1c. (a) radiative fluxes q_x, and (b) radiative source terms $(-dq_x/dx)$.

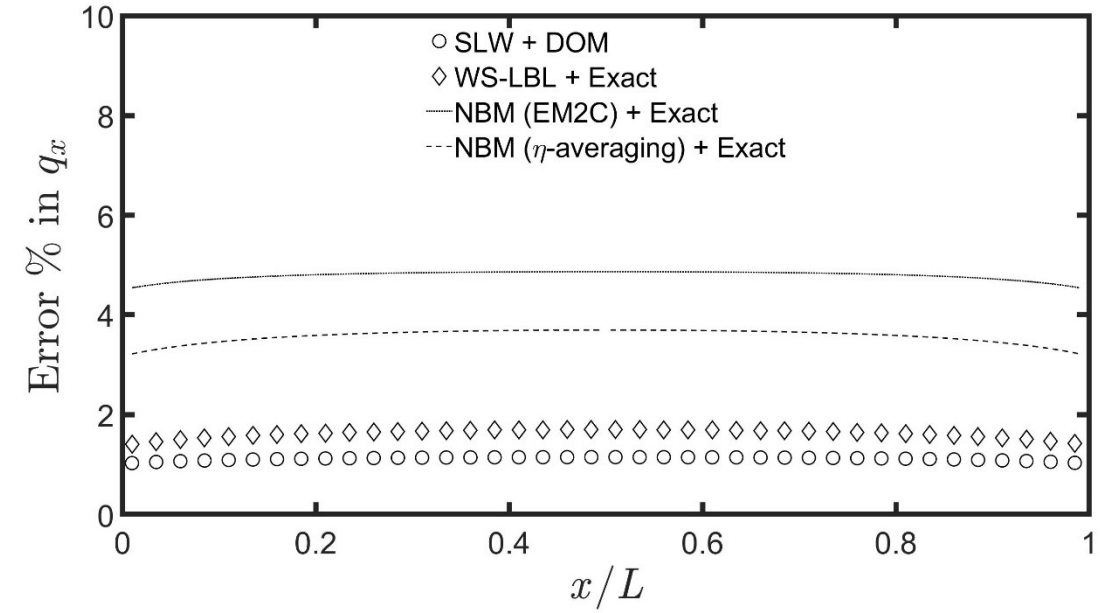

(a)

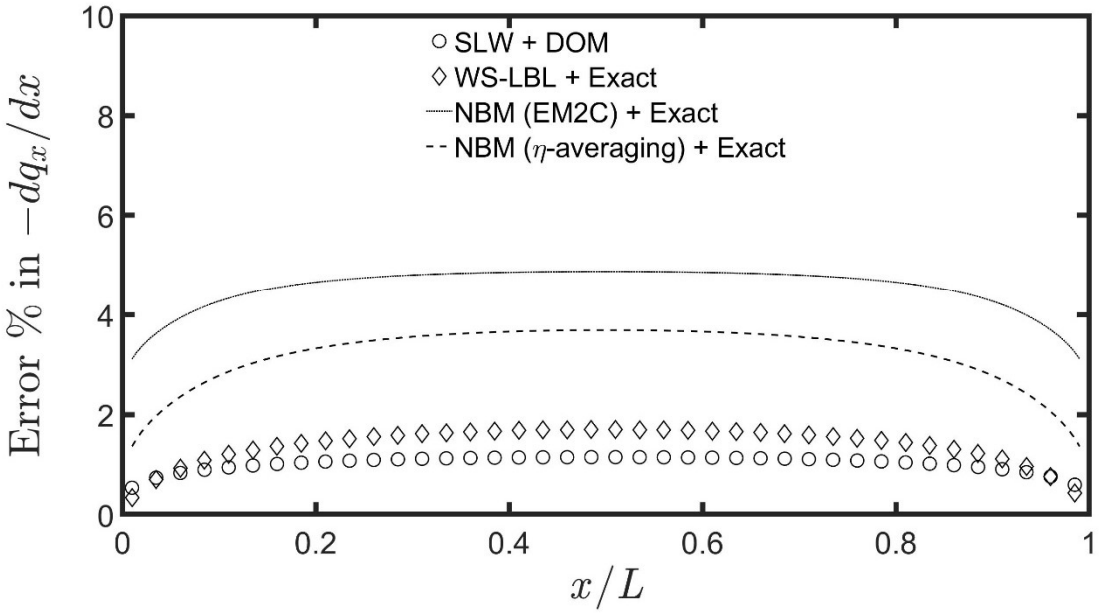

(b)

Figure 1.11 Errors in SLW, WS-LBL and the two NBM forms relative to the Exact-LBL solution for Case 1c. (a) radiative fluxes q_x, and (b) radiative source terms $(-dq_x/dx)$.

1.6.3 Case 2

The enclosure in Case 2 is isothermal and homogeneous as in Cases 1a and 1b, but with CO_2 as the participating species. The domain length $L = 0.1$ m, medium temperature is 2000 K, walls are black at temperature 300 K, and CO_2 mole fraction is 0.5. Figures 1.12 (a) and 1.12 (b) compare the fluxes and source terms computed using the spectral approaches coupled with the exact solution, except for SLW, which uses DOM. The negative flux at $x = 0$ and the positive flux at $x = L$ are due to radiative transfer from the hotter medium at 2000 K to the cooler walls at 300 K. The negative values of $\left(-\frac{dq_x}{dx}\right)$ for all x suggest that the gas is a net emitter of radiative energy throughout the domain. The magnitude of the source term is the highest at the walls but decreases as it moves away from the walls toward the center of the domain. Adjacent to the walls, the gas receives the least amount of radiative energy so that the net of the gas-emitted and gas-received radiative energies is maximum at the walls. It can be seen in Figures 1.12 (a) and 1.12 (b) that the SLW and WS-LBL predictions are in excellent agreement with the LBL results. The two NBM forms also show good agreement with LBL, which can be attributed to the inherently high optical thickness of CO_2. Thus, although Case 2 has the same domain length as Case 1a, the NBM model performs significantly better in Case 2, as CO_2 is optically thicker compared to H_2O.

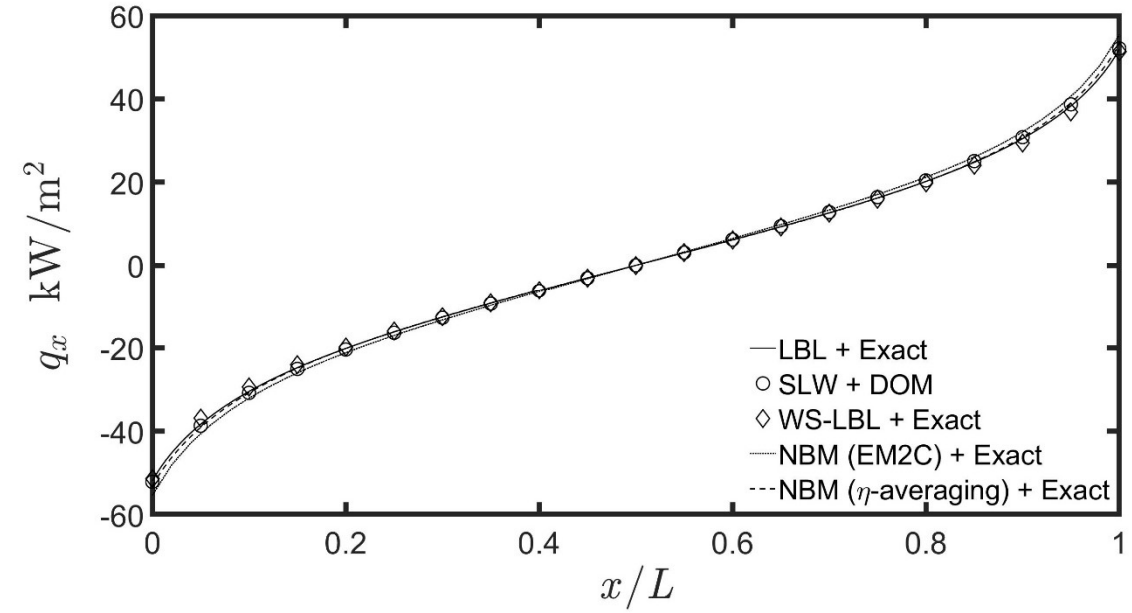

(a)

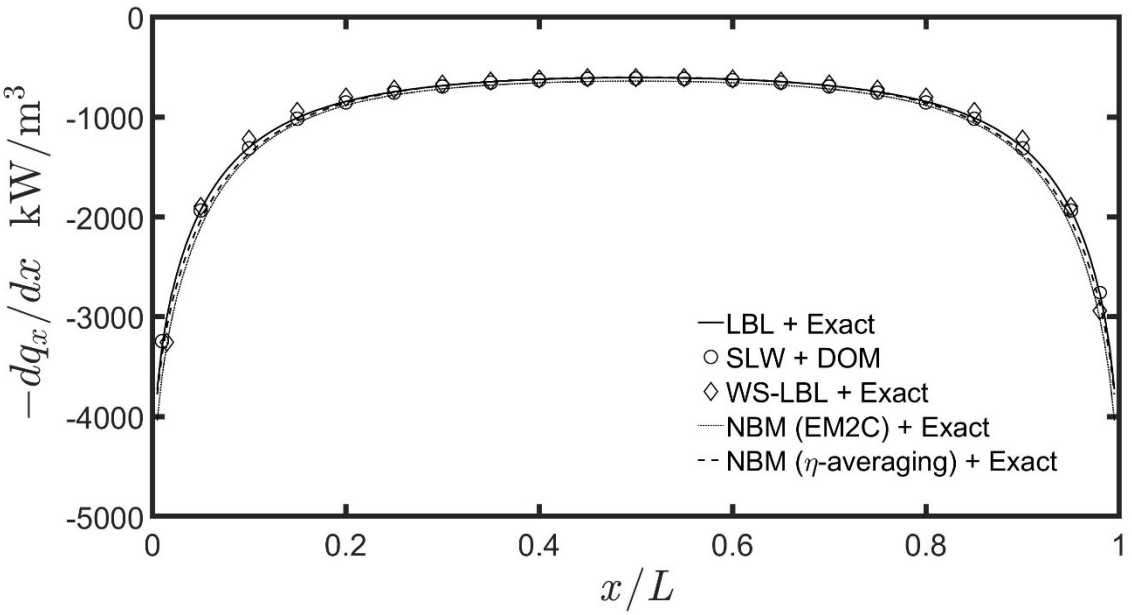

(b)

Figure 1.12 Comparison of 1-D LBL, SLW, WS-LBL and two NBM forms in combination with the exact solution for Case 2a. (a) radiative fluxes q_x, and (b) radiative source terms $(-dq_x/dx)$.

1.6.4 Case 3

This is a case with uniform medium temperature, but inhomogeneous species mole fractions. The participating species is CO_2 with a parabolic mole-fraction profile indicated in Table 1.1. The domain length and temperature are 1 m and 1000 K, respectively, and the two boundary walls are black at a temperature of 300 K. This case is significant for multiple reasons. Firstly, in spite of the inhomogeneous mole fraction profile, Case 3 allows the exact analytical solution to be obtained for the RTE. This is because for CO_2, the absorption cross-sections are weakly dependent on mole fraction, so that the mole-fraction dependence for CO_2 is manifested only as a multiplicative factor in the absorption coefficient (*i.e.*, only in equation (1.29)). Therefore, this case serves as a valuable test case for evaluating the performance of the DOM and CA-DOM numerical solutions. The exact RTE solution in combination with the LBL absorption coefficients is also an ideal benchmark for evaluating approximate spectral models. Secondly, the parabolic profile of CO_2 mole fraction is such that the mole fraction is maximum at the center of the domain and approaches zero at the two walls. As will be seen in the discussion that follows, this mole fraction profile leads to a rather interesting spatial profile of the radiative source term.

In Figures 1.13 (a) and 1.13 (b), the radiative fluxes and source terms computed using the three solution methods in conjunction with the LBL absorption coefficients are compared. Generally, both DOM and CA-DOM are in good agreement with the exact solution, although DOM shows slightly better agreement than CA-DOM. The radiative source terms shown in Figure 1.13 (b) are of greater interest in this case. It is seen that the profile of $\left(-\frac{dq_x}{dx}\right)$ has a "w" shape, which arises because $\left(-\frac{dq_x}{dx}\right)$ gradually

approaches zero, both at the walls and in the center of the enclosure. At the walls, the source term approaches zero due to the CO_2 mole fraction going to zero. The zero source is not able to be captured as this requires a much higher spatial resolution at the walls. At the domain center, the source term tends to zero because at this location the medium is neither an emitter nor an absorber, which again can be captured with a finer spatial resolution (and/or longer domain length). In Figure 1.13 (b), it can be seen that both DOM and CA-DOM are able to capture the "w" shape of $\left(-\frac{dq_x}{dx}\right)$ profile. When compared to CA-DOM, the DOM results are in slightly closer agreement with the LBL source terms.

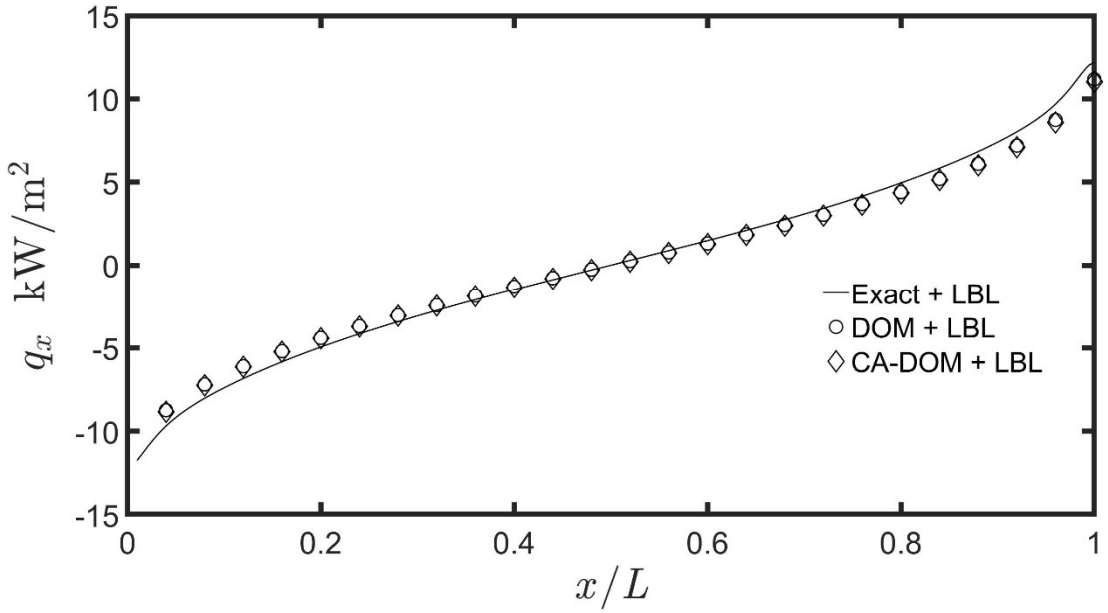

(a)

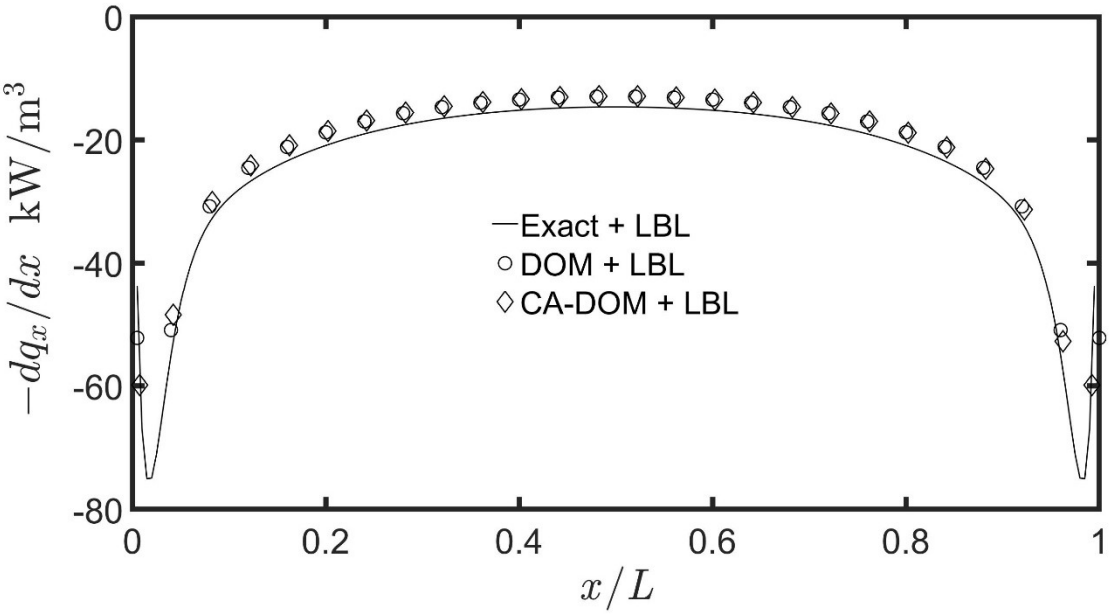

(b)

Figure 1.13 Comparison of 1-D exact analytical, DOM and CA-DOM solution methods for Case 3. (a) radiative fluxes q_x, and (b) radiative source terms $(-dq_x/dx)$.

Figures 1.14 (a) and 1.14 (b) show a comparison of the fluxes and source terms obtained using the spectral approaches coupled with the exact solution (again, except for SLW which is coupled with DOM). Figure 1.14 (a) shows that all four spectral models show good agreement with the LBL data for fluxes. In Figure 1.14 (b), it can be seen that the predictions of $\left(-\frac{dq_x}{dx}\right)$ by the two NBM forms are in reasonable agreement with the LBL data, with the comparison improving away from the walls. It should be noted that the derivative in the flux accentuates the differences between LBL and the other spectral models. With the exact-LBL solution as the benchmark, the errors in q_x and $\left(-\frac{dq_x}{dx}\right)$ as a function of x for the SLW, WS-LBL and the two NBM forms are shown in Figures 1.15(a) and 1.15 (b), respectively. It can be seen in Figure 1.15 (a) that the errors for all methods are less than 10%. Additionally, the NBM with spectral averaging is more accurate than NBM with EM2C. The WS-LBL method again performs better than the two NBM approaches. The overall good performance of the NBM is again due to the higher optical thickness of CO_2.

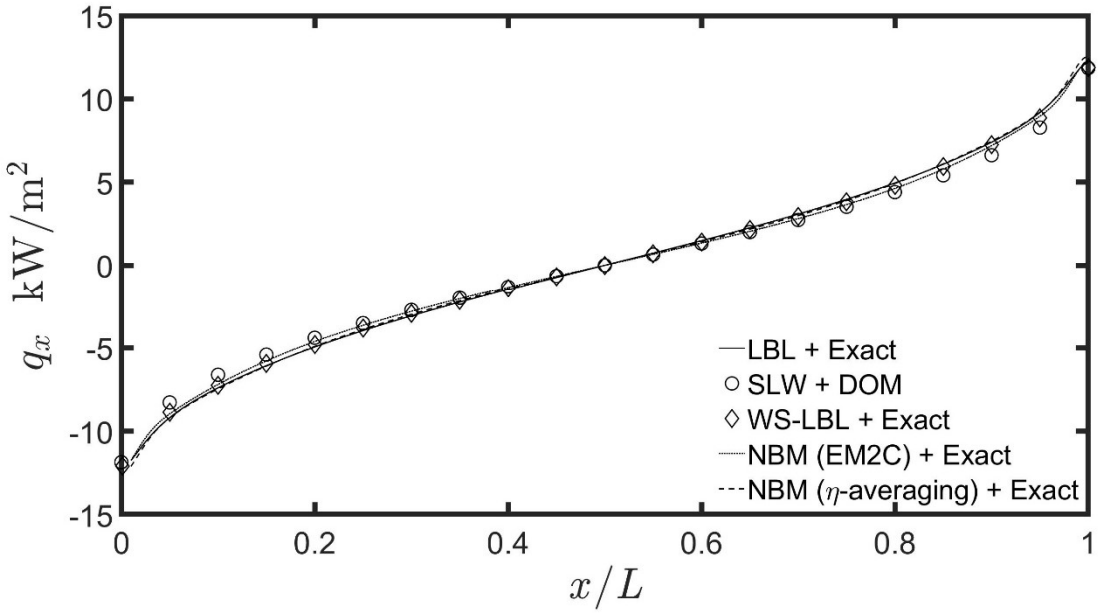

(a)

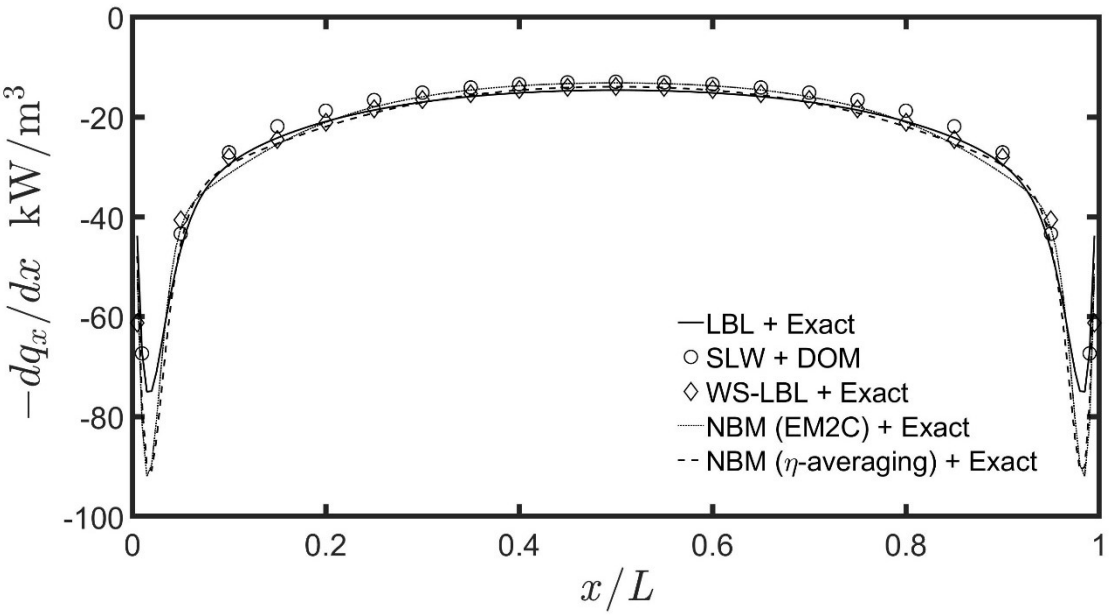

(b)

Figure 1.14 Comparison of 1-D LBL, SLW, WS-LBL and two NBM forms in combination with the exact solution for Case 3. (a) radiative fluxes q_x, and (b) radiative source terms $(-dq_x/dx)$.

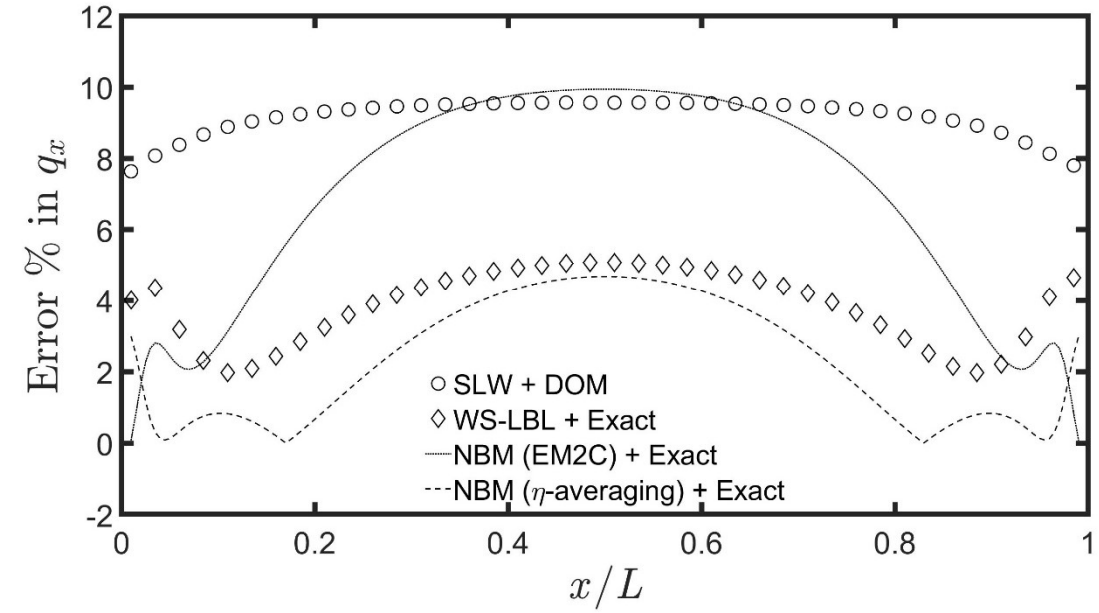

(a)

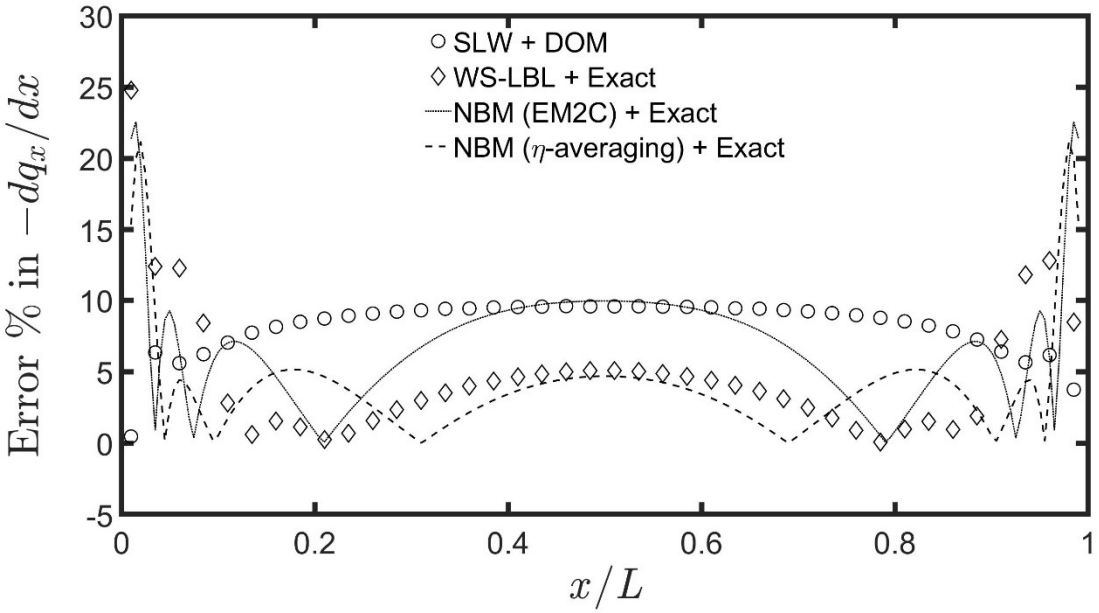

(b)

Figure 1.15 Errors in SLW, WS-LBL and the two NBM forms relative to the Exact-LBL solution for Case 3. (a) radiative fluxes q_x, and (b) radiative source terms $(-dq_x/dx)$.

1.6.5 Case 4

This is a case with uniform species mole fraction, but non-isothermal medium temperatures. The participating species is H_2O with a mole fraction of unity and a spatially varying temperature profile. The domain length $L = 0.2$ m, and the boundaries at $x = 0$ and $x = L$ are both black with temperatures of 1500 K and 300 K, respectively. The temperature profile illustrated in Figure 1.2 shows that between $x = 0$ and $x = 0.05$ m, the gas temperature decreases sharply from 1500 K to about 500 K, and thereafter decreases gradually to 300 K at the right wall. Thus, the medium is cooler compared to the left wall, which will play a crucial role in determining the flux direction, as well as whether the medium is a net emitter or absorber of radiative energy. For this case, the spatially varying H_2O temperature profile precludes an exact analytical solution of the RTE. As a result, results obtained using only DOM and CA-DOM are shown.

Figures 1.16 (a) and 1.16 (b) compare the fluxes and the source terms computed using the five spectral approaches. In Figure 1.16 (a), it can be seen that the flux is positive throughout the domain, with the implication that the hot left wall is driving the radiative fluxes along the positive-x direction. It can also be seen that for $x < 0.1$, the flux increases with x reaching a maximum, and thereafter decreases monotonically with increasing x. The increase in flux occurs because close to the left wall, the net radiative transport from the wall to the medium is the dominant mechanism, whose magnitude increases as the medium temperature decreases (for $x < 0.1$). The wall effects diminish for $x > 0.1$, as the hot-gas to cold-gas radiative transport becomes the more significant contribution. In Figure 1.16 (b), the source term, $\left(-\frac{dq_x}{dx}\right)$ is negative for $x < 0.1$, and becomes positive thereafter. Thus, the medium transitions from an emitter near the left

wall into an absorber as it moves away. The transition may be attributed to the decreasing gas temperature with distance from the left wall, so that the gas in the farther grid cells becomes a net recipient of radiative flux. For $x > 0.1$, the gas temperature approaches a nearly constant value, with the consequence that $\left(-\frac{dq_x}{dx}\right)$ also decreases and gradually approaches zero. In these figures, it is observed that the WS-LBL and SLW predictions are in good agreement with the LBL results. Among the spectral models considered, the two NBM forms deviate the most from the LBL fluxes and source terms; this behavior is due to the inherently low optical thickness of H_2O. In Figure 1.16 (a), it can be seen that the NBM radiative fluxes, after achieving a peak around $x = 0.05$ m, decrease sharply relative to LBL fluxes. The sharp fall in NBM fluxes for $x > 0.05$ may be attributed to the neglect of the correlation between the gas absorption coefficient and radiative intensity in the narrowband-averaged RTE. For the four spectral models, the errors in radiative fluxes and source terms are plotted in Figures 1.17 (a) and 1.17 (b), respectively. In Figure 1.17 (a), peak errors in the two NBM fluxes are in the 4-5% range. It can be seen that the errors in WS-LBL are significantly lower than those in NBM forms, and that the SLW method shows the best performance among the four spectral methods. In Figure 1.17 (b), the peak errors, occurring in the $x \sim 0.1$-0.2 range, are higher, which is to be expected since derivatives generally tend to amplify the errors.

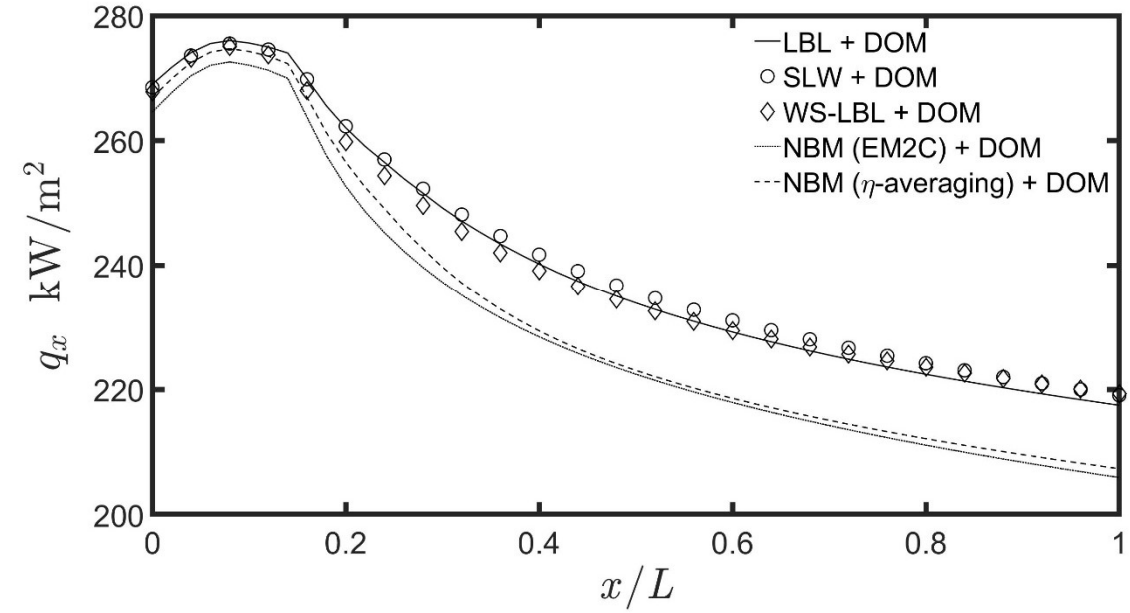

(a)

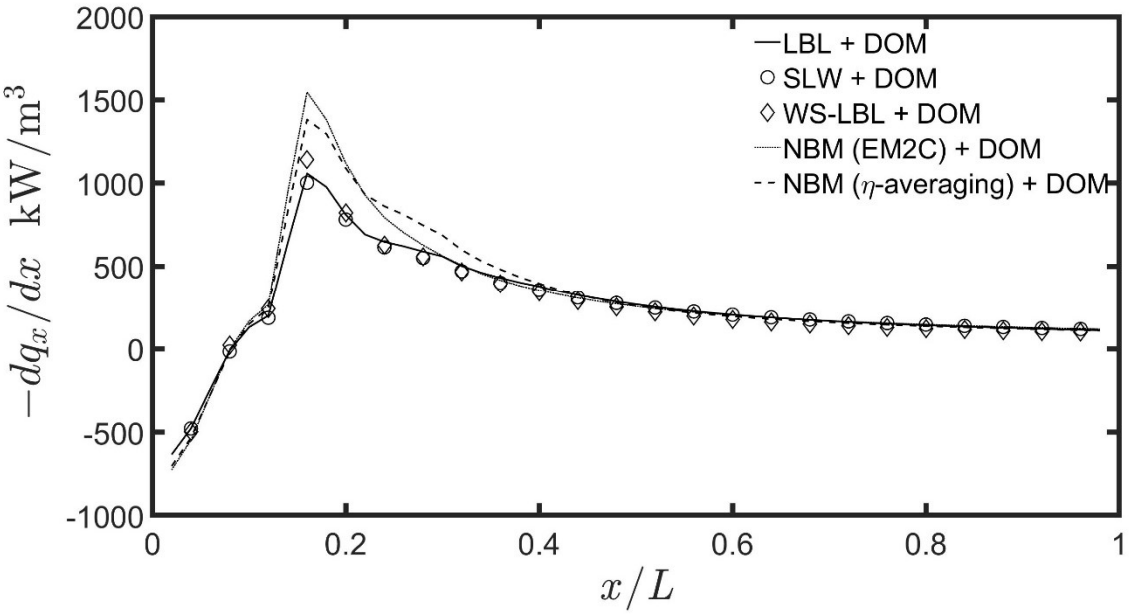

(b)

Figure 1.16 Comparison of 1-D LBL, SLW, WS-LBL and two NBM forms in combination with the DOM solution for Case 4. (a) radiative fluxes q_x, and (b) radiative source terms $(-dq_x/dx)$.

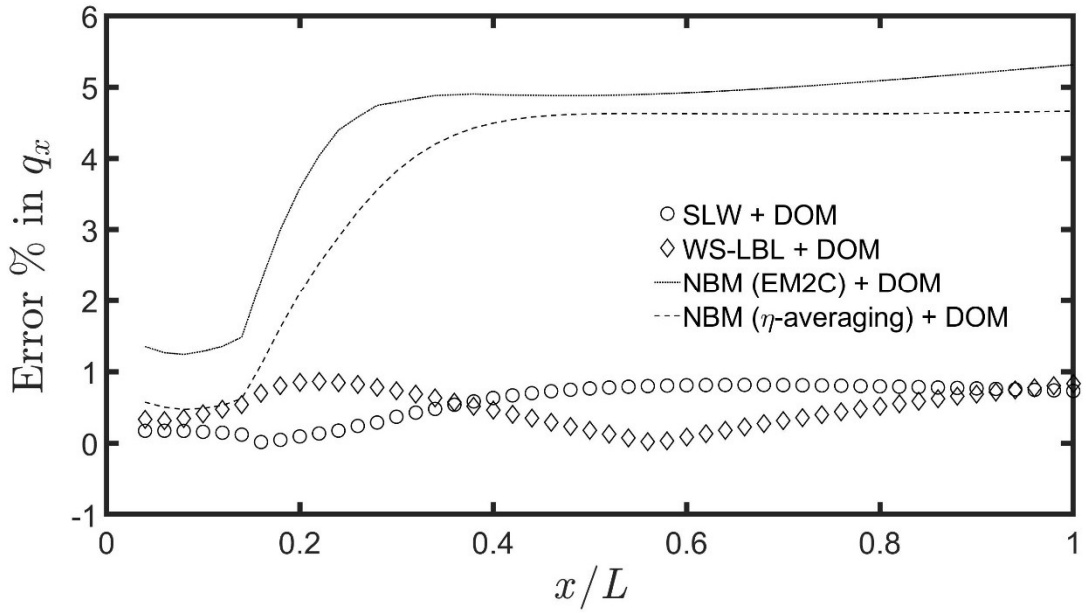

(a)

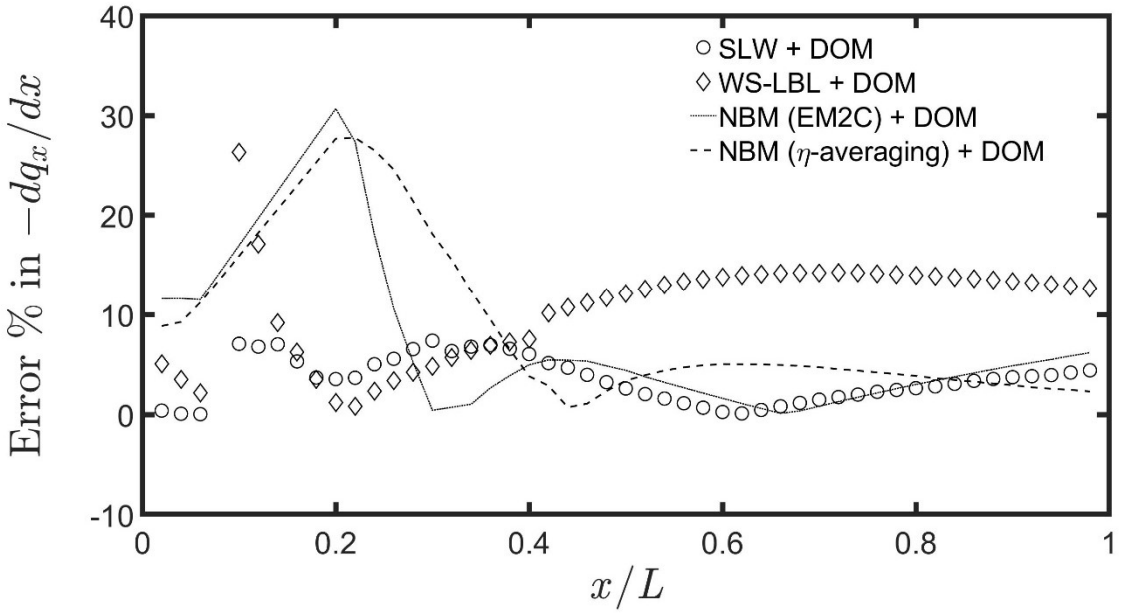

(b)

Figure 1.17 Errors in SLW, WS-LBL and the two NBM forms relative to the Exact-LBL solution for Case 4. (a) radiative fluxes q_x, and (b) radiative source terms $(-dq_x/dx)$.

1.6.6 Case 5

This case is representative of combustion in air with a non-isothermal, non-homogeneous mixture of H_2O and CO_2. The temperature and mole fraction profiles, shown in Figure 1.3, are similar to those in a diffusion flame occurring between a fuel jet and an opposing air jet [3]. The length of the domain $L = 1$ m, with the two boundaries being black at 300 K. The medium temperature increases rather quickly from ~ 300 K near the left wall to a maximum of 2000 K at $x \approx 0.14$, followed by a gradual decrease to 300 K at the right wall. The H_2O mole fraction too increases from zero at the left wall to a maximum of 0.2 at $x \approx 0.14$, and then decreases again to zero at the right wall. The CO_2 mole fraction profile is similar, but with a maximum of 0.1 at $x \approx 0.14$. Due to the spatial variations in both temperature and mole fractions, Case 5 serves as a stringent test case to investigate the performance of spectral models *vis a vis* LBL calculations.

Figures 1.18 (a) and 1.18 (b) present a comparison of the flux and the source term computed using the five spectral approaches coupled with DOM. It can be noted that the radiative flux is directed toward the left wall, *i.e.*, the negative x-direction for $x < 0.3$, but reverses direction toward the right wall for greater x. It can also be observed that the flux q_x is essentially flat for $x < 0.2$, and for $x > 0.4$. Correspondingly, in Figure 1.18 (b), $\left(-\frac{dq_x}{dx}\right) \approx 0$ for $x < 0.2$, and $x > 0.4$. In the range $0.2 < x < 0.4$, it can be seen that $\left(-\frac{dq_x}{dx}\right) < 0$, suggesting that the medium acts as a net emitter of radiative energy at these locations. It is noted from these two figures that the WS-LBL and SLW methods show the best agreement with LBL calculations. In Figure 1.18 (a), the two NBM forms show differences with the LBL results for $x < 0.2$, and for $x > 0.4$. Despite these differences, the NBM forms are in overall reasonable agreement with LBL. Although the

NBM method suffers from the errors associated with the approximation $\overline{\kappa_\eta I_\eta} \approx \bar{\kappa}_\eta \bar{I}_\eta$, the presence of CO_2 in the species mixture enhances the optical thickness of the mixture, thereby mitigating these errors. The errors in q_x and $\left(-\frac{dq_x}{dx}\right)$ for the SLW, WS-LBL and NBM are shown in figures 1.19 (a) and 1.19 (b), respectively. In Figure 1.19 (a), NBM with EM2C data has a peak error of ~ 20%, while NBM with spectral averaging shows a peak error of about ~ 10%. The WS-LBL method again shows good performance relative to the two NBM forms, and the SLW method has the lowest errors.

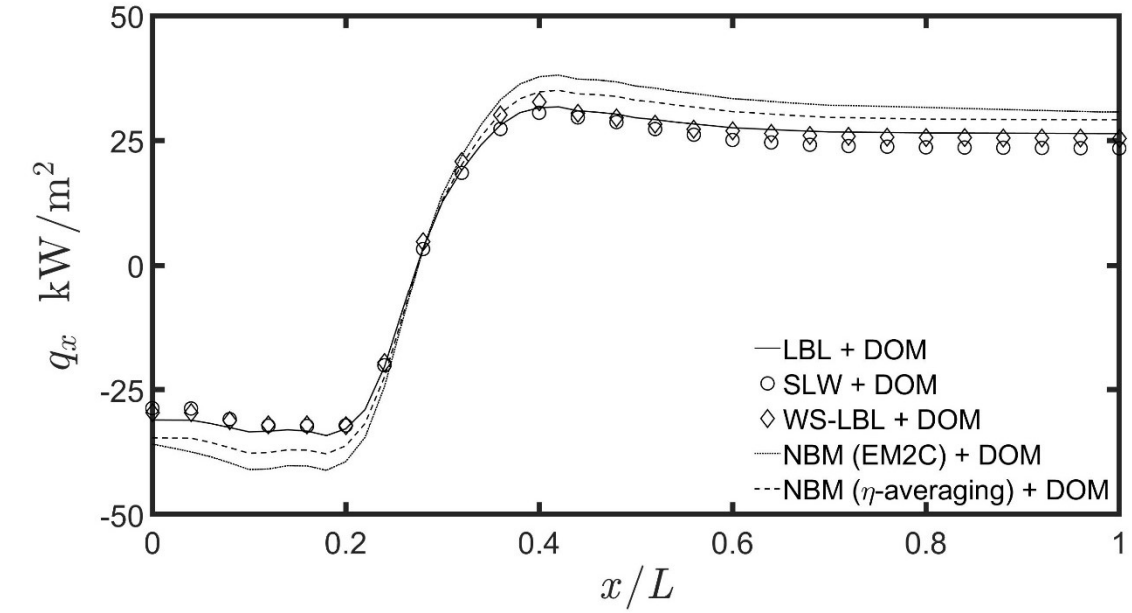

(a)

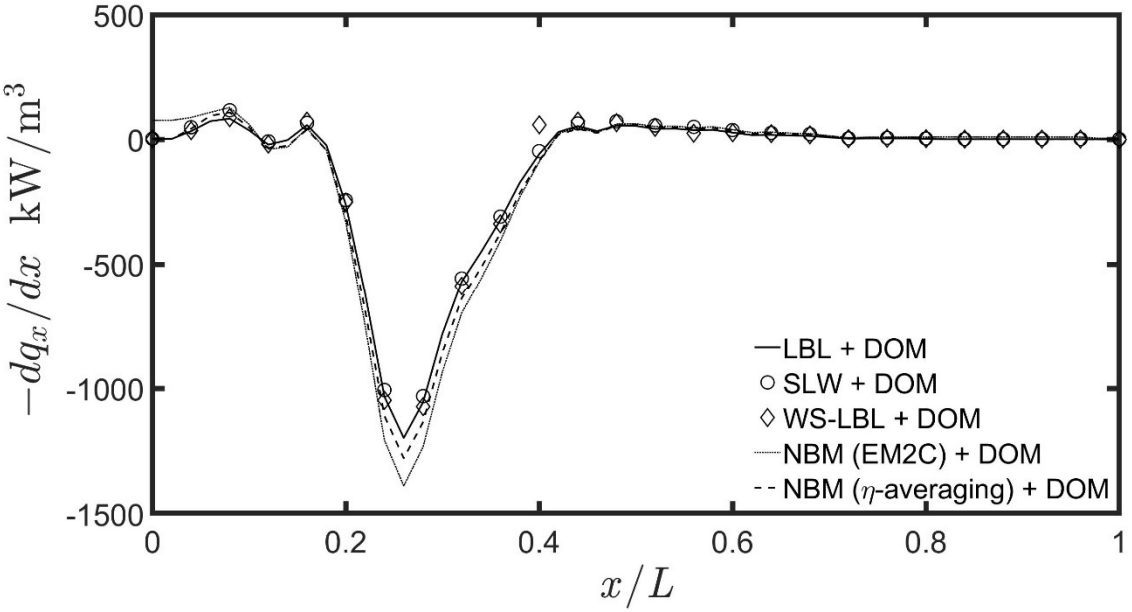

(b)

Figure 1.18 Comparison of 1-D LBL, SLW, WS-LBL and two NBM forms in combination with the DOM solution for Case 5. (a) radiative fluxes q_x, and (b) radiative source terms $(-dq_x/dx)$.

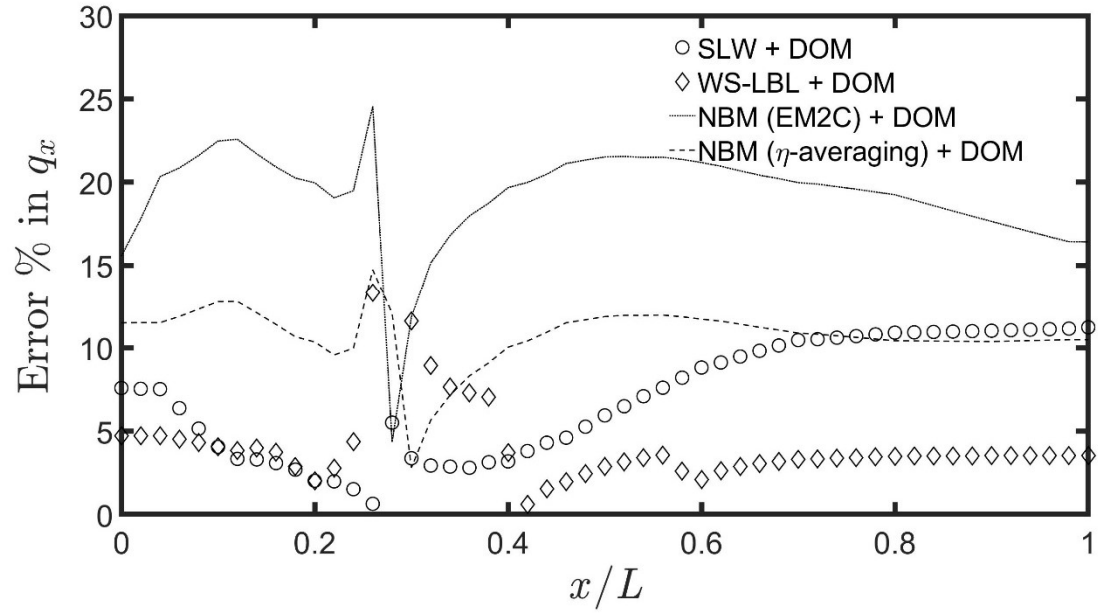

(a)

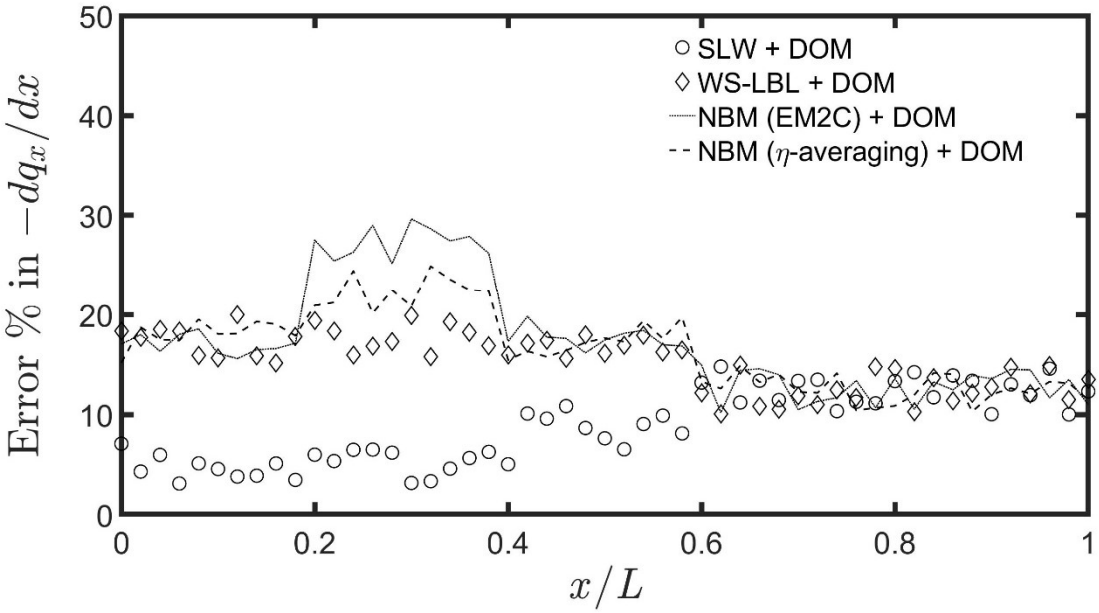

(b)

Figure 1.19 Errors in SLW, WS-LBL and the two NBM forms relative to the Exact-LBL solution for Case 5. (a) radiative fluxes q_x, and (b) radiative source terms $(-dq_x/dx)$.

1.7 Conclusions

A comprehensive investigation was undertaken of a narrow-band modeling approach based on the absorption coefficient as the fundamental radiative property. The first step in applying the NBM was to average the RTE over a narrow band giving rise to the correlation $\overline{\kappa_\eta I_\eta}$, which is approximated as $\overline{\kappa_\eta I_\eta} \approx \bar{\kappa}_\eta \bar{I}_\eta$. The accuracy of this approximation was studied analytically in the limits of high and low optical thicknesses, and the insights from the analysis were confirmed numerically. Furthermore, the WS-LBL approach was considered, which may be regarded as LBL with a wavenumber resolution equal to that of the narrow band model. The WS-LBL method does not give rise to the $\overline{\kappa_\eta I_\eta}$ correlation, thereby providing a direct and efficient means to evaluate the effects of the approximation $\overline{\kappa_\eta I_\eta} \approx \bar{\kappa}_\eta \bar{I}_\eta$ on the predictions of the NBM.

Two approaches to calculate the mean absorption coefficient $\bar{\kappa}_\eta$ were considered, namely EM2C and spectral averaging. The accuracy of the two NBM forms was investigated by comparing their predictions of radiative fluxes and source terms with those from LBL calculations, SLW method, and WS-LBL calculations. The five spectral approaches were applied to compute radiative heat transfer in conjunction with the discrete ordinates method (DOM), the control-angle discrete ordinates method (CA-DOM), and the exact analytical solution. A large number of 1-D non-gray cases were considered comprising H_2O, or CO_2, or a mixture of the two. The cases were chosen so as to investigate the effects of medium optical thickness, isothermal/non-isothermal medium temperatures, and homogeneous/inhomogeneous species mole fractions on the accuracy of the two NBM forms. For the homogeneous and isothermal H_2O enclosure Case 1a, the

behavior of the two NBM forms suggests that the approximation $\overline{\kappa_\eta I_\eta} \approx \bar{\kappa}_\eta \bar{I}_\eta$ leads to higher errors when considering a smaller domain size with a correspondingly lower optical depth. To investigate the effects of optical depth, Case 1b was considered to have the same medium properties as Case 1a, but with a longer domain length $L = 1$ m. It is seen that the performance of the NBM forms is significantly improved for Case 1b. A third enclosure, Case 1c, was also considered that has the same domain size as Case 1a, $L = 0.1$ m, but a higher medium temperature of 3000 K. This case demonstrates that the NBM performs well in an optically thin domain with a higher medium temperature.

The enclosure in Case 2 is also isothermal and homogeneous, but with CO_2 as the participating species. In contrast with the Case 1a, the two NBM forms showed good agreement with LBL, which can be attributed to the inherently high optical thickness of CO_2. Thus, it can been seen that although Case 2 has the same domain length as Case 1a, the NBM model performs significantly better in Case 2, as CO_2 is optically thicker compared to H_2O. Case 3 considered isothermal medium temperature, but inhomogeneous species mole fractions. The participating species is CO_2 with a parabolic mole fraction profile. It is observed that the profile of the radiative source term $\left(-\frac{dq_x}{dx}\right)$ has a "w" shape, which arises because of $\left(-\frac{dq_x}{dx}\right)$ gradually approaching zero, both at the walls and in the center. Case 4 considered homogeneous H_2O mole fractions, but non-isothermal medium temperatures. It is observed that the predictions of WS-LBL are in good agreement with the LBL results. The SLW method showed remarkable agreement with the LBL calculations for this non-isothermal case. Case 5 is an air-combustion case consisting of non-isothermal, inhomogeneous mixtures of H_2O and CO_2. For this case, the SLW prediction is again in excellent agreement with the LBL results. The presence

of CO_2 in the species mixture enhances the optical thickness of the mixture, thereby mitigating the errors in the NBM forms.

Chapter 2. Absorption Coefficient-Based Narrow Band Model and Its Application to the Calculation of Radiative Heat Transfer in Two-Dimensional Enclosures

2.1 Introduction

In Chapter 1, a narrow band model (NBM) based on the absorption coefficient for the calculation of radiative heat transfer in 1-D enclosures was presented. Accordingly, the principal objective of Chapter 2 is to examine the accuracy of the NBM in calculating radiative transfer in 2-D rectangular enclosures that are homogeneous and isothermal, as well as inhomogeneous and non-isothermal. The participating species considered are CO_2, H_2O or their mixture. The radiative fluxes and flux divergences predicted using the NBM are compared with those from LBL calculations, SLW method, and the WS-LBL calculations.

Recall that LBL calculations of radiative heat transfer are extremely computationally intensive due to the large number of spectral lines in the absorption spectra of gas species, as well as to the extreme fluctuations in the absorption cross-sections of spectral lines. The computational burden imposed by LBL calculations has motivated the development of approximate spectral models, which may be broadly classified into three types: (1) narrow band models [9, 10, 11]; (2) wide band models (WBMs) [13, 36]; and (3) global models [25, 22, 5, 14]. A review of spectral models and their application in solving the RTE may be found in the references [37, 38, 35]. Among the well-known narrow band models are the Elsasser NBM [9],

Goody NBM [10], and the Malkmus NBM [11]. The Elsasser, Goody and Malkmus NBMs are based on transmissivity being the basic radiative property and hence are inherently suited to solving the RTE in its integral form (for a non-scattering medium). The NBM considered in the present study is based on the absorption coefficient as the basic property so that the RTE may be solved in differential form. Among the global non-gray gas models suited to solving the differential RTE is the highly successful spectral line-based weighted sum of gray gases (SLW) method [21, 22, 27, 26, 28]. SLW method is fundamentally based on replacing the spectral radiative intensities I_η by a small number of aggregate intensities I_j. Each I_j, corresponding to a "gray gas", is obtained by integrating I_η over all such wavenumber intervals wherein the spectral absorption cross-section lies between two reference values of absorption cross-section, and then summing all the integrated intensities. An objective of the current study is also to perform a direct comparison of the SLW method with LBL calculations in 2-D enclosures.

The classical SLW model, developed by Denison and Webb [21], is a global spectral method for predicting radiative transfer in isothermal, homogeneous media. Subsequently, Denison and Webb [22] extended the classical SLW to non-isothermal media with spatial inhomogeneities in gas pressure and species concentrations. The extended method, referred to as the SLW reference approach, is fundamentally based on the assumption that the absorption cross-section is separable as $C_\eta(p, T, Y_s) = \phi(p, T, Y_s)\, \psi(\eta)$. The implication of this assumption is that the absorption cross-section spectrum of a given species has the same spectral dependence irrespective of the thermodynamic state of the medium. Subsequently, Denison and Webb [27] advanced

the inhomogeneous and non-isothermal SLW model to a mixture of two gases, which was then generalized to a mixture of many gases by Solovjov and Webb [26]. The SLW model has since been continually developed, as well as made computationally efficient through a number of studies such as [5, 23, 24, 28].

The principal objective of the study is to examine the accuracy of an absorption-coefficient-based NBM [39] in predicting radiative transport in 2-D rectangular enclosures with CO_2, H_2O and their mixture as the participating species. Homogeneous and isothermal, as well as inhomogeneous and non-isothermal enclosures are considered. The mean line-intensity to mean line-spacing ratio needed to compute the mean absorption coefficient is obtained using two approaches — from the EM2C database [19], and by averaging the LBL absorption coefficients over the narrow band. The differential RTE is numerically solved using the control angle discrete ordinates method (CA-DOM) [30], in conjunction with the two NBM approaches. Radiative transfer statistics predicted by the NBM are compared with those obtained using LBL calculations, SLW method and WS-LBL method.

The organization of this chapter is as follows. Section 2.2 presents the important aspects of the absorption-coefficient-based NBM. The CA-DOM method for the numerical solution of the RTE in 2-D domains is discussed in Section 2.3. Results obtained for the various 2-D cases considered are presented in Section 2.4. Finally, the study is summarized in the Conclusions section.

2.2 Narrow Band Model Formulation

Recall the narrow-band model formulation in Chapter 1. In this section, the salient aspects of the narrow band model developed in [39] are presented in the interest of completeness. The radiative transfer equation for a non-scattering, absorbing and emitting gas is [8]

$$\frac{dI_\eta}{ds} = \kappa_\eta I_{b\eta} - \kappa_\eta I_\eta \ , \tag{2.1}$$

where $I_\eta(s)$ is the spectral and directional radiative intensity, η is the wavenumber, s is the path length along a given direction, $I_{b\eta}$ is the spectral (and diffuse) blackbody intensity, and κ_η is the spectral absorption coefficient of the participating medium. Averaging the RTE over a narrow band of width $\Delta\eta$ provides

$$\frac{d\bar{I}_\eta}{ds} \approx \bar{\kappa}_\eta \overline{I_{b\eta}} - \bar{\kappa}_\eta \bar{I}_\eta \ , \tag{2.2}$$

where it is approximated to be $\overline{\kappa_\eta I_{b\eta}} \approx \bar{\kappa}_\eta \overline{I_{b\eta}}$, which is reasonable since $I_{b\eta}$ varies slowly over $\Delta\eta$ as compared to κ_η and I_η. In going from equation (2.1) to equation (2.2), the approximation $\overline{\kappa_\eta I_\eta} \approx \bar{\kappa}_\eta \bar{I}_\eta$ is also utilized, *i.e.*, the correlation of fluctuations in κ_η and I_η over a narrow band has been neglected. The validity of this approximation has been rigorously examined both analytically and computationally in the recent 1-D study [39]. It is demonstrated that the approximation is most accurate in optically thin and optically thick enclosures. In both LBL and WS-LBL calculations, the RTE equation is solved given by equation (2.1). In the latter, equation (2.2) is solved for the values of the absorption coefficient selected from the LBL spectrum at discrete wavenumbers separated by the same interval as the narrow-band width $\Delta\eta$. Thus, the WS-LBL calculations may be regarded as a spectrally coarse form of LBL calculations, but with

the same resolution as that of the NBM, thereby providing a convenient means to evaluate the effects of neglecting the correlation of fluctuations in κ_η and I_η.

In the 1-D study [39], the following expression is derived for the absorption coefficient averaged over the narrow band, $\bar{\kappa}_\eta$

$$\bar{\kappa}_\eta = \frac{N}{\Delta\eta}\frac{\bar{S}\ tan^{-1}\frac{\Delta\eta}{2\gamma_L}}{\left(\frac{\pi}{2}\right)} \quad . \tag{2.3}$$

Consider a narrow band of thickness 25 cm^{-1} when the ratio $\frac{\Delta\eta}{2\gamma_L} \sim O(100 - 1000)$ for CO_2 and H_2O so that it may written as $\bar{\kappa}_\eta \approx \frac{\bar{S}}{d}$. Here $d = \frac{\Delta\eta}{N}$ is the mean line spacing of the narrow band and N is the number of spectral lines contained in the narrow band. The mean absorption coefficient $\bar{\kappa}_\eta = \frac{\bar{S}}{d}$ is calculated using two approaches. The first is based on using the $\frac{\bar{S}}{d}$ values tabulated for CO_2 and H_2O by Soufiani, Taine, Riviere and coworkers at the EM2C Laboratory [17, 18, 19]. The initial versions of the EM2C database were obtained using HITRAN [6], but the more recent versions were generated based on HITEMP 2010 [7]. In the second approach, $\bar{\kappa}_\eta$ is calculated by averaging the LBL absorption coefficients in a narrow band of width $\Delta\eta$.

2.3 RTE Solution Methodology

In the prior 1-D study [39], two numerical solution methods for the RTE namely DOM and CA-DOM were considered. It was found that the radiative fluxes and flux divergences obtained using DOM were in excellent agreement with those obtained using CA-DOM for both gray and non-gray cases. Hence, CA-DOM was only used for the numerical solution of the RTE in the current 2-D study. CA-DOM is based on the discretization of direction space into small/differential solid angles referred to as control

angles, analogous to control volumes in the finite volume method (FVM). In FVM, the spatial domain is discretized into control volumes or finite volumes followed by the integration of the governing equation over a control volume. Analogously, in CA-DOM, the 4π direction space is divided into control angles $\Delta\Omega^i$, with each control angle $\Delta\Omega^i$ enveloping or surrounding the direction unit vector $\mathbf{s}^{\mathrm{i}}$. Thus, in CA-DOM, the RTE is integrated over the spatial control volume, as well as over the control angle $\Delta\Omega^i$.

For 2-D domains, the CA-DOM form of the spatio-directional intensity in a control volume p and control angle i is given by [25]

$$I_{\eta,i}^{p} = \frac{D_{x,i}^{-}\,\Delta y\, I_{\eta,i}^{W} + D_{y,i}^{-}\,\Delta x\, I_{\eta,i}^{S} + \kappa_\eta\ \Delta x\,\Delta y\,\Delta\Omega^i I_{b\eta,i}}{D_{x,i}^{+}\ \Delta y + D_{y,i}^{-}\,\Delta x + \kappa_\eta\,\Delta x\,\Delta y\,\Delta\Omega^i} \quad , \tag{2.4}$$

where $\Delta\Omega^i$ is the control angle (or solid angle) corresponding to the ith discretized direction $\mathbf{s}^{\mathrm{i}}$, $I_{\eta,i}^{W}$ and $I_{\eta,i}^{S}$ are the intensities in the control volumes to the west and south, respectively, of the current control volume p. It may be noted that "west" and "south" refer to the control volumes that are upstream of the control volume p along x and y directions, respectively. The 2-D forms of $D_{x,i}^{+}$ and $D_{x,i}^{-}$ are [25]

$$D_{x,i}^{+} = \int_{\Delta\Omega^i} \mathbf{s}^i \bullet \mathbf{n}_x^j\, d\Omega, \qquad \mathbf{s}^i \bullet \mathbf{n}_x^j > 0 \tag{2.5}$$

$$D_{x,i}^{-} = \int_{\Delta\Omega^i} |\mathbf{s}^i \bullet\ \mathbf{n}_x^j|\, d\Omega, \qquad \mathbf{s}^i \bullet \mathbf{n}_x^j < 0 \quad , \tag{2.6}$$

where $\mathbf{n}_x^j$ denotes the outward unit normal vector to the x faces of the control volume p. Similarly, $D_{y,i}^{+}$ and $D_{y,i}^{-}$ are given by

$$D_{y,i}^{+} = \int_{\Delta\Omega^i} \mathbf{s}^i \bullet \mathbf{n}_y^j\, d\Omega, \qquad \mathbf{s}^i \bullet \mathbf{n}_y^j > 0 \tag{2.7}$$

$$D_{y,i}^{-} = \int_{\Delta\Omega^i} |\mathbf{s}^i \bullet\ \mathbf{n}_y^j|\, d\Omega, \qquad \mathbf{s}^i \bullet\ \mathbf{n}_y^j < 0 \quad , \tag{2.8}$$

where $\mathbf{n}_y^j$ denotes the outward unit normal vector to the y faces of the control volume p. Further details of the CA-DOM implementation are identical to those in Chai *et al.* [30].

2.4 Results

The 2-D cases considered in this study are all based on the $1\,\mathrm{m} \times 0.5\,\mathrm{m}$ rectangular enclosure shown in Figure 2. The participating species and the medium properties for these cases are listed in Table 2.1. In Case 1, the medium is isothermal and homogeneous, while in Case 2, the medium is non-isothermal and inhomogeneous, with CO_2 as the participating species in both cases. Cases 3 and 4 are the equivalent cases with H_2O as the participating species. Case 5 consists of a non-isothermal and inhomogeneous mixture of H_2O and CO_2. In all cases, total pressure is 1 atm., and the four boundary walls are black at 300 K. Five spectral approaches were considered: (1) NBM with EM2C data, (2) NBM with spectral averaging, (3) LBL absorption coefficient spectra calculated from HITEMP 2010, (4) SLW method (with 200 gray gases), and (5) wavenumber-selective LBL (WS-LBL) calculations. The LBL calculations serve as the benchmark, while the WS-LBL calculations help infer the effects of the approximation $\overline{\kappa_\eta I_\eta} \approx \bar{\kappa}_\eta \bar{I}_\eta$ on NBM predictions.

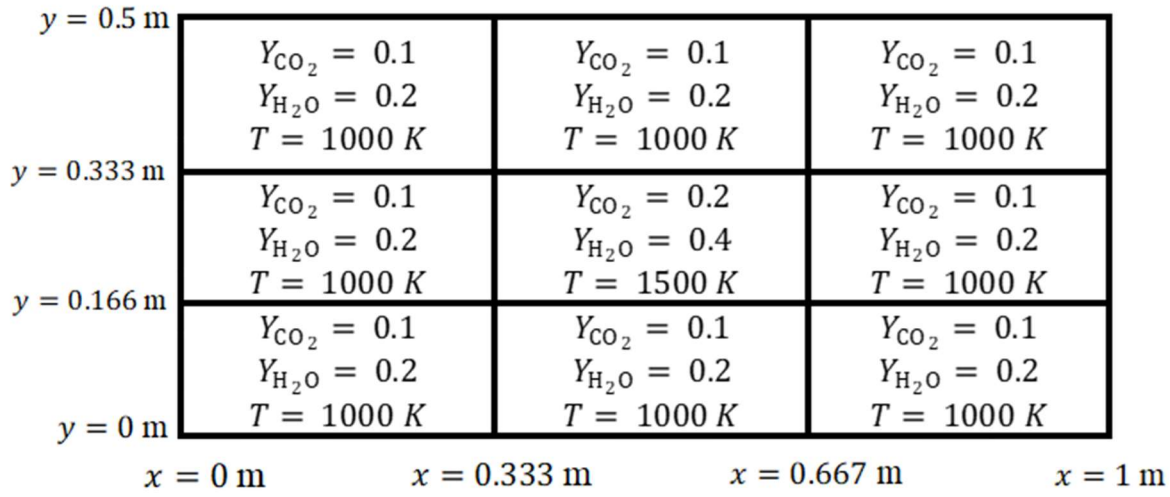

Figure 2.1 Schematic of temperature and mole fraction variation in the 2-D rectangular enclosure for Cases 2, 4, and 5.

Table 2.1 Non-gray gas cases considered in the 2-D study.

Case	Species	Domain Temperature	Wall Temperature	Pressure (atm)	H_2O Mole	CO_2 Mole
1	CO_2	1000 K	300, 300	1.0	--	0.1
2	CO_2	Step profile	300, 300	1.0	--	Step
3	H_2O	1000 K	300, 300	1.0	1.0	--
4	H_2O	Step profile	300, 300	1.0	Step	--
5	$H_2O + CO_2$	Step profile	300, 300	1.0	Step	Step

For the rectangular enclosure under consideration, the following were computed: (1) wall-normal heat fluxes along the right and top walls, *i.e.*, $q_x = \mathbf{q}\bullet\hat{\mathbf{e}}_x$ as a function of y along the right wall, and $q_y = \mathbf{q}\bullet\hat{\mathbf{e}}_y$ as a function of x along the top wall, and (2) the radiative source term $(-\partial q_x/\partial x)$ as a function of x along the horizontal centerline of the rectangle ($y = 0.25$ m), and the source term $(-\partial q_y/\partial y)$ as a function of y along the vertical centerline ($y = 0.5$ m). Here $\mathbf{q}$ is the heat flux vector, and $\hat{\mathbf{e}}_x$ and $\hat{\mathbf{e}}_y$ are the unit vectors along the x and y directions, respectively. For each case, the

statistics obtained using the five spectral approaches in conjunction with the CA-DOM method for solving the RTE are compared.

2.4.1 Case 1

The medium in Case 1 is isothermal at 1000 K, as well as homogeneous with a CO_2 mole fraction of 0.1. In Figures 2.2 (a) and (b), the wall-normal radiative fluxes along the right and top walls of the enclosure are plotted. Figure 2.2 (a) compares the radiative fluxes, q_x, as a function of y along the right wall, while Figure 2.2 (b) compares the fluxes, q_y, as a function of x along the top wall. Firstly, the positive fluxes along the two walls are indicative of radiative heat transfer from the hotter medium at 1000 K to the cooler walls at 300 K. The fluxes peak midway along the top and right walls, which is precisely where the heat transfer from the gas to the walls to be the highest is expected. This is because the two midpoints are the least influenced by (or the farthest from) the cooler neighboring walls, so that these locations are the largest recipients of net heat flux. The SLW fluxes are in excellent agreement with the LBL data both in Figures 2.2 (a) and (b). The next best agreement is seen for the WS-LBL method. The two NBM forms, NBM with EM2C and NBM with spectral averaging, do not perform as well as the WS-LBL method.

In Figures 2.3 (a) and (b), the radiative source terms computed along the horizontal and vertical centerlines of the domain are shown. Figure 2.3 (a) compares the source term $(-\partial q_x/\partial x)$ as a function of x along the $y = 0.25$ m line, and Figure 2.3 (b) compares the source term $(-\partial q_y/\partial y)$ as a function of y along the $x = 0.5$ m line. As in Figures 2.2 (a) and (b), the SLW method shows the best agreement with the LBL calculations, including at the two end points closest to the walls. The WS-LBL method,

as well as the two NBM forms, agree well with the LBL data. The good agreement seen for the flux divergences, in spite of the differences in the corresponding fluxes for WS-LBL and NBM, may be attributed to the similar shapes of the flux curves for all spectral methods considered here. Finally, it is noted that the negative values of the source terms both in Figures 2.3 (a) and (b) show that the gas is a net emitter of radiative energy. This is because the walls are significantly cooler than the gas throughout the domain. Further, the magnitude of the source term is the highest near the walls and is seen to decrease with distance from the walls.

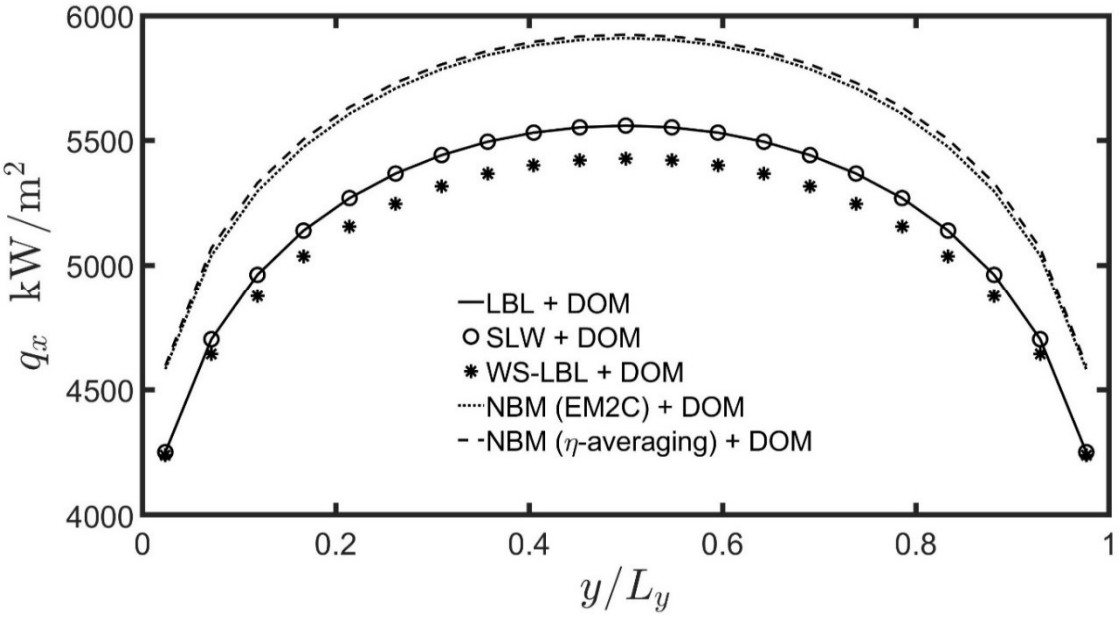

(a)

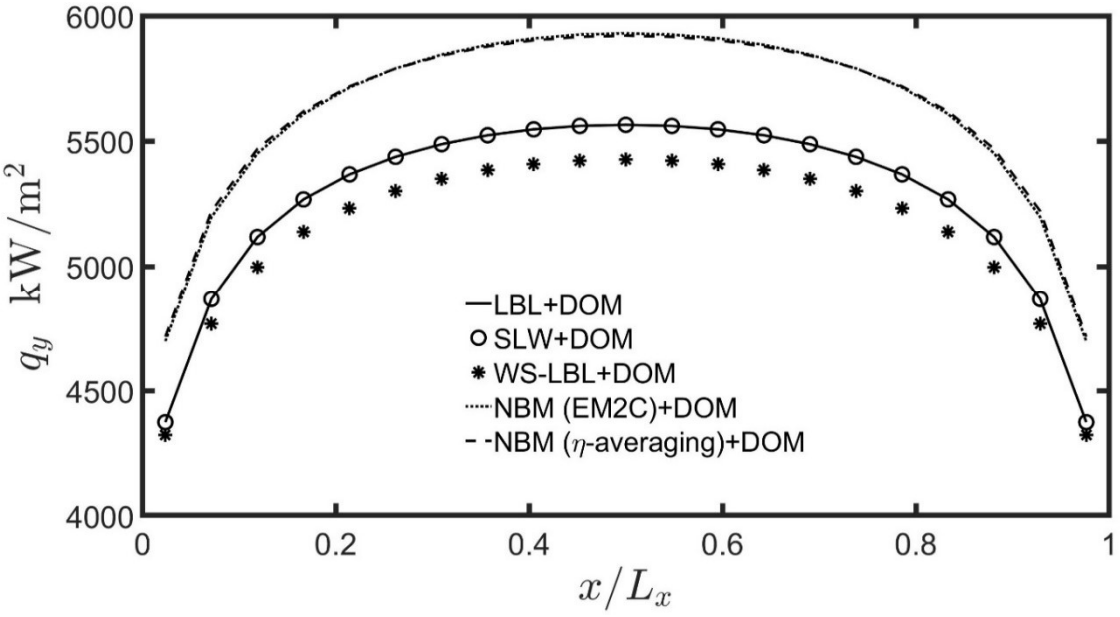

(b)

Figure 2.2 Comparison of radiative fluxes obtained using LBL, SLW, WS-LBL and the two NBM approaches for Case 1. (a) q_x as a function of y along the right wall, (b) q_y as a function of x along the top wall.

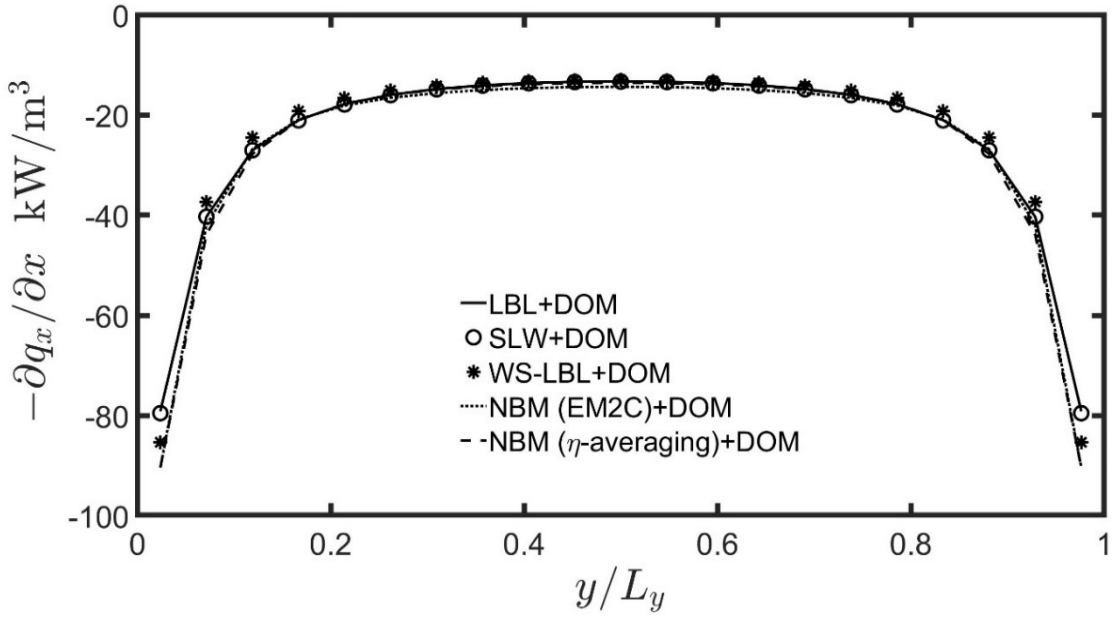

(a)

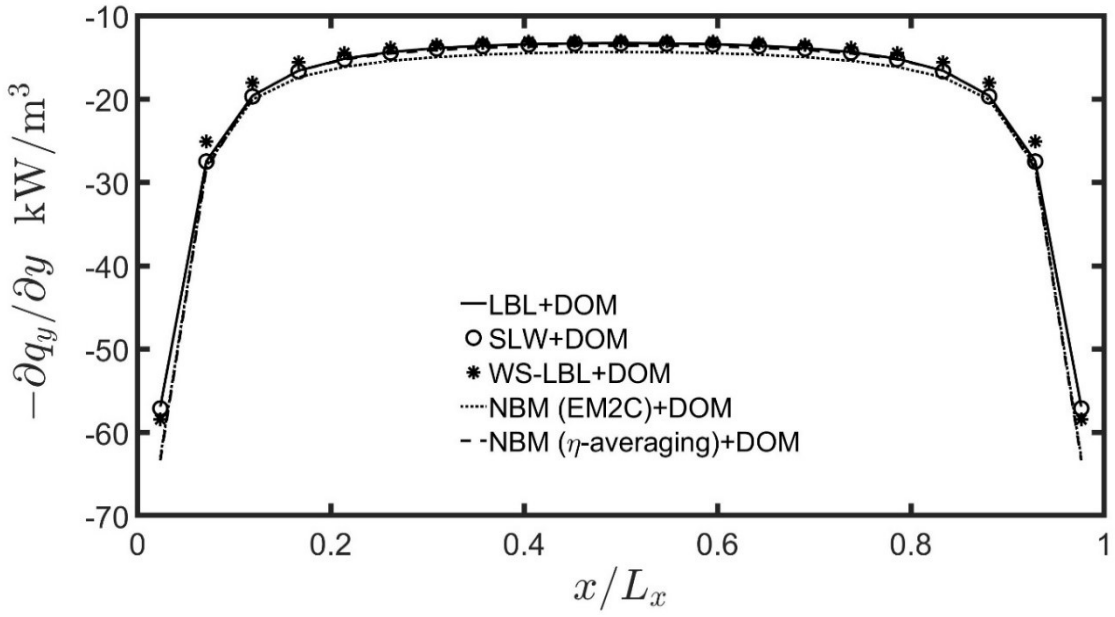

(b)

Figure 2.3 Comparison of radiative flux divergences obtained using LBL, SLW, WS-LBL and the two NBM approaches for Case 1. (a) $(-\partial q_x/\partial x)$ as a function of x along the $y = 0.25$ m centerline, and (b) $(-\partial q_y/\partial y)$ as a function of y along the $x = 0.5$ m centerline.

2.4.2 Case 2

In this case, the medium containing CO_2 is non-isothermal and inhomogeneous, as shown in Figure 2.1. The temperature undergoes step changes, both along x and y directions, from 1000 K to 1500 K and then again to 1000 K. The CO_2 mole fraction too varies abruptly from 0.1 to 0.2 and then to 0.1. As a result, Case 2 is a stringent test case for studying the accuracy of spectral models such as SLW, WS-LBL and NBM.

Figures 2.4 (a) and (b) show the wall-normal radiative fluxes along the right and top walls of the enclosure. In these figures, the SLW flux profiles are essentially identical to those of the LBL calculations. The WS-LBL calculations too show good agreement with the LBL calculations. The two NBM forms, NBM with EM2C and NBM with spectral averaging, show better agreement with LBL for this Case than in Case 1. The improved performance of the narrow band model in Case 2 may be attributed to the higher temperature, as well as to the higher CO_2 mole fraction in the central region of the rectangular enclosure (as compared to Case 1). In the 1-D study, it was demonstrated analytically and numerically that higher temperatures and higher CO_2 mole fractions mitigate the errors due to the neglect of the correlation between the gas absorption coefficient and radiative intensity in the narrowband-averaged RTE.

In Figures 2.5 (a) and (b), the radiative source terms computed along the horizontal and vertical centerlines of the rectangular enclosure are compared. It is observed that the medium transitions from being an emitter near the left and right walls *i.e.*, in the ranges $0 < x < 0.333$ and $0.666 < x < 1.0$, to an absorber away from these two walls (but before the step changes in medium properties). The gas transitions again from an absorber to an emitter in the high temperature central region of the 2-D

enclosure. The source terms computed using the SLW are in excellent agreement with the LBL data. The WS-LBL predictions are also in good agreement with the LBL calculations. The NBM with spectral averaging performs marginally better than the NBM with EM2C.

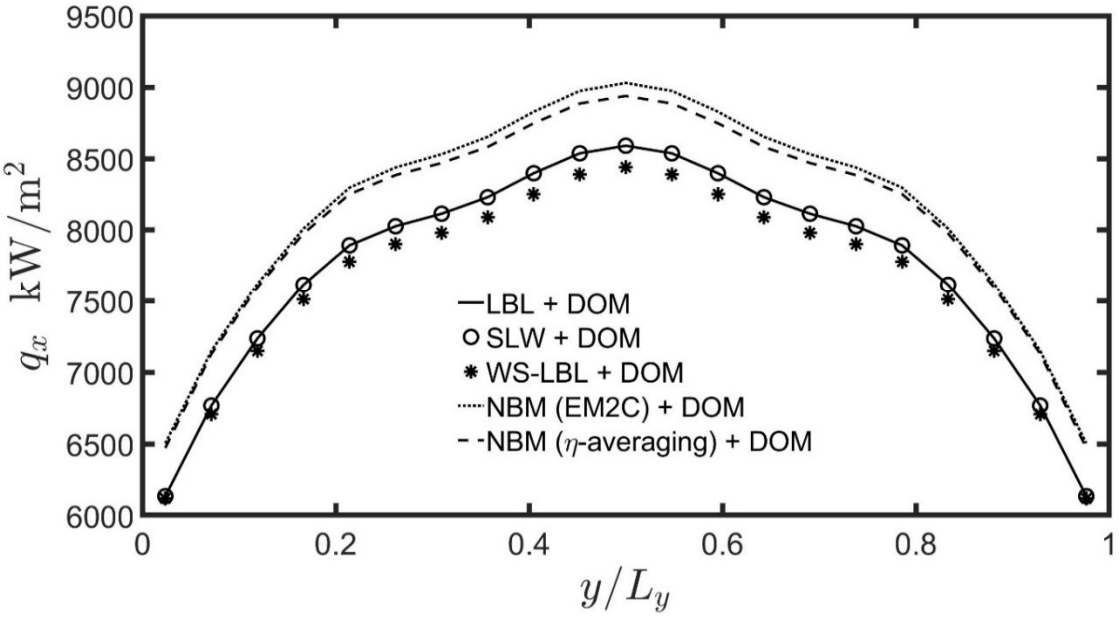

(a)

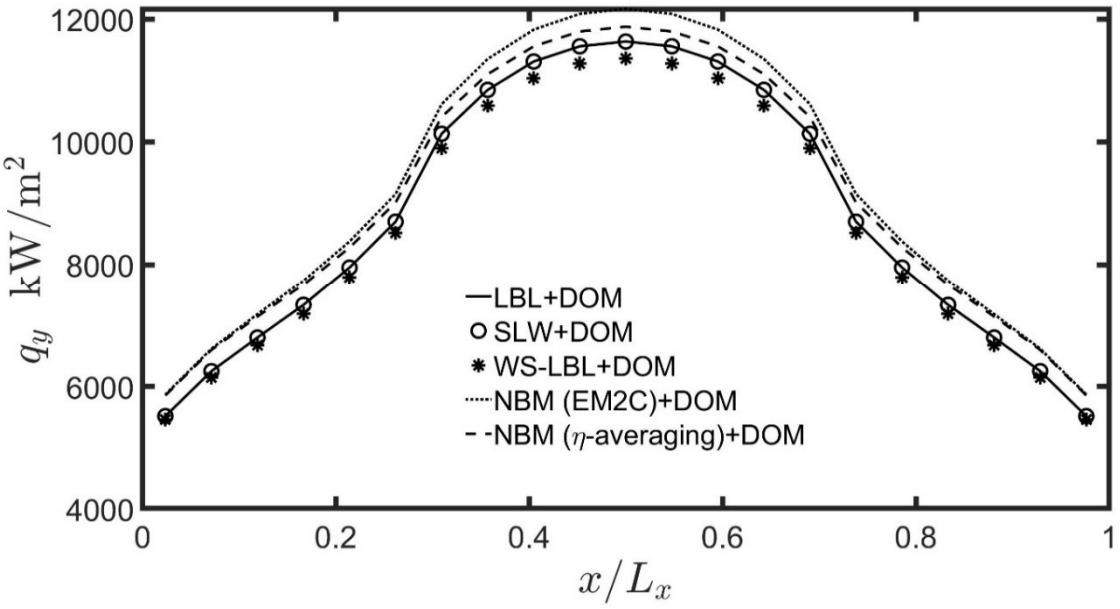

(b)

Figure 2.4 Comparison of radiative fluxes obtained using LBL, SLW, WS-LBL and the two NBM approaches for Case 2. (a) q_x as a function of y along the right wall, (b) q_y as a function of x along the top wall.

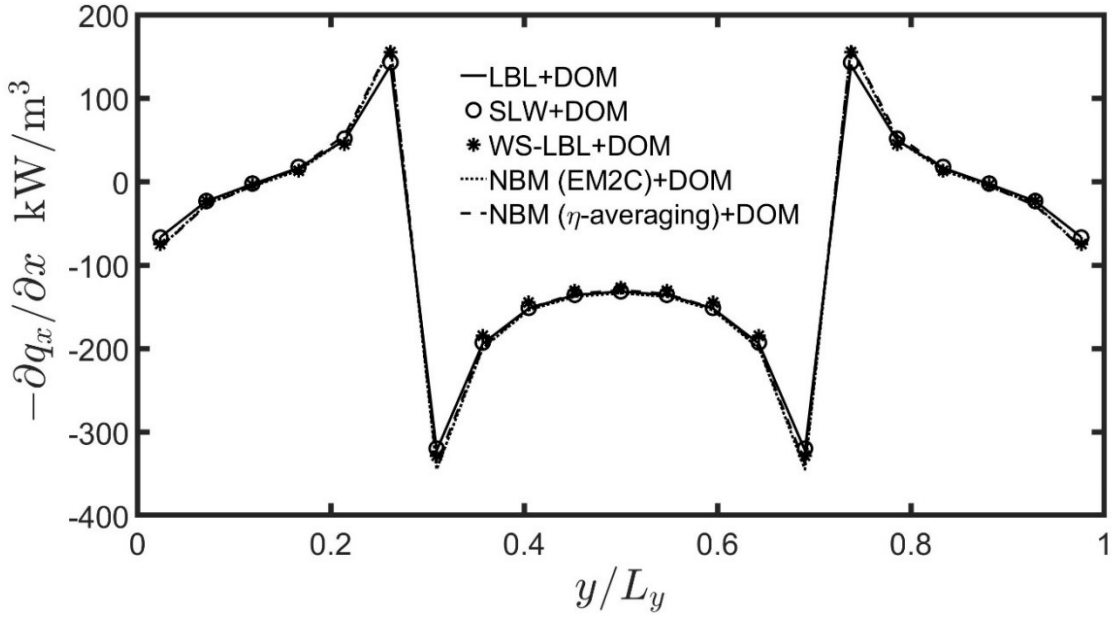

(a)

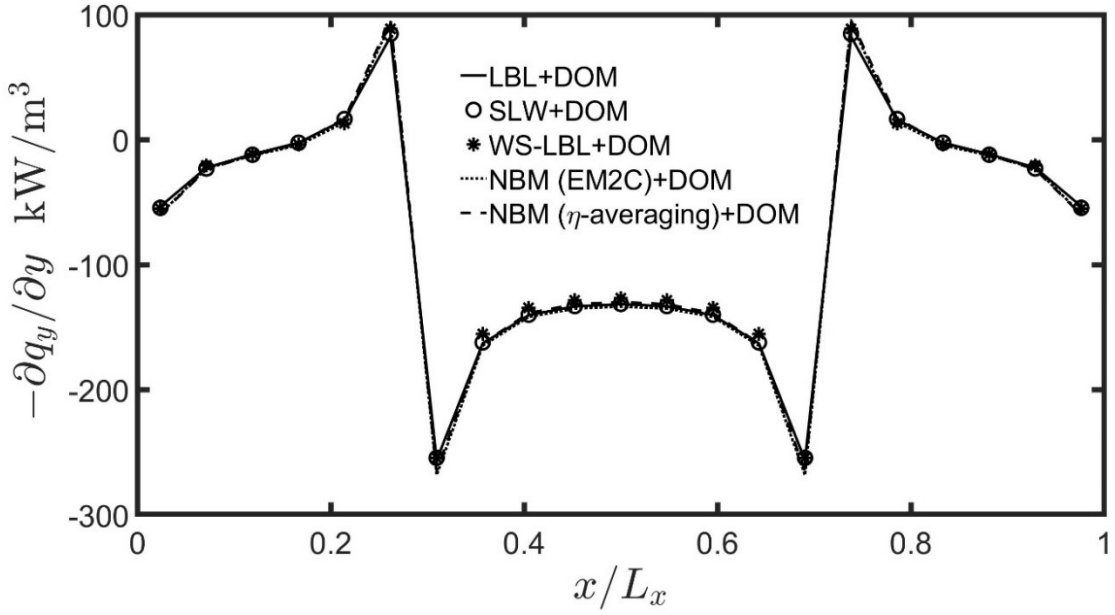

(b)

Figure 2.5 Comparison of radiative flux divergences obtained using LBL, SLW, WS-LBL and the two NBM approaches for Case 2. (a) $(-\partial q_x/\partial x)$ as a function of x along the $y = 0.25$ m centerline, and (b) $(-\partial q_y/\partial y)$ as a function of y along the $x = 0.5$ m centerline.

2.4.3 Case 3

Case 3 is an isothermal and homogeneous case with a medium temperature of 1000 K and H_2O vapor as the participating species with a mole fraction of unity. The wall-normal radiative fluxes along the right and top walls of the enclosure are shown in Figures 2.6 (a) and (b). Figure 2.6 (a) compares the radiative fluxes, q_x, as a function of y along the right wall, while Figure 2.6 (b) compares the radiative fluxes, q_y, as a function of x along the top wall. The positive fluxes along the two walls denote radiative heat transfer from the hotter medium at 1000 K to the cooler walls at 300 K. The fluxes are the highest midway along both walls because the two midpoints are the least influenced by the cooler neighboring walls. The comparison between the LBL calculations and the remaining four spectral models is similar to that in Figures 2.2 (a) and (b) for Case 1 (isothermal and homogeneous CO_2 case). The SLW fluxes are seen to be in excellent agreement with the LBL data. The WS-LBL predictions too show good agreement with the LBL data. However, the two NBM forms deviate significantly from the LBL data (similar to the trends in Figures 2.2 (a) and 2.2 (b)). The NBM model overpredicts the LBL fluxes by about 15% in Case 3 (with H_2O mole fraction of 1.0), but only by 7% in Case 1 (with CO_2 mole fraction of 0.1). Thus, it is deduced that when H_2O is the participating gas in a 2-D enclosure, even a mole fraction of unity does not make the medium optically thick enough so as to mitigate the errors due to the approximations in the narrowband-averaged RTE.

In Figures 2.7 (a) and (b), the radiative source terms are plotted along the horizontal and vertical centerlines of the domain. As in Figure 2.2 (for Case 1), the SLW and WS-LBL methods show the best agreement with the LBL calculations, including the

near-wall region. The NBM model also shows good agreement with LBL, but with small deviations near the wall. It is noted that the negative values of the source terms in Figures 2.7 (a) and (b) arise because the gas is a net emitter of radiative energy, being at a higher temperature than the walls. The magnitudes of the source terms are the highest near the walls but decrease with distance from the walls.

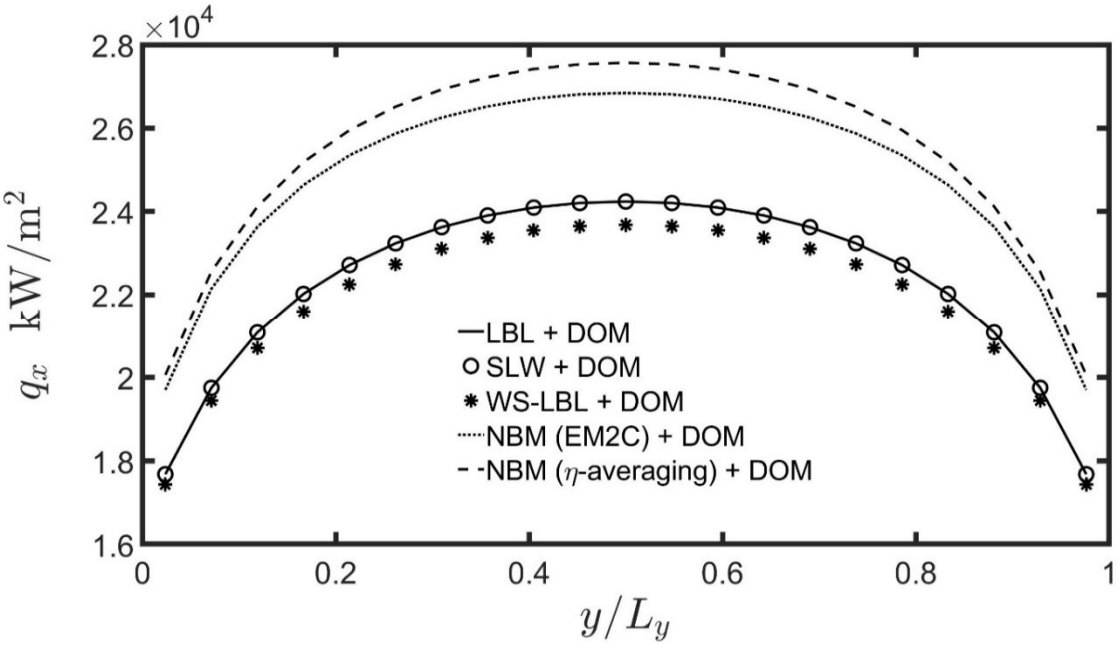

(a)

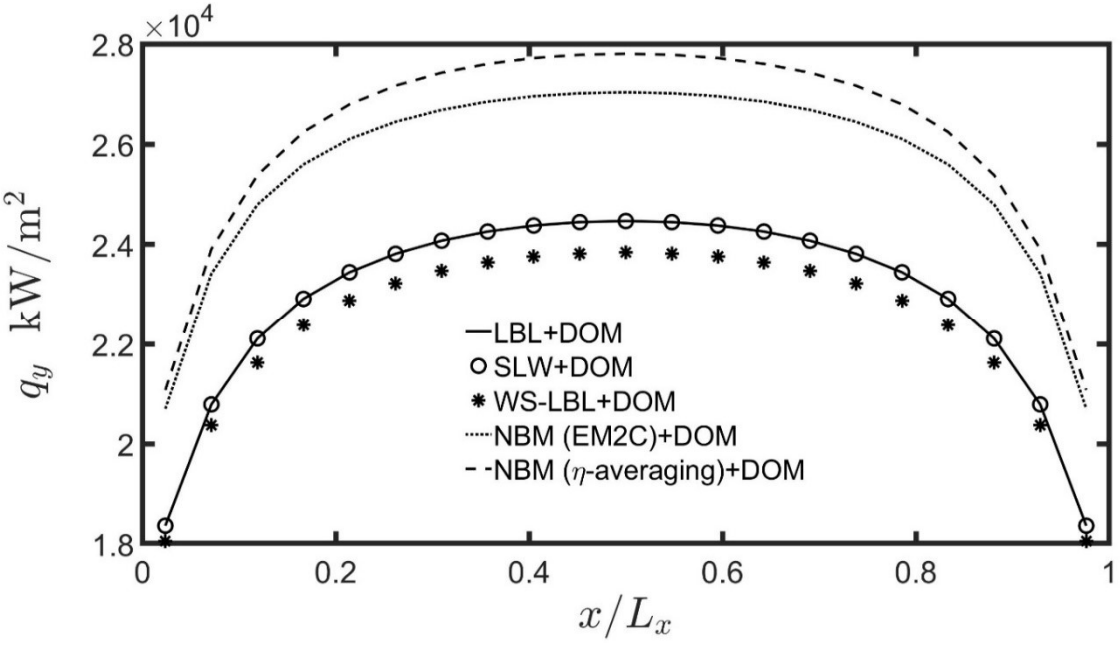

(b)

Figure 2.6 Comparison of radiative fluxes obtained using LBL, SLW, WS-LBL and the two NBM approaches for Case 3. (a) q_x as a function of y along the right wall, (b) q_y as a function of x along the top wall.

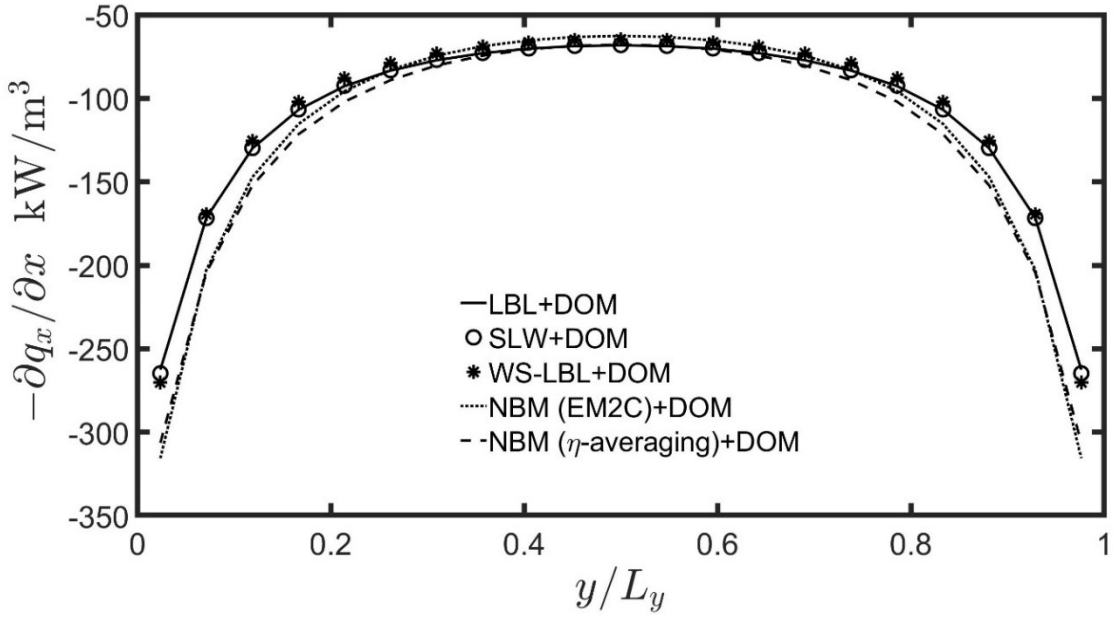

(a)

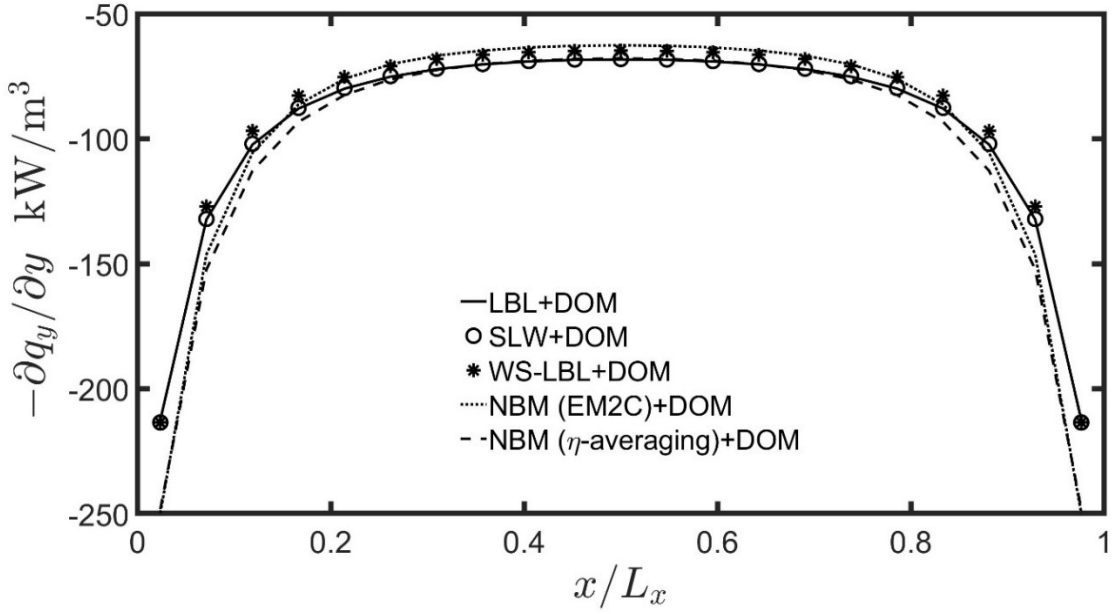

(b)

Figure 2.7 Comparison of radiative flux divergences obtained using LBL, SLW, WS-LBL and the two NBM approaches for Case 3. (a) $(-\partial q_x/\partial x)$ as a function of x along the $y = 0.25$ m centerline, and (b) $(-\partial q_y/\partial y)$ as a function of y along the $x = 0.5$ m centerline.

2.4.4 Case 4

Analogous to Case 2, a non-isothermal and inhomogeneous medium in Case 4, but with H_2O as the participating species, is considered. As shown in Figure 2.1, the medium temperature varies discontinuously from 1000 K to 1500 K and then to 1000 K. The H_2O mole fraction too undergoes step increase from 0.2 to 0.4 and then decreases back to 0.2.

Figures 2.8 (a) and (b) show the wall-normal radiative fluxes along the right and top walls. In these figures, it is noticed that the SLW method shows the best agreement with the LBL calculations, while the WS-LBL calculations slightly underperform when compared to the SLW method. The two NBM approaches differ the most from the LBL data. For Case 2 (non-isothermal, inhomogeneous CO_2), NBM showed good agreement with LBL, in contrast to the current Case 4. The higher optical thickness of CO_2, relative to H_2O, explains the improved accuracy of NBM in Case 2. In Figures 2.8 (a) and (b), the fluxes reach a maximum at the midpoints of the two walls. This is because the two midpoints are the least influenced by the neighboring cooler walls, and hence receive the highest net heat flux.

In Figures 2.9 (a) and (b), the radiative source terms computed along the horizontal and vertical centerlines of the domain are shown. Figure 2.9 (a) compares the source term $(-\partial q_x/\partial x)$ as a function of x along $y = 0.25$ m, and Figure 2.9 (b) compares the source term $(-\partial q_y/\partial y)$ as a function of y along $x = 0.5$ m. The source terms obtained using the SLW method are in excellent agreement with the LBL data, while those computed using the two NBM forms are in good agreement with the LBL data (due mainly to the similar curvatures of the flux profiles for NBM and LBL). It can

also be seen in Figures 2.9 (a) and (b) that the gas transitions from being a marginal emitter near the left and right walls to a marginal absorber away from these two walls, *i.e.*, in the x ranges $0 < x < 0.333$, and $0.666 < x < 1.0$. However, in the high temperature core of the enclosure, the gas becomes a net emitter again.

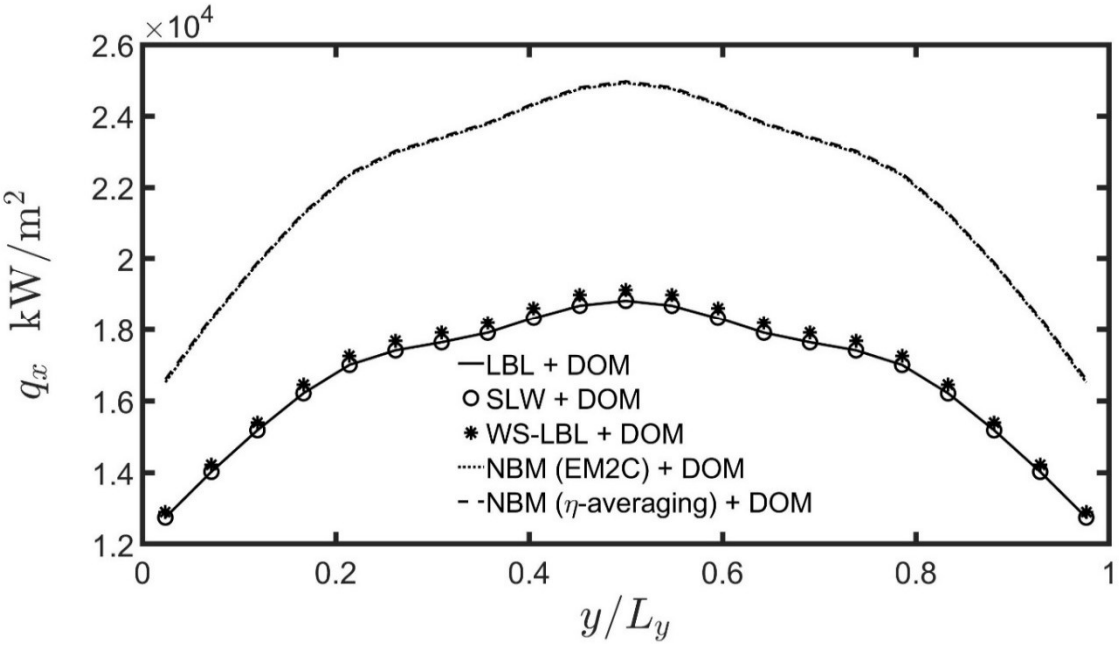

(a)

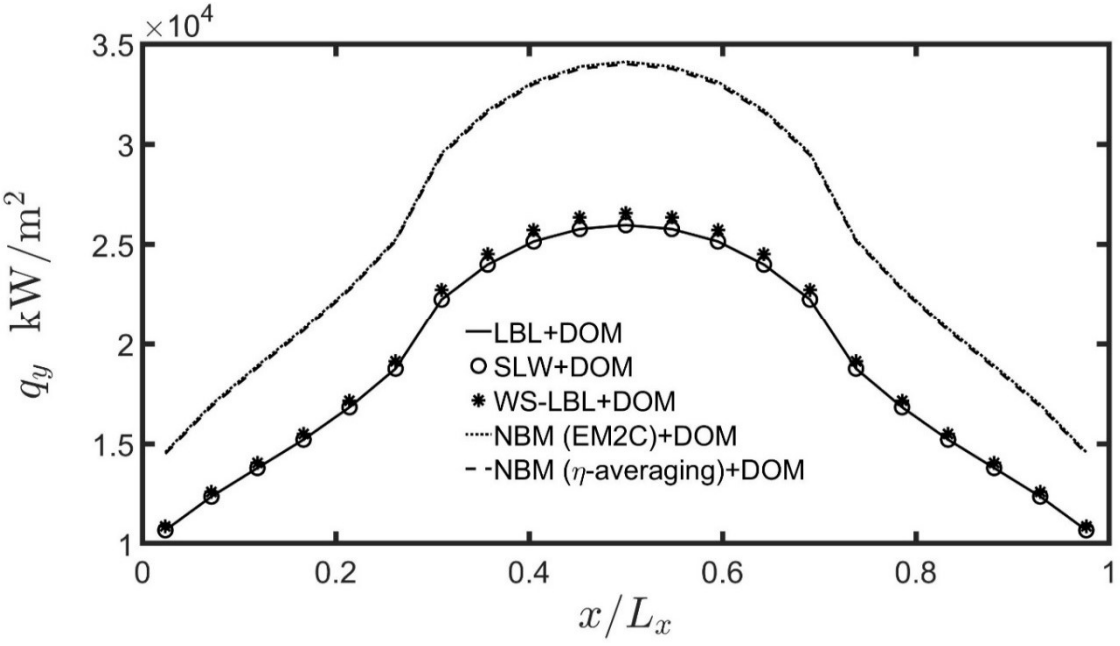

(b)

Figure 2.8 Comparison of radiative fluxes obtained using LBL, SLW, WS-LBL and the two NBM approaches for Case 4. (a) q_x as a function of y along the right wall, (b) q_y as a function of x along the top wall.

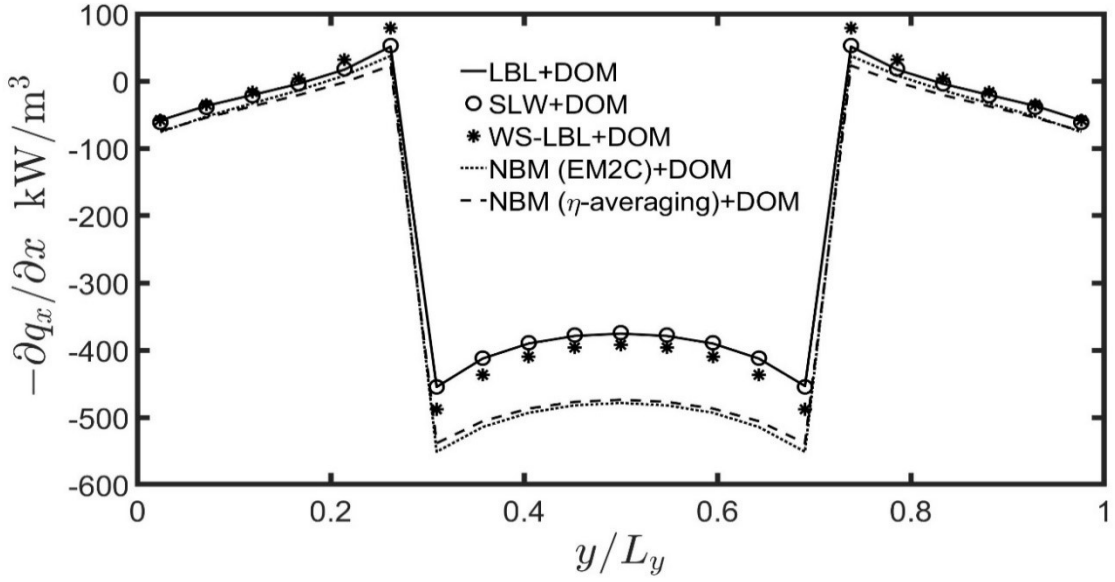

(a)

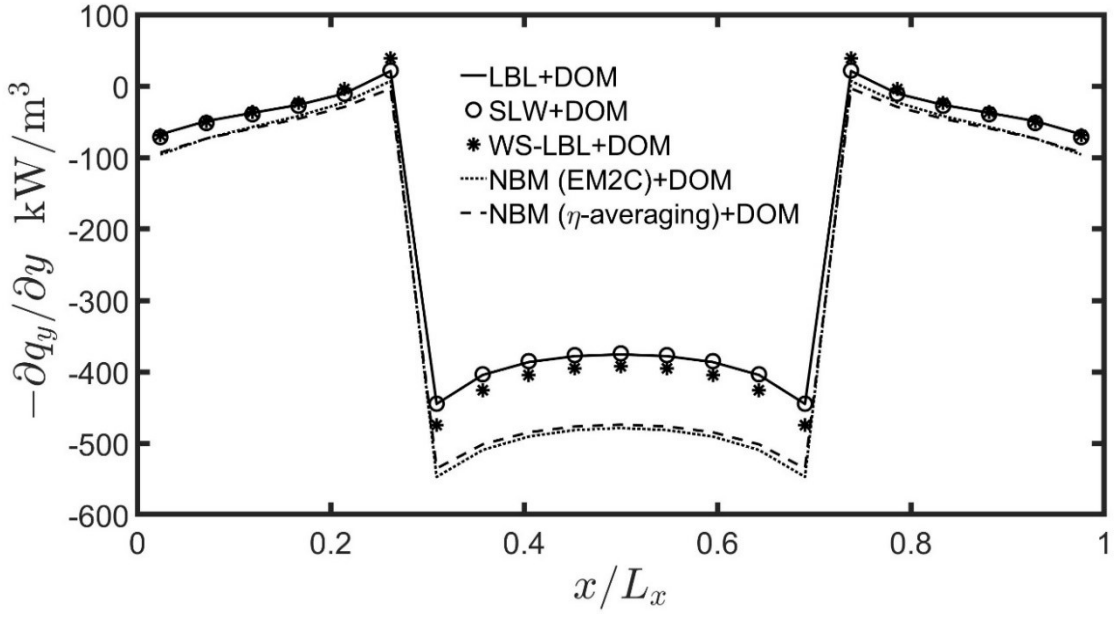

(b)

Figure 2.9 Comparison of radiative flux divergences obtained using LBL, SLW, WS-LBL and the two NBM approaches for Case 4. (a) $(-\partial q_x/\partial x)$ as a function of x along the $y = 0.25$ m centerline, and (b) $(-\partial q_y/\partial y)$ as a function of y along the $x = 0.5$ m centerline.

2.4.5 Case 5

In this final case, a non-isothermal and inhomogeneous mixture of CO_2 and H_2O is considered. Case 5 is essentially a combination of Case 2 and Case 4, as the mole fractions of CO_2 and H_2O are the same as in Case 2 and Case 4. The wall-normal radiative fluxes along the right and top walls are presented in Figure 10. In Figures 2.10 (a) and (b), it is noticed that the SLW and WS-LBL predictions of the wall fluxes are both in excellent agreement with the LBL calculations. As compared to Case 4, the two NBM forms agree better with the LBL data due mainly to the presence of CO_2 in the gas mixture. In Figures 2.11 (a) and (b), the radiative source terms along the horizontal and vertical centerlines of the domain are compared. The source terms obtained from the SLW and WS-LBL calculations agree very well with the LBL data, while those computed using the two NBM forms are in good agreement with LBL. The role of the medium as an emitter/absorber is qualitatively similar to that in Case 4, suggesting that H_2O has a dominant effect on the radiative transport in the enclosure.

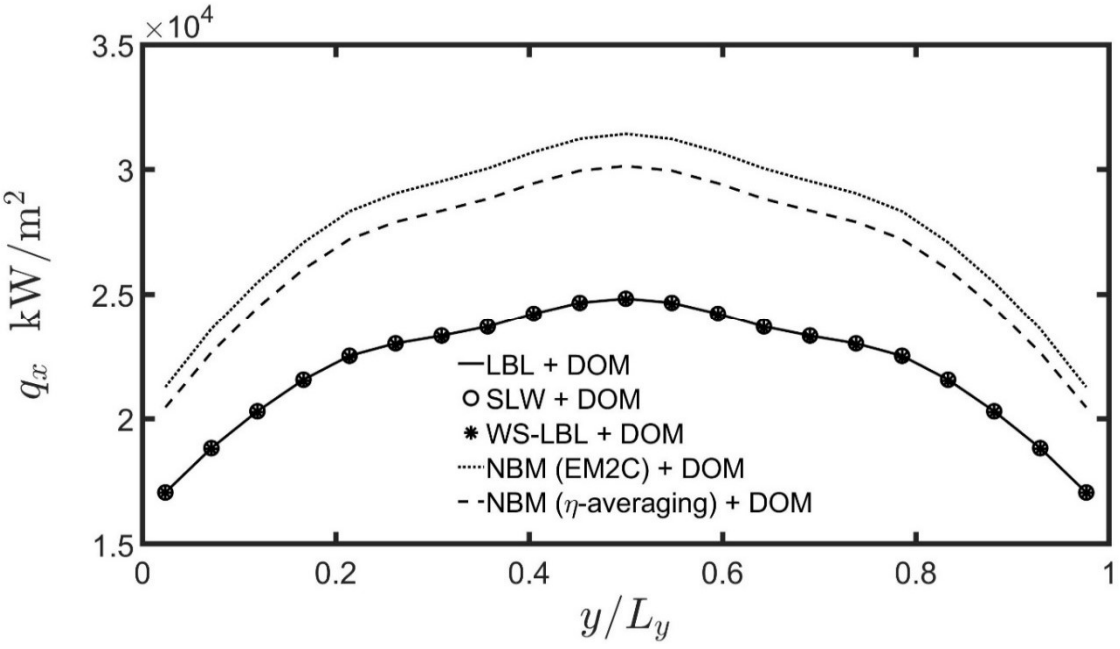

(a)

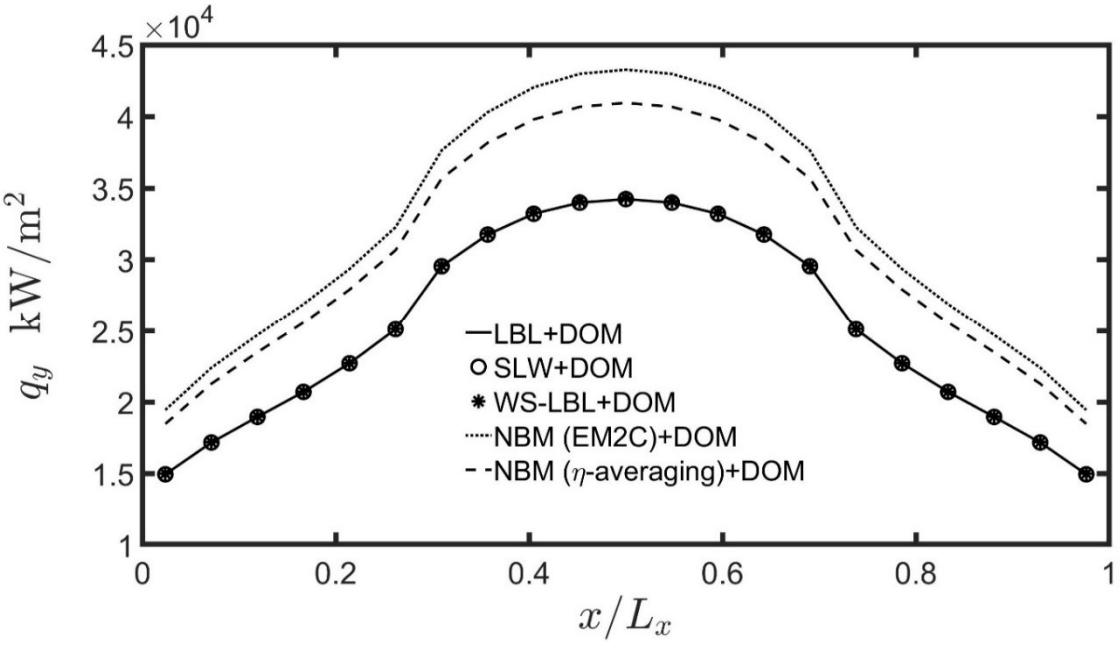

(b)

Figure 2.10 Comparison of radiative fluxes obtained using LBL, SLW, WS-LBL and the two NBM approaches for Case 5. (a) q_x as a function of y along the right wall, (b) q_y as a function of x along the top wall.

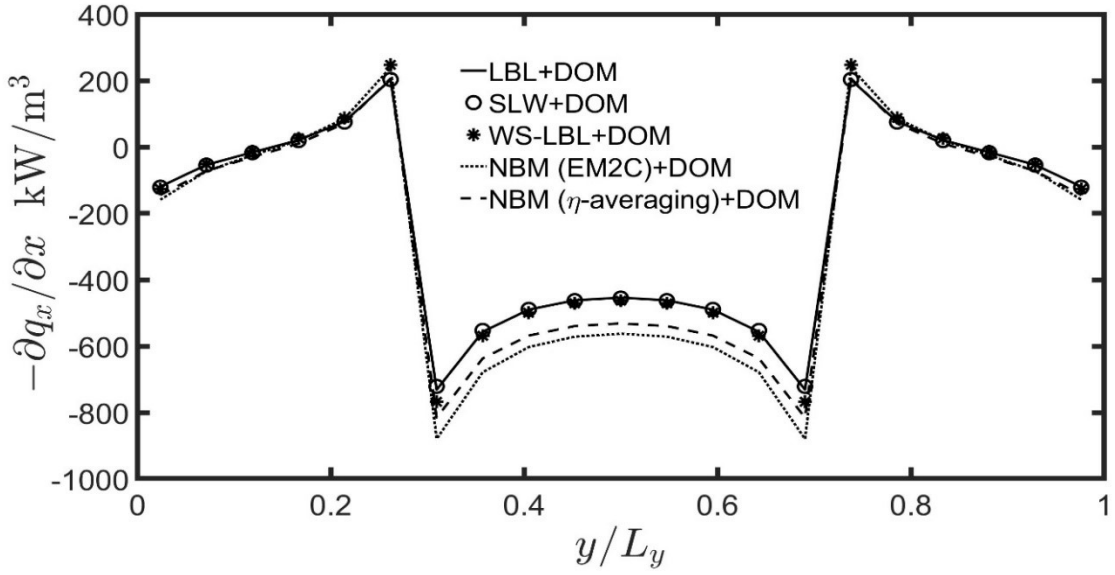

(a)

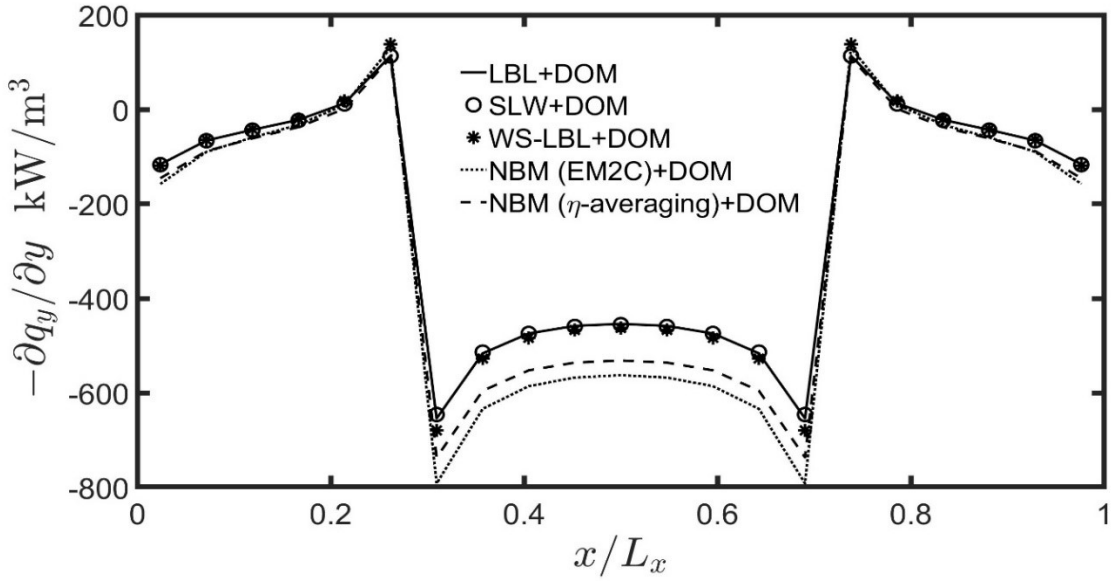

(b)

Figure 2.11 Comparison of radiative flux divergences obtained using LBL, SLW, WS-LBL and the two NBM approaches for Case 5. (a) $(-\partial q_x/\partial x)$ as a function of x along the $y = 0.25$ m centerline, and (b) $(-\partial q_y/\partial y)$ as a function of y along the $x = 0.5$ m centerline.

2.5 Conclusions

In this study, a previously developed narrow band model was extended to 2-D enclosures and examined the model accuracy through comparison with LBL and SLW methods. A number of 2-D non-gray cases were considered comprising CO_2, H_2O, or a mixture of the two gases. The cases were chosen so as to investigate the effects of isothermal/non-isothermal medium temperatures and homogeneous/inhomogeneous species mole fractions on the accuracy of the two NBM forms. The SLW method consistently showed excellent agreement with the LBL calculations. The WS-LBL calculations too were in good to excellent agreement with the LBL calculations. As in the 1-D study, the narrow band model showed improved performance in optically thick media, wherein the effects of the neglect of the correlation of absorption coefficients and radiative intensities are mitigated.

Chapter 3. Radiative Transfer Equation Solution Methodologies

3.1 Introduction

This chapter is an extension of Sections 1.5 and 2.3, where the Radiative Transfer Equation (RTE) solution methodologies are further defined to include the exact analytical solution, the Discrete Ordinates Method (DOM), and the Control-Angle Discrete Ordinates Method (CA-DOM). First, the radiation source term in the energy equation is discussed. Next, the overall solution methodology to the RTE is discussed. Lastly, the generalized boundary conditions are defined, followed by the development of the exact, DOM, and CA-DOM methodologies.

3.2 Radiation Source Term in Energy Equation

The energy equation written in enthalpy form is given below:

$$\frac{\partial(\rho c_p H)}{\partial t} + \nabla \bullet (\rho \mathbf{u} H) = \nabla \bullet (k \nabla T) + \nabla \bullet (\mathbf{u} \bullet \boldsymbol{\tau}) - \nabla \bullet \mathbf{q}_{rad} \ , \tag{3.1}$$

where H is the total enthalpy and $-\nabla \bullet \mathbf{q}_{rad}$ is the source term due to radiation. For a non-gray, absorbing and emitting gas, $-\nabla \bullet \mathbf{q}_{rad}$ may be written as

$$\nabla \bullet \mathbf{q}_{rad} = \int_{\eta=0}^{\infty} \int_{4\pi} \left[\kappa_\eta I_{b\eta}(\mathbf{x}) - \kappa_\eta I_\eta(\mathbf{x}, \hat{\mathbf{s}})\right] d\Omega \, d\eta \ , \tag{3.2}$$

where the integration is over the wavelength space and over the total solid angle, Ω, of 4π steradians, $I_\eta(\mathbf{x}, \hat{\mathbf{s}})$ is the spectral radiation intensity at the spatial location $\mathbf{r}$ along the direction $\hat{\mathbf{s}}$ and $I_{b\eta}(\mathbf{x})$ is the spectral blackbody intensity at the location $\mathbf{x}$ and is

represented by Planck's function. It is to be noted that for a gray gas, the wavelength dependence of radiative intensity is integrated out.

The primary equation that governs the intensity of radiative heat transfer, I, through participating media is the RTE. Solving the RTE to determine the radiant intensity is more involved than solving equations governing standard conduction or convection. This is because of several complexities inherent in the RTE due to (1) the dependence of radiant intensity, I, not only on the spatial location, $\mathbf{x}$, but also on wavelength of the radiation, η, and on the direction of radiation, $\hat{\mathbf{s}}$; (2) the dependence of the participating medium properties, such as the absorption and scattering coefficients, on direction $\hat{\mathbf{s}}$ (*i.e.,* anisotropy) and wavelength η; and (3) the need to couple the radiant intensity and the broader thermal (enthalpy or temperature) equation as shown above in equations (3.1) and (3.2). There are many numerical techniques for solving the RTE, to include ray tracing methods such as the discrete transfer model and the DOM, CA-DOM, Monte-Carlo methods, and zonal methods.

3.3 Overview of Solving the RTE

The steady, spectral (*i.e.*, wavelength dependent) radiative transfer equation for an emitting, absorbing and scattering non-gray gas can be written as:

$$\frac{\partial I_\eta(\mathbf{x},\hat{\mathbf{s}})}{\partial s} = \kappa_\eta(\mathbf{x}) I_{b\eta}(\mathbf{x}) - \kappa_\eta(\mathbf{x}) I_\eta(\mathbf{x},\hat{\mathbf{s}}) + \frac{\sigma_s(\mathbf{x})}{4\pi}\int_{4\pi} I(\mathbf{x},\hat{\mathbf{s}}')\phi(\mathbf{x},\hat{\mathbf{s}}' \rightarrow \hat{\mathbf{s}})\, d\Omega' , \qquad (3.3)$$

where I_η is the spectral intensity along a line of sight vector $\hat{\mathbf{s}}$, $\mathbf{x}$ is the spatial location at which the radiative intensity is to be computed, p is the in-scattering phase function, Ω' is the solid angle enveloping the direction $\hat{\mathbf{s}}'$, and $I_{b\eta}$ is the Planck's function. The spectral absorption coefficient is κ_η and the scattering term is $\frac{\sigma_s(\mathbf{x})}{4\pi}\int_{4\pi} I(\mathbf{x},\hat{\mathbf{s}}')\phi(\mathbf{x},\hat{\mathbf{s}}' \rightarrow$

$\hat{\mathbf{s}}$) $d\Omega'$. For a gray gas, the wavenumber (η) dependence drops out and only one equation needs to be solved for every $\hat{\mathbf{s}}$. The physics behind the terms in equation (3.3) can be understood by looking at a 1-D schematic of radiation in a participating medium, shown in Figure 3.1.

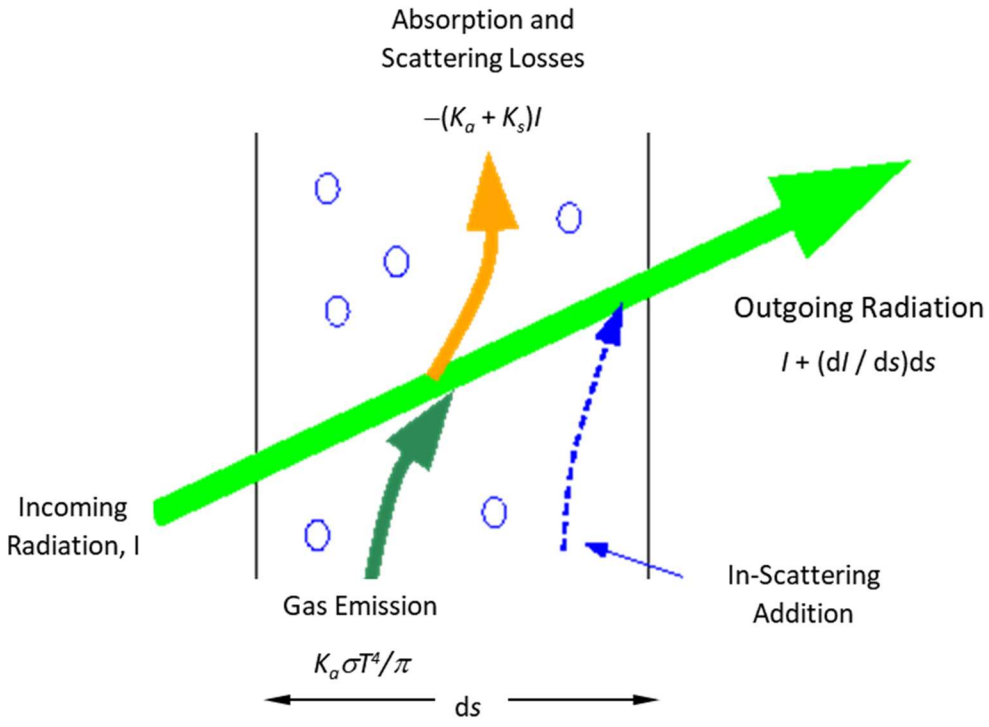

Figure 3.1 Schematic of radiation processes in a 1-D participating medium.

From equation (3.3), it can be seen that radiation intensity, I, depends on six independent variables: location in space, $\mathbf{x}$ (3); radiation direction vector $\hat{\mathbf{s}}$ (two for θ and ϕ determining the solid angle); and wavelength η (1).

There are various steps required to compute the RTE solution. The following steps described in this section are generalized and further detailed steps are included in latter sections and chapters. Figure 3.2 shows the breakdown of solving the RTE

cases discussed in previous chapters. To solve for the RTE, there must be a numerical methodology to solve the RTE in addition to the absorption coefficient, whether it is based on line-by-line (LBL) or on a model.

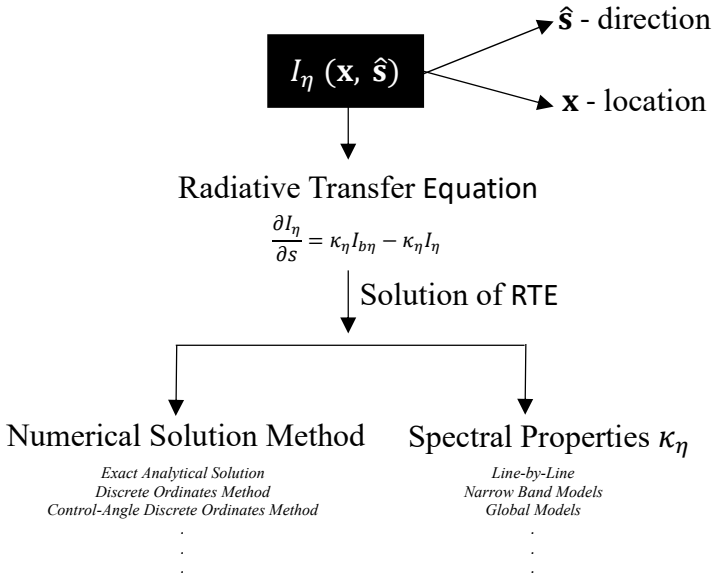

Figure 3.2 General construct of solving the RTE.

Figure 3.3 illustrates the general flow of solving the RTE. Key changes in the program are in calculating the absorption coefficient with respect to LBL vs. models and in calculating the positive and negative intensities for the different solver. Figure 3.3 shows a more detailed overall RTE 1-D program flow. This is the general 1-D RTE code schematic for most of the exact analytical solution method, DOM, and CA-DOM cases and is generally valid for the 2-D cases. Most RTE cases discussed follow the schematic flow with changes mostly in the intensity calculation loops.

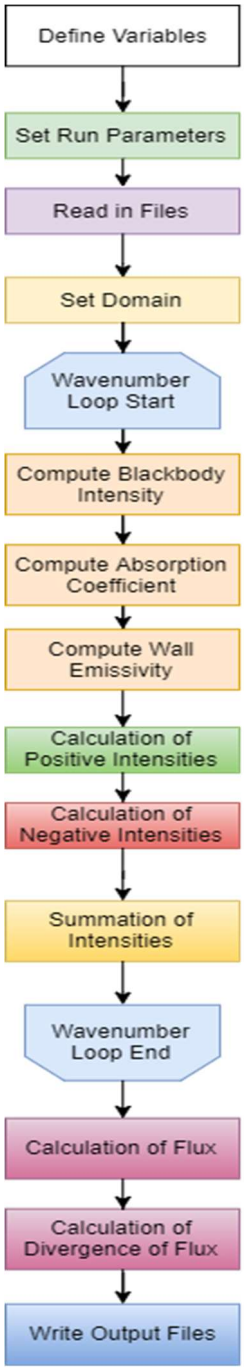

Figure 3.3 Program schematic for solving the RTE.

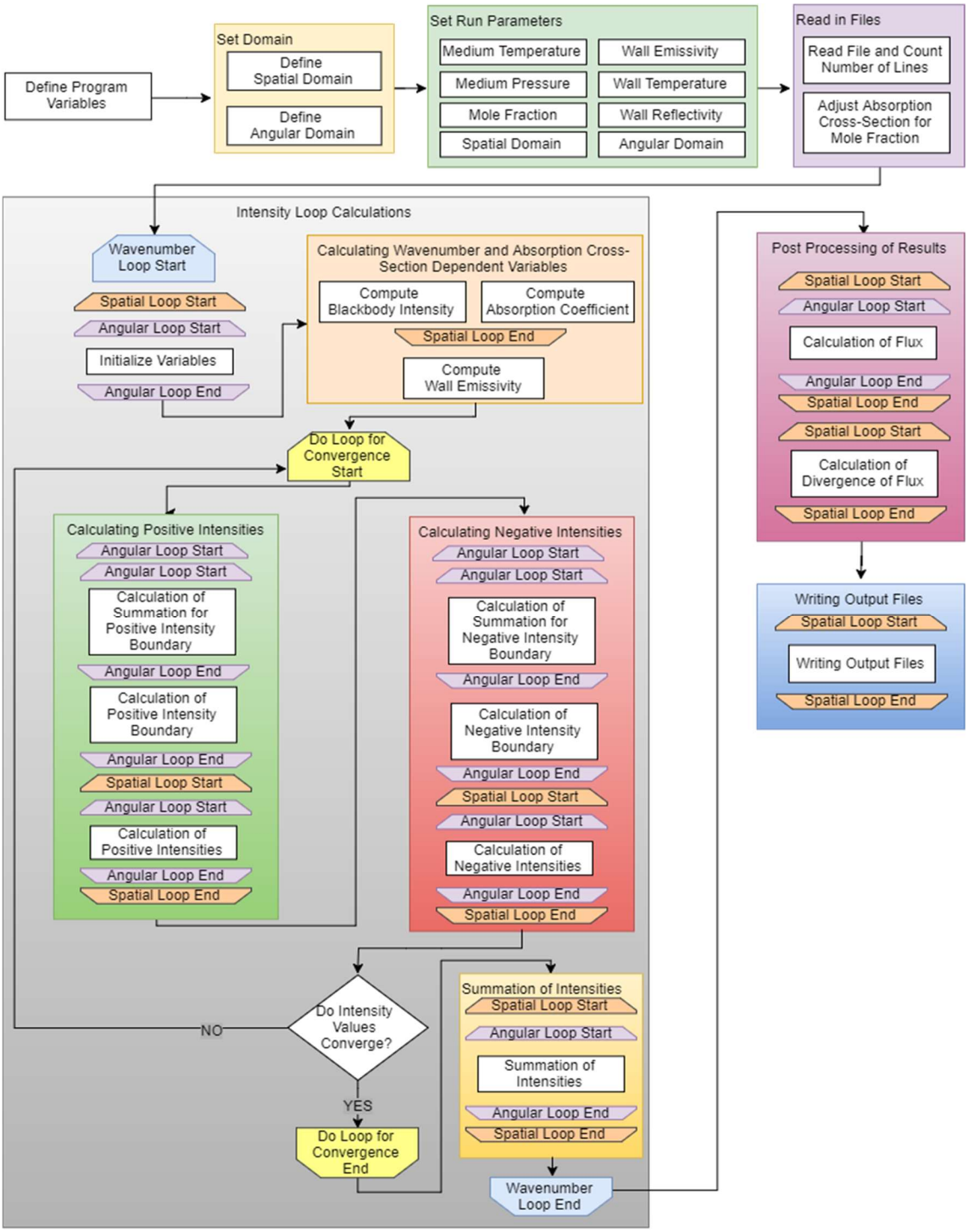

Figure 3.4 General RTE code schematic.

3.4 General Boundary Condition Formulation

According to Modest [8], the general boundary for diffusely emitting and reflecting opaque surfaces can be formulated as:

$$I(\mathbf{r},\hat{\mathbf{s}}) = \varepsilon(\mathbf{r})I_b(\mathbf{r}) + \frac{\rho(\mathbf{r})}{\pi}\int_{\hat{\mathbf{n}}\cdot\hat{\mathbf{s}}<0} I(\mathbf{r},\hat{\mathbf{s}}')|\hat{\mathbf{n}}\cdot\hat{\mathbf{s}}'|d\Omega' \quad , \tag{3.4}$$

where $\mathbf{r}$ is the point on a surface, $\hat{\mathbf{s}}$ is the direction, $\hat{\mathbf{n}}$ is the local outward surface normal, $\hat{\mathbf{n}}\cdot\hat{\mathbf{s}}' = cos\theta'$ is the cosine of the angle between any incoming direction $\hat{\mathbf{s}}'$ and the surface normal, $I(\mathbf{r},\hat{\mathbf{s}})$ is the intensity leaving the surface, $\varepsilon(\mathbf{r})$ is the emissivity of the wall surface, $I_b(\mathbf{r})$ is the blackbody intensity of the wall surface, $\rho(\mathbf{r})$ is the reflectivity of the wall surface (also can be defined as 1- ε), n is the unit normal vector at the boundary location, and Ω' is the incoming direction of radiation.

The first term, $\varepsilon(\mathbf{r})I_b(\mathbf{r})$, describes the properties of the wall surface. The second term, $\frac{\rho(\mathbf{r})}{\pi}\int_{\hat{\mathbf{n}}\cdot\hat{\mathbf{s}}<0} I(\mathbf{r},\hat{\mathbf{s}}')|\hat{\mathbf{n}}\cdot\hat{\mathbf{s}}'|d\Omega'$, accounts for the contributions to the outgoing intensity due to the reflection from incoming radiation. Together, $\varepsilon(\mathbf{r})I_b(\mathbf{r}) + \frac{\rho(\mathbf{r})}{\pi}\int_{\hat{\mathbf{n}}\cdot\hat{\mathbf{s}}<0} I(\mathbf{r},\hat{\mathbf{s}}')|\hat{\mathbf{n}}\cdot\hat{\mathbf{s}}'|d\Omega'$ accounts for the contributions to the outgoing intensity due to emission from the surface and reflection from the outgoing intensity.

3.5 Exact Solution in a 1-D Domain

This section and the following exact analytical solutions discussed is analogous to Section 1.5 in the Chapter 1, in which the solution was also discussed. The aforementioned boundary conditions in the previous section can be used with the exact solutions. According to Modest [8], an analytical or exact method can be developed for non-gray media. Neglecting scattering, the RTE is

$$\frac{dI_\eta}{ds} = \kappa_\eta I_{b\eta} - \kappa_\eta I_\eta \quad , \tag{3.5}$$

where $I_{b\eta}$ is the spectral blackbody intensity, κ_η is the spectral absorption coefficient, I_η is the spectral intensity, and s is location of intensity.

Re-arranging the previous equation by moving the absorption term to the left side results in

$$\frac{dI_\eta}{ds} + \kappa_\eta I_\eta = \kappa_\eta I_{b\eta} \quad . \tag{3.6}$$

Note that κ_η can vary with s as κ_η is a function of spatial location. Multiplying on both sides with $e^{\left(\int_0^s \kappa_\eta ds\right)}$ provides

$$e^{\left(\int_0^s \kappa_\eta ds\right)}\left[\frac{dI_\eta}{ds} + \kappa_\eta I_\eta\right] = e^{\left(\int_0^s \kappa_\eta ds\right)}\left(\kappa_\eta I_{b\eta}\right) \quad . \tag{3.7}$$

Using the product rule,

$$\frac{d}{ds}\left[e^{\left(\int_0^s \kappa_\eta ds\right)} I_\eta\right] = e^{\left(\int_0^s \kappa_\eta ds\right)}\left(\kappa_\eta I_{b\eta}\right) \quad , \tag{3.8}$$

where integrating from 0 to s gives

$$e^{\left(\int_0^s \kappa_\eta ds\right)} I_\eta(s) - I_\eta(0) = \int_0^s e^{\left(\int_0^{s'} \kappa_\eta ds''\right)}\left(\kappa_\eta I_{b\eta}\right) ds' \tag{3.9}$$

$$I_\eta(s) = e^{\left(-\int_0^s \kappa_\eta ds\right)} I_\eta(0) + \frac{\int_0^s e^{\left(\int_0^{s'} \kappa_\eta ds''\right)} (\kappa_\eta I_{b\eta}) ds'}{e^{\left(\int_0^s \kappa_\eta ds\right)}} \quad , \tag{3.10}$$

simplifying further to include the z notation,

$$I_{\eta,positive}(z,\theta) = e^{\left(-\frac{\tau_{\eta,z}}{cos\theta}\right)} I_\eta(0,\theta) + \int_0^z e^{\left(-\frac{\left(\tau_{\eta,z} - \tau'_{\eta,z'}\right)}{cos\theta}\right)}\left(\kappa_\eta I_{b\eta}\right) dz' \tag{3.11}$$

where

$$\tau_{\eta,z} = \int_0^z \kappa_\eta dz = \kappa_\eta * z \tag{3.12}$$

$$\tau'_{\eta,z'} = \int_0^{z'} \kappa_\eta dz'' \quad . \tag{3.13}$$

Equation (3.11) is the formulation for the bottom wall or positive intensities. $I_{positive}(z,\theta)$ is the intensity at positive wall (also considered the bottom wall), $I_{b\eta}$ is the spectral blackbody intensity, κ_η is the spectral absorption coefficient, I_η is the intensity, and z is the location of intensity, calculated as $x_i * dx$.

The top wall, or negative intensities, can be calculated as

$$I_{\eta,negative}(z,\theta) = e^{\left(-\frac{\tau_{\eta,z}}{cos\theta}\right)} I_\eta(L,\theta) + \int_L^z e^{\left(-\frac{\left(\tau_{\eta,z}-\tau'_{\eta,z'}\right)}{cos\theta}\right)} \left(\kappa_\eta I_{b\eta}\right) dz' \quad , \tag{3.14}$$

where

$$\tau_{\eta,z} = \int_L^z \kappa_\eta dz = \kappa_\eta (z-L) \tag{3.15}$$

$$\tau'_{\eta,z'} = \int_L^{z'} \kappa_\eta dz'' \tag{3.16}$$

with L as the wall location of intensity is calculated as number of nodes $x_i * dx$.

3.5.1 Exact Method – Homogeneous, Isothermal Cases

For an isothermal, homogenous medium in a 1-D domain, such as Cases 1a, 1b, 2a, and 2b in Chapter 1, an exact analytical solution can be developed. Recall the general exact analytical solution for 1-D:

$$I_{\eta,positive}(z,\theta) = e^{\left(-\frac{\tau_{\eta,z}}{cos\theta}\right)} I_\eta(0,\theta) + \frac{1}{cos\theta} \int_0^z e^{\left(-\frac{\left(\tau_{\eta,z}-\tau'_{\eta,z'}\right)}{cos\theta}\right)} \kappa_\eta I_{b\eta} dz' \tag{3.17}$$

with

$$\tau_{\eta,z} = \int_0^z \kappa_\eta dz = \kappa_\eta * z \tag{3.18}$$

$$\tau'_{\eta,z'} = \int_0^{z'} \kappa_\eta dz'' \quad . \tag{3.19}$$

Then (3.17) becomes

$$I_{\eta,positive}(z,\theta) = e^{\left(-\frac{1}{cos\theta}\int_0^z \kappa_\eta dz\right)} I_\eta(0,\theta) + \frac{1}{cos\theta}\int_0^z e^{\left(-\frac{\left(\int_0^z \kappa_\eta dz - \tau'_{\eta,z'}\right)}{cos\theta}\right)} \kappa_\eta I_{b\eta} dz' \ , \quad (3.20)$$

which further simplifies to

$$I_{\eta,positive}(z,\theta) = e^{\left(-\frac{\kappa_\eta * z}{cos\theta}\right)} I_\eta(0,\theta) + \frac{\kappa_\eta I_{b\eta}}{cos\theta} e^{\left(-\frac{1}{cos\theta}\int_0^z \kappa_\eta dz\right)} \int_0^z e^{\left(\frac{\left(\tau'_{\eta,z'}\right)}{cos\theta}\right)} dz' \quad (3.21)$$

$$I_{\eta,positive}(z,\theta) = e^{\left(-\frac{\kappa_\eta * z}{cos\theta}\right)} I_\eta(0,\theta) + \frac{\kappa_\eta I_{b\eta}}{cos\theta} e^{\left(-\frac{\kappa_\eta * z}{cos\theta}\right)} \int_0^z e^{\left(\frac{\left(\tau'_{\eta,z'}\right)}{cos\theta}\right)} dz' \quad (3.22)$$

$$I_{\eta,positive}(z,\theta) = e^{\left(-\frac{\kappa_\eta * z}{cos\theta}\right)} I_\eta(0,\theta) + \frac{\kappa_\eta I_{b\eta}}{cos\theta} e^{\left(-\frac{\kappa_\eta * z}{cos\theta}\right)} \left[\frac{e^{\left(\frac{\kappa_\eta * z}{cos\theta}\right)}}{\frac{\kappa_\eta}{cos\theta}}\right]_0^z \quad (3.23)$$

$$I_{\eta,positive}(z,\theta) = e^{\left(-\frac{\kappa_\eta * z}{cos\theta}\right)} I_\eta(0,\theta) + I_{b\eta} e^{\left(-\frac{\kappa_\eta * z}{cos\theta}\right)} \left(e^{\left(\frac{\kappa_\eta * z}{cos\theta}\right)} - e^{\left(\frac{\kappa_\eta * 0}{cos\theta}\right)}\right) \quad (3.24)$$

$$I_{\eta,positive}(z,\theta) = e^{\left(-\frac{\kappa_\eta * z}{cos\theta}\right)} I_\eta(0,\theta) + I_{b\eta}\left[1 - e^{\left(-\frac{\kappa_\eta * z}{cos\theta}\right)}\right] \ . \quad (3.25)$$

Additionally, for negative intensities, or from the top wall,

$$I_{\eta,negative}(z,\theta) = e^{\left(-\frac{\tau_{\eta,z}}{cos\theta}\right)} I_\eta(L,\theta) + \frac{1}{cos\theta}\int_L^z e^{\left(-\frac{\left(\tau_{\eta,z} - \tau'_{\eta,z'}\right)}{cos\theta}\right)} \kappa_\eta I_{b\eta} dz' \quad (3.26)$$

$$\tau_{\eta,z} = \int_L^z \kappa_\eta dz = \kappa_\eta (z - L) \quad (3.27)$$

$$\tau'_{\eta,z'} = \int_L^{z'} \kappa_\eta dz'' = \kappa_\eta (z' - L) \quad (3.28)$$

which becomes

$$I_{\eta,negative}(z,\theta) = e^{\left(-\frac{1}{cos\theta}\int_L^z \kappa_\eta dz\right)} I_\eta(L,\theta) + \frac{1}{cos\theta}\int_L^z e^{\left(-\frac{\left(\int_L^z \kappa_\eta dz - \tau'_{\eta,z'}\right)}{cos\theta}\right)} \kappa_\eta I_{b\eta} dz' \quad (3.29)$$

$$I_{\eta,negative}(z,\theta) = e^{\left(-\frac{\kappa_\eta (z-L)}{cos\theta}\right)} I_\eta(L,\theta) + \frac{\kappa_\eta I_{b\eta}}{cos\theta} e^{\left(-\frac{\kappa_\eta (z-L)}{cos\theta}\right)} \int_L^z e^{\left(\frac{\left(\tau'_{\eta,z'}\right)}{cos\theta}\right)} dz' \quad (3.30)$$

$$I_{\eta,negative}(z,\theta) = e^{\left(-\frac{\kappa_\eta(z-L)}{cos\theta}\right)} I_\eta(L,\theta) + \frac{\kappa_\eta I_{b\eta}}{cos\theta} e^{\left(-\frac{\kappa_\eta(z-L)}{cos\theta}\right)} \left[\frac{e^{\left(\frac{\kappa_\eta * (z'-L)}{cos\theta}\right)}}{\frac{\kappa_\eta}{cos\theta}} \right]_L^z \quad (3.31)$$

$$I_{\eta,negative}(z,\theta) = e^{\left(-\frac{\kappa_\eta(z-L)}{cos\theta}\right)} I_\eta(L,\theta) + I_{b\eta} e^{\left(-\frac{\kappa_\eta(z-L)}{cos\theta}\right)} \left(e^{\left(\frac{\kappa_\eta(z-L)}{cos\theta}\right)} - e^{\left(\frac{\kappa_\eta(L-L)}{cos\theta}\right)} \right) \quad (3.32)$$

$$I_{\eta,negative}(z,\theta) = e^{\left(-\frac{\kappa_\eta(z-L)}{cos\theta}\right)} I_\eta(L,\theta) + I_{b\eta} e^{\left(-\frac{\kappa_\eta(z-L)}{cos\theta}\right)} \left(e^{\left(\frac{\kappa_\eta(z-L)}{cos\theta}\right)} - 1 \right) \quad (3.33)$$

$$I_{\eta,negative}(z,\theta) = e^{\left(-\frac{\kappa_\eta(z-L)}{cos\theta}\right)} I_\eta(L,\theta) + I_{b\eta} \left(1 - e^{\left(-\frac{\kappa_\eta(z-L)}{cos\theta}\right)} \right) \quad . \quad (3.34)$$

3.5.2 Exact Method – Inhomogeneous Functional Varying Cases

For an inhomogeneous functional varying case in a 1-D domain, such as Case 3 in the Chapter 1, an exact analytical solution can be developed. Note that this can only be performed for specific cases, such as CO_2 and not H_2O due to the nature of the LBL H_2O. Recall the general exact analytical solution for 1-D:

$$I_{\eta,positive}(z,\theta) = e^{\left(-\frac{\tau_{\eta,z}}{cos\theta}\right)} I_\eta(0,\theta) + \frac{1}{cos\theta} \int_0^z e^{\left(-\frac{\left(\tau_{\eta,z} - \tau'_{\eta,z'}\right)}{cos\theta} \right)} \kappa_\eta I_{b\eta} dz' \quad . \quad (3.35)$$

For Case 3 in the Chapter 1, the mole fraction profile is $f(z) = 4\left(1 - \frac{z}{L}\right)z$. Recall that the absorption coefficient is dependent on mole fraction, so that $\kappa_\eta = \kappa_{\eta 1} * f(z)$, where κ_η is the absorption coefficient with the mole fraction function and $\kappa_{\eta 1}$ is the local absorption coefficient without the mole fraction function.

If

$$\tau_{\eta,z} = \int_0^z \kappa_\eta dz = \int_0^z \kappa_{\eta 1} * f(z) dz = \int_0^z \kappa_{\eta 1} * f(z) dz \; =$$

$$\kappa_{\eta 1}\int_0^z 4\left(1-\frac{z}{L}\right)zdz = 4*\kappa_{\eta 1}\int_0^z\left(z-\frac{z^2}{L}\right)dz =$$

$$4*\kappa_{\eta 1}\left[\frac{z^2}{2}-\frac{z^3}{3L}\right]_0^z = \kappa_{\eta 1}\left[2z^2-\frac{4z^3}{3L}\right]_0^z = \kappa_{\eta 1}\left(2z^2-\frac{4z^3}{3L}\right) \quad (3.36)$$

with

$$\tau'_{\eta,z'} = \kappa_{\eta 1}\left(2z'^2-\frac{4z'^3}{3L}\right) \ , \quad (3.37)$$

then (3.35) becomes

$$I_{\eta,positive}(z,\theta) = e^{\left(-\frac{\kappa_{\eta 1}\left(2z^2-\frac{4z^3}{3L}\right)}{cos\theta}\right)}I_\eta(0,\theta)\ \frac{\kappa_{\eta 1}I_{b\eta}}{cos\theta}e^{\left(-\frac{\kappa_{\eta 1}\left(2z^2-\frac{4z^3}{3L}\right)}{cos\theta}\right)}\int_0^z e^{\left(\frac{\left(\tau'_{\eta,z'}\right)}{cos\theta}\right)}f(z)dz'. \quad (3.38)$$

This further simplifies to

$$I_{\eta,positive}(z,\theta) = e^{\left(-\frac{\kappa_{\eta 1}\left(2z^2-\frac{4z^3}{3L}\right)}{cos\theta}\right)}I_\eta(0,\theta) + \frac{\kappa_{\eta 1}I_{b\eta}}{cos\theta}e^{\left(-\frac{\kappa_{\eta 1}\left(2z^2-\frac{4z^3}{3L}\right)}{cos\theta}\right)}\int_0^z e^{\left(\frac{\left(\kappa_{\eta 1}\left(2z'^2-\frac{4z'^3}{3L}\right)\right)}{cos\theta}\right)}4\left(1-\frac{z'}{L}\right)z'\,dz' \ . \quad (3.39)$$

The integral in the previous equation analytically by variable substitution can be solved. Let $\xi = 2z^2-\frac{4z^3}{3L}$, then $d\xi = \left(4z-\frac{12z^2}{3L}\right)dz$. Simplifying further provides $d\xi = 4\left(1-\frac{z}{L}\right)z\,dz$.

Then,

$$I_{\eta,positive}(z,\theta) = e^{\left(-\frac{\kappa_{\eta 1}\left(2z^2-\frac{4z^3}{3L}\right)}{cos\theta}\right)} I_\eta(0,\theta) + \frac{\kappa_{\eta 1} I_{b\eta}}{cos\theta} e^{\left(-\frac{\kappa_{\eta 1}\left(2z^2-\frac{4z^3}{3L}\right)}{cos\theta}\right)} \int_0^z e^{\left(\frac{\kappa_{\eta 1}\xi}{cos\theta}\right)} d\xi \tag{3.40}$$

$$I_{\eta,positive}(z,\theta) = e^{\left(-\frac{\kappa_{\eta 1}\left(2z^2-\frac{4z^3}{3L}\right)}{cos\theta}\right)} I_\eta(0,\theta) + \frac{\kappa_{\eta 1} I_{b\eta}}{cos\theta} e^{\left(-\frac{\kappa_{\eta 1}\left(2z^2-\frac{4z^3}{3L}\right)}{cos\theta}\right)} \left[\frac{cos\theta}{\kappa_{\eta 1}} e^{\left(\frac{\kappa_{\eta 1}\xi}{cos\theta}\right)}\right] \tag{3.41}$$

$$I_{\eta,positive}(z,\theta) = e^{\left(-\frac{\kappa_{\eta 1}\left(2z^2-\frac{4z^3}{3L}\right)}{cos\theta}\right)} I_\eta(0,\theta) + \frac{\kappa_{\eta 1} I_{b\eta}}{cos\theta} e^{\left(-\frac{\kappa_{\eta 1}\left(2z^2-\frac{4z^3}{3L}\right)}{cos\theta}\right)} \left[\frac{cos\theta}{\kappa_{\eta 1}} e^{\left(\frac{\kappa_{\eta 1}\left(2z^2-\frac{4z^3}{3L}\right)}{cos\theta}\right)}\right]_0^z \tag{3.42}$$

$$I_{\eta,positive}(z,\theta) = e^{\left(-\frac{\kappa_{\eta 1}\left(2z^2-\frac{4z^3}{3L}\right)}{cos\theta}\right)} I_\eta(0,\theta) + \frac{\kappa_{\eta 1} I_{b\eta}}{cos\theta} e^{\left(-\frac{\kappa_{\eta 1}\left(2z^2-\frac{4z^3}{3L}\right)}{cos\theta}\right)} \frac{cos\theta}{\kappa_{\eta 1}} \left[e^{\left(\frac{\kappa_{\eta 1} 2z^2-\frac{4z^3}{3L}}{cos\theta}\right)} - 1\right] . \tag{3.43}$$

Simplifying further,

$$I_{\eta,positive}(z,\theta) = e^{\left(-\frac{\kappa_{\eta 1}\left(2z^2-\frac{4z^3}{3L}\right)}{cos\theta}\right)} I_\eta(0,\theta) + I_{b\eta}\left[1 - e^{\left(-\frac{\kappa_{\eta 1} 2z^2-\frac{4z^3}{3L}}{cos\theta}\right)}\right] . \tag{3.44}$$

For negative intensities, or from the top wall,

$$I_{\eta,negative}(z,\theta) = e^{\left(-\frac{\tau_{\eta,z}}{cos\theta}\right)} I_\eta(L,\theta) + \frac{1}{cos\theta}\int_L^z e^{\left(-\frac{\left(\tau_{\eta,z}-\tau'_{\eta,z'}\right)}{cos\theta}\right)} \kappa_\eta I_{b\eta} dz' \tag{3.45}$$

with

$$\tau_{\eta,z} = \int_L^z \kappa_\eta dz = \kappa_\eta (z-L) \tag{3.46}$$

$$\tau'_{\eta,z'} = \int_L^{z'} \kappa_\eta dz'' = \kappa_\eta (z'-L) \tag{3.47}$$

$$\tau_{\eta,z} = \int_0^z \kappa_\eta dz = \int_0^z \kappa_{\eta 1} * f(z) dz = \int_0^z \kappa_{\eta 1} * f(z) dz$$

$$= \kappa_{\eta 1} \int_0^z 4\left(1-\frac{z}{L}\right) z dz = 4 * \kappa_{\eta 1} \int_0^z \left(z - \frac{z^2}{L}\right) dz =$$

$$4 * \kappa_{\eta 1}\left[\frac{z^2}{2} - \frac{z^3}{3L}\right]_0^z = \kappa_{\eta 1}\left[2z^2 - \frac{4z^3}{3L}\right]_0^z = \kappa_{\eta 1}\left(2z^2 - \frac{4z^3}{3L}\right) \tag{3.48}$$

$$\tau'_{\eta,z'} = \kappa_{\eta 1}\left(2z'^2 - \frac{4z'^3}{3L}\right) \quad . \tag{3.49}$$

Since the variable mole fraction function is symmetric across the domain – *e.g.*,

$$I_{\eta,positive}(z) = I_{\eta,negative}(L-z) \ ,$$

the problem for the negative intensities can be simplified. Using the positive intensity equation, the negative intensity equation can be formulated as

$$I_{\eta,negative}(z,\theta) = e^{\left(-\frac{\kappa_{\eta 1}\left(2(L-z)^2 - \frac{4(L-z)^3}{3L}\right)}{cos\theta}\right)} I_\eta(L,\theta) + I_{b\eta}\left[1 - e^{\left(-\frac{\kappa_{\eta 1} 2(L-z)^2 - \frac{4(L-z)^3}{3L}}{cos\theta}\right)}\right] . \tag{3.50}$$

3.6 Discrete Ordinates Method in a 1-D Domain

As previously discussed in Chapter 1, DOM is based on discretizing the direction-vector space $\hat{\mathbf{s}}$ into a finite number of direction vectors or ordinates $\hat{\mathbf{s}}_i$, $i = 1, 2, \cdots, n$. The following method is provided by Modest [8]. Before exploring the intensity formulation, the boundary conditions will first be discussed. In DOM,

$$\int_{4\pi} I(\mathbf{x}, \hat{\mathbf{s}}')|\hat{\mathbf{n}} \cdot \hat{\mathbf{s}}'|d\Omega' \quad = \quad \sum_{i=1}^{n} \omega_i I(\mathbf{x}, \hat{\mathbf{s}}_i)|\hat{\mathbf{n}} \cdot \hat{\mathbf{s}}_i| \quad , \tag{3.51}$$

where the ω_i are the quadrature weights associated with the direction $\hat{\mathbf{s}}_i$. Then equation (3.4) can be re-written to

$$I(\mathbf{x}, \hat{\mathbf{s}}_i) = \varepsilon(\mathbf{x})I_b(\mathbf{x}) + \frac{\rho(\mathbf{x})}{\pi} \sum_{\hat{\mathbf{n}} \cdot \hat{\mathbf{s}}_j < 0} \omega_j I(\mathbf{x}, \hat{\mathbf{s}}_j)|\hat{\mathbf{n}} \cdot \hat{\mathbf{s}}_j| \quad , \qquad \hat{\mathbf{n}} \cdot \hat{\mathbf{s}}_i > 0 \tag{3.52}$$

$$I(\mathbf{x}, \hat{\mathbf{s}}_i) = \varepsilon(\mathbf{x})I_b(\mathbf{x}) + \frac{\rho(\mathbf{x})}{\pi} \sum_{\hat{\mathbf{n}} \cdot \hat{\mathbf{s}}_j < 0} \omega_j I(\mathbf{x}, \hat{\mathbf{s}}_j)|\hat{\mathbf{n}} \cdot \hat{\mathbf{s}}_j| \quad , \qquad \hat{\mathbf{n}} \cdot \hat{\mathbf{s}}_i > 0 \quad . \tag{3.53}$$

The first term, $\varepsilon(\mathbf{x})I_b(\mathbf{x})$, describes the properties of the wall surface. The second term, $\frac{\rho(\mathbf{x})}{\pi} \sum_{\hat{\mathbf{n}} \cdot \hat{\mathbf{s}}_j < 0} \omega_j I(\mathbf{x}, \hat{\mathbf{s}}_j)|\hat{\mathbf{n}} \cdot \hat{\mathbf{s}}_j|$ accounts for the contributions to the outgoing intensity due to the reflection from incoming radiation. Together, $\varepsilon(\mathbf{x})I_b(\mathbf{x}) + \frac{\rho(\mathbf{r})}{\pi} \sum_{\hat{\mathbf{n}} \cdot \hat{\mathbf{s}}_j < 0} \omega_j I(\mathbf{x}, \hat{\mathbf{s}}_j)|\hat{\mathbf{n}} \cdot \hat{\mathbf{s}}_j|$ accounts for the contributions to the outgoing intensity due to emission from the surface and reflection from the outgoing intensity.

For the intensity calculations in a 1-D domain, regardless of if the medium is isothermal, homogeneous, non-isothermal, inhomogeneous, or functionally varying, DOM can be applied in a more straightforward manner, unlike the exact analytical solution. DOM has a general formulation for nearly all variations of cases. For a general formulation of the RTE:

$$\hat{\mathbf{s}}_{\boldsymbol{i}} \cdot \nabla I(\mathbf{x}, \hat{\mathbf{s}}_i) = \kappa(\mathbf{x}) I_b(\mathbf{x}) - \kappa(\mathbf{x}) I(\mathbf{x}) + \frac{\sigma_s(\mathbf{x})}{4\pi} \sum_{\mathrm{j}=1}^{n} \omega_j I\left(\mathbf{x}, \hat{\mathbf{s}}_j\right) \phi\left(\mathbf{x}, \hat{\mathbf{s}}_j, \hat{\mathbf{s}}_i\right) \quad , \quad (3.54)$$

where $\hat{\mathbf{s}}_{\boldsymbol{i}} \cdot \nabla I(\mathbf{x}, \hat{\mathbf{s}}_i)$ is the gradient of intensity in the specified direction, $\hat{\mathbf{s}}_{\boldsymbol{i}}$, $\kappa(\mathbf{x})$ is the absorption coefficient of medium, $\sigma_s(\mathbf{x})$ is the scattering coefficient of medium, $I(\mathbf{x})$ is the intensity of medium, $I_b(\mathbf{x})$ is the blackbody intensity of medium, $\phi\left(\mathbf{x}, \hat{\mathbf{s}}_j, \hat{\mathbf{s}}_i\right)$ is the phase function from incoming direction to outgoing direction, Ω is the outgoing direction of radiation, and Ω' is the incoming direction of radiation. The term $-\kappa(\mathbf{x}) I(\mathbf{x})$ accounts for the decrease in number of photons per direction because they are absorbed and $\kappa(\mathbf{x}) I_b(\mathbf{x})$ accounts for the increase in number of photons because of thermal emission. The term $\frac{\sigma_s(\mathbf{x})}{4\pi} \sum_{\mathrm{j}=1}^{n} \omega_j I\left(\mathbf{x}, \hat{\mathbf{s}}_j\right) \phi\left(\mathbf{x}, \hat{\mathbf{s}}_j, \hat{\mathbf{s}}_i\right)$ accounts for the scattering, in which a photon propagating along a direction is redirected onto another direction. It is integrated to consider all possible directions.

In the RTE, the scattering references will be removed, since scattering does not contribute to the overall heat transfer, but rather re-directs photons. Taking out the scattering provides

$$\hat{\mathbf{s}}_{\boldsymbol{i}} \cdot \nabla I(\mathbf{x}, \hat{\mathbf{s}}_i) = \kappa(\mathbf{x}) I_b(\mathbf{x}) - \kappa(\mathbf{x}) I(\mathbf{x}) \quad . \quad (3.55)$$

Further simplifying with $\kappa = \beta$ and $\kappa I_b = S$ provides

$$\hat{\mathbf{s}}_{\boldsymbol{i}} \cdot \nabla I(\mathbf{x}, \hat{\mathbf{s}}_i) = -\beta I(\mathbf{x}) + S \quad . \quad (3.56)$$

The following formulation is the same as the 1-D formulation by Pearson [5], Chu *et al.* [3], but follows the detailed formulation provided by Modest [8] and Caliot [40]. Starting with the previous equation and taking the gradient of the intensity in the discrete direction at the position:

$$\mu \frac{\partial I}{\partial x} = -\beta I + S \quad , \quad (3.57)$$

where μ is the direction cosine. Multiply both sides of the equations by dx:

$$\mu\, \partial I = -\beta I dx + S dx \ . \tag{3.58}$$

Integrating over the control volume provides

$$|\mu|\ (A_{exit} I_{exit} - A_{enter} I_{ente}\ ) = -\beta I_p \Delta x + S\Delta x \ , \tag{3.59}$$

where $A_{exit} I_{exit}$ and $A_{enter} I_{enter}$ are the face areas and intensities of each direction. Recall this is a 1-D problem with two walls with two directions: $\mu > 0$ and $\mu < 0$, where the west wall is $\mu > 0$ and the east wall is $\mu < 0$. I_p is the intensity at the cell center point and calculations begin at the west wall. For this particular case, the previous equation becomes

$$|\mu|\ (A_e I_e - A_w I_w) = -\beta I_p \Delta x + S\Delta x \ , \tag{3.60}$$

where the intensity enters in from the west, beginning with the west boundary condition value, and moving east, where the intensity exits. The intensities at each face of the control volume can be related to the cell-center intensity by the following general relation:

$$I_p = \gamma I_{exit} + (1-\gamma) I_{enter} \ , \tag{3.61}$$

Where γ is a weighting factor relation, which is covered in a later section. Equation (3.61) states that the intensity at a point can be related to the amount of intensity entering and exiting the cell center. With this relation, an equation for the west wall, $\mu > 0$ can be formulated. Starting at the west wall and moving easterly, the intensity at the west wall is the entering intensity and the intensity at the east wall is the exiting intensity, providing

$$I_p = \gamma I_e + (1-\gamma) I_w \ . \tag{3.62}$$

Equation (3.62) can be used in equation (3.60) to solve for the intensities at I_p. Restructuring (3.62) to solve for I_e provides

$$I_e = \frac{1}{\gamma}(I_p - (1-\gamma)I_w) \quad . \tag{3.63}$$

Solving for $A_e I_e - A_w I_w$ in (3.60) gives

$$A_e I_e - A_w I_w = \frac{1}{\gamma}\{A_e I_p - I_w(A_e(1-\gamma) + \gamma A_w)\} \ , \tag{3.64}$$

Where $\big((1-\gamma)A_e + \gamma A_w\big)$ can be substituted for a variable, A_{ew}. This simplifies (3.64) to

$$A_e I_e - A_w I_w = \frac{1}{\gamma}\{A_e I_p - I_w A_{ew}\} \ . \tag{3.65}$$

Substituting (3.65) into the $A_e I_e - A_w I_w$ in (3.60) provides

$$|\mu| \ \frac{1}{\gamma}\{A_e I_p - I_w A_{ew}\} = -\beta I_p \Delta x + S\Delta x \quad , \tag{3.66}$$

And simplifying (3.66) obtains

$$\frac{|\mu| A_e I_p}{\gamma} - \frac{|\mu| I_w A_{ew}}{\gamma} = -\beta I_p \Delta x + S\Delta x \quad . \tag{3.67}$$

To solve for I_p, the I_p terms are moved to one side, giving

$$\frac{|\mu| A_e I_p}{\gamma} + \ \beta I_p \Delta x = \frac{|\mu| I_w A_{ew}}{\gamma} + S\Delta x \ , \tag{3.68}$$

and grouping terms and solving for I_p to give

$$I_p \left(\frac{|\mu| A_e}{\gamma} + \ \beta\Delta x\right) = \frac{|\mu| I_w A_{ew}}{\gamma} + S\Delta x \quad . \tag{3.69}$$

Then

$$I_p = \frac{\left({}^{|\mu| I_w A_{ew}}/_{\gamma}\right) + S\Delta x}{\left({}^{|\mu| A_e}/_{\gamma}\right) + \ \beta\Delta x} \qquad \text{for} \quad \mu > 0 \quad . \tag{3.70}$$

Equation (3.70) is the final form of the cell-center point intensity starting from the west wall and marching east. The west intensity starts at the west wall boundary condition intensity and then moves to the east boundary. After the intensities are found for each point in the domain, then the east intensities are calculated. The east intensity to west

intensity formulation can begin at equation (3.59). Starting at the east boundary, the east intensity is the entering intensity and the west intensity is the exiting intensity, providing

$$|\mu|\,(A_w I_w - A_e I_e) = -\beta I_p \Delta x + S\Delta x \quad . \tag{3.71}$$

Note that $|\mu|$ is used instead of μ. As discussed in the boundary condition section, although the notation of $\mu > 0$ and $\mu < 0$ are used, μ will always be positive. The notation of $\mu < 0$ only denotes the direction of the intensities traveling.

Recall (3.61) as

$$I_p = \gamma I_{exit} + (1-\gamma) I_{enter} \quad . \tag{3.61}$$

Noting again that the east intensity is the entering intensity and the west intensity is the exiting intensity:

$$I_p = \gamma I_w + (1-\gamma) I_e \quad . \tag{3.72}$$

Equation (3.72) can be used in equation (3.71) to solve for the intensities at I_p. Restructuring (3.72) to solve for I_w provides

$$I_w = \frac{1}{\gamma}(I_p - (1-\gamma) I_e) \quad . \tag{3.73}$$

Solving for $A_w I_w - A_e I_e$ in (3.71) gives

$$A_w I_w - A_e I_e = \frac{1}{\gamma}\{A_w I_p - I_e(A_w(1-\gamma) + \gamma A_e)\} \quad . \tag{3.74}$$

$\big((1-\gamma)A_w + \gamma A_e\big)$ can be substituted for a variable, A_{ew}, simplifying (3.74) to

$$A_w I_w - A_e I_e = \frac{1}{\gamma}\{A_w I_p - I_e A_{ew}\} \quad . \tag{3.75}$$

Substituting (3.75) into the $A_w I_w - A_e I_e$ in (3.71), providing

$$|\mu|\,\frac{1}{\gamma}\{A_w I_p - I_e A_{ew}\} = -\beta I_p \Delta x + S\Delta x \quad . \tag{3.76}$$

Simplifying further gives

$$\frac{|\mu|A_w I_p}{\gamma} - \frac{|\mu|I_e A_{ew}}{\gamma} = -\beta I_p \Delta x + S\Delta x \quad . \tag{3.77}$$

To solve for I_p, the I_p terms are moved to one side, providing

$$\frac{|\mu|A_w I_p}{\gamma} + \beta I_p \Delta x = \frac{|\mu|I_e A_{ew}}{\gamma} + S\Delta x \quad . \tag{3.78}$$

Grouping terms in (3.75) and solving for I_p results in

$$I_p \left(\frac{|\mu|A_w}{\gamma} + \beta\Delta x\right) = \frac{|\mu|I_e A_{ew}}{\gamma} + S\Delta x \quad , \tag{3.79}$$

finally resulting in

$$I_p = \frac{\left({}^{|\mu|I_e A_{ew}}/_{\gamma}\right) + S\Delta x}{\left({}^{|\mu|A_w}/_{\gamma}\right) + \beta\Delta x} \qquad \text{for} \quad \mu < 0 \quad . \tag{3.80}$$

3.7 Control-Angle Discrete Ordinates Method

One of the more popular solution methods is CA-DOM, which is a combination of the basic concepts of the finite volume and discrete ordinates methods. In CA-DOM, the radiation directional space is discretized into solid angles, with each solid angle enveloping a discrete direction. Analogous to the finite volume approach, the RTE is then integrated over a control volume and a control angle, which is the direction-space counterpart to the control volume. The (control) angle integrals of directional divergence terms are converted into surface integrals, *i.e.,* facial flux terms, which are obtained just as in the conventional finite volume approach. The integrals over the control angle are evaluated analytically, eliminating the quadrature errors found in the conventional DOM approach. Accuracy of the control angle integration is, however, determined by the number of control angles used to discretize the directional space. The steady spectral radiative transfer equation for an emitting, absorbing and scattering non-gray gas can be written as:

$$\frac{dI^{\eta}(\mathbf{r},\hat{\mathbf{s}})}{ds} = -\left(K_s^{\eta} + K_a^{\eta}\right)I^{\eta}(\mathbf{r},\hat{\mathbf{s}}) + K_a^{\eta} I_b^{\eta}(\mathbf{r}) + \frac{K_s^{\eta}}{4\pi}\int_{4\pi} I^{\eta}(\mathbf{r},\hat{\mathbf{s}}')\, p(\hat{\mathbf{s}}' \rightarrow \hat{\mathbf{s}};\mathbf{r}) d\Omega' \quad , \qquad (3.81)$$

where I^{η} is the spectral intensity along a line-of-sight vector $\hat{\mathbf{s}}$, $\mathbf{r}$ is the spatial location at which the radiative intensity is to be computed, p is the in-scattering phase function, Ω' is the solid angle enveloping the direction $\hat{\mathbf{s}}'$, and I_b^{η} is the Planck's function. The spectral scattering and absorption coefficients are K_s^{η} and K_a^{η} respectively. Equation (3.81) can be re-written as

$$\hat{\mathbf{s}} \bullet \nabla_r I^{\eta} = -\left(K_s^{\eta} + K_a^{\eta}\right)I^{\eta}(\hat{\mathbf{s}},\Omega) + K_a^{\eta} I_b^{\eta} + \frac{K_s^{\eta}}{4\pi}\int_{4\pi} I^{\eta}(\mathbf{r},\hat{\mathbf{s}}')p(\hat{\mathbf{s}}' \rightarrow \hat{\mathbf{s}})d\Omega' \quad , \qquad (3.82)$$

where ∇_r is the spatial gradient term. Since the radiative direction $\mathbf{s}$ does not depend upon the spatial location $\mathbf{r}$, the RTE can be written as

$$\nabla \bullet (\hat{\mathbf{s}} I^{\eta}) = -\left(K_s^{\eta} + K_a^{\eta}\right)I^{\eta}(\hat{\mathbf{s}},\Omega) + K_a^{\eta} I_b^{\eta} + \frac{K_s^{\eta}}{4\pi}\int_{4\pi} I^{\eta}(\mathbf{r},\hat{\mathbf{s}}')p(\hat{\mathbf{s}}' \rightarrow \hat{\mathbf{s}})d\Omega' \quad . \qquad (3.83)$$

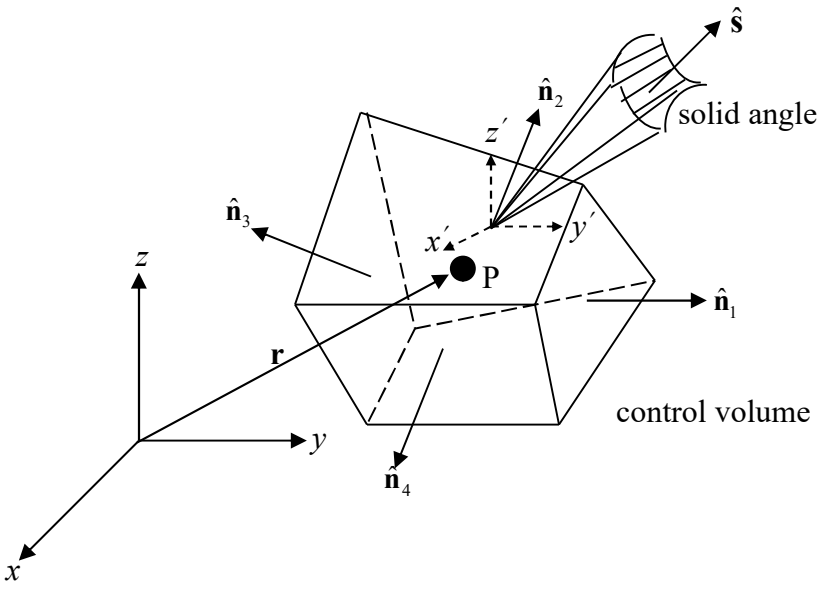

Figure 3.5 Schematic of a control volume and a control angle used in CA-DOM.

The first step in CA-DOM is to subdivide the physical computational domain into control volumes and the radiation directional space into control angles, which can be seen

in Figure 3.5. Each control angle is a solid angle that envelops the direction vector or the discrete ordinate $\hat{s}$. The control volumes could be arbitrary polyhedra, although simpler tetrahedra, hexahedra, wedges, pyramids, *etc.*, are more common. Each control volume has a cell center, P, given by the position vector **r** at which all dependent variables are stored. The control volume has a number of faces whose outward normals are represented as $\hat{\mathbf{n}}_i$, i being the face index. The control angle is essentially a differential solid angle, obtained by taking infinitesimal steps $d\theta$ and $d\phi$ around polar and azimuthal angles θ and ϕ, respectively. This can be seen in Figure 3.6.

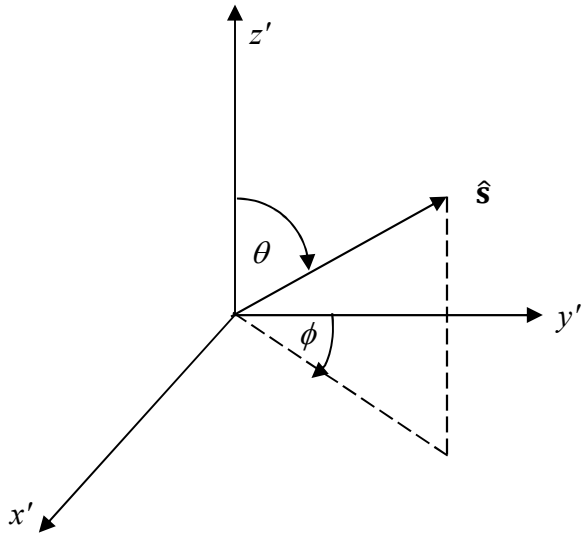

Figure 3.6 Schematic of the radiation direction vector, $\hat{\mathbf{s}}$, with the polar and azimuthal angles.

The control angles are obtained by dividing the directional space (4π steradians) into solid angles as shown above. Let $I_P^{m\eta}$ represent the radiation intensity (units of power per unit area per steradian per unit wavelength) at the cell center P of the control volume, in the direction $\hat{s}$ represented by the m^{th} solid angle Ω_m, and at wavelength η. The subscript "m" refers to the discretization index of the solid angle space. Upon

integrating equation (3.83) over the control volume and the control angle (m), this provides

$$\int_{\Omega_m}\int_V \nabla \bullet (\hat{\mathbf{s}} I^\eta) dV d\Omega = -\int_{\Omega_m}\int_V \left(K_s^\eta + K_a^\eta\right) I^\eta dV d\Omega +$$

$$\int_{\Omega_m}\int_V \left[K_a^\eta I_b^\eta + \frac{K_s^\eta}{4\pi}\int_{4\pi} I^\eta\,(\hat{\mathbf{s}}, \Omega')p(\hat{\mathbf{s}}' \rightarrow \hat{\mathbf{s}}) d\Omega'\right] dV d\Omega \quad . \tag{3.84}$$

Using the divergence theorem, the volume integral on the left hand side (LHS) of the above equation can converted into a surface integral over the control volume surface A, providing

$$\int_{\Omega_m}\int_A I^\eta (\hat{\mathbf{s}} \bullet \hat{n}) dA d\Omega = -\int_{\Omega_m}\int_V \left(K_s^\eta + K_a^\eta\right) I^\eta dV d\Omega +$$

$$\int_{\Omega_m}\int_V \left[K_a^\eta I_b^\eta + \frac{K_s^\eta}{4\pi}\int_{4\pi} I^\eta\,(\hat{\mathbf{s}}, \Omega')p(\hat{\mathbf{s}}' \rightarrow \hat{\mathbf{s}}) d\Omega'\right] dV d\Omega \quad . \tag{3.85}$$

The LHS integral over the control volume surface is next broken down into integrals over the faces A_{Pi} of the control volume V_P. Using the standard finite volume methodology, the surface integrals are written simply as a summation over the control volume faces, while the volume integrals are reduced to a product of the integrand value over the control volume and V_P. The control volume and facial radiant intensities are assumed to be constant. This provides

$$\sum_{A_{Pi}} I_i^{m\eta} A_{Pi} s_\Omega \bullet \hat{n}_{Pi} = \left[-\left(K_{s,P}^\eta + K_{a,P}^\eta\right) I_P^{m\eta} + K_{a,P}^\eta I_{b,P}^\eta\right] V_P \Omega_m$$

$$+ \frac{K_{s,P}^\eta}{4\pi} V_P \Omega_m \sum_{m'} I_P^{m'\eta} \bar{p}(m, m') \quad , \tag{3.86}$$

where

$$\Omega_m = \int_{\Omega_m} d\Omega = \int_{\Delta\theta_m}\int_{\Delta\phi_m} \sin\theta \, d\theta d\phi$$

$$\mathbf{s}_\Omega = \int_{\Omega_m} s d\Omega$$

$$\bar{p}(m,m') = \int_{\Omega_m} p(m,m') d\Omega = \int_{\Delta\theta_m}\int_{\Delta\phi_m} p(m,m') \sin\theta \, d\theta d\phi \quad .$$

In the above equations, subscript *i* denotes the value at the face *i* of the control volume *P*, subscript *P* denotes the value at the grid point *P* of the control volume and the scattering and absorption coefficients are functions of the spatial location *P* (because of anisotropy), and of wavenumber. The integral $\int_{\Omega_m} d\Omega$ represents integral over the control angle, Ω_m, of interest and the integral $\int_{4\pi} d\Omega_{m'}$ represents integration over all the other control angles that contribute to the control angle *m* through the in-scattering function, *p*. The mean direction vector, $\boldsymbol{s_\Omega}$, corresponding to a control angle, Ω_m, is obtained as follows:

$$\hat{\mathbf{s}} = \sin\theta \sin\phi \mathbf{i} + \sin\theta \cos\phi \mathbf{j} + \cos\theta \mathbf{k} \tag{3.87}$$

$$\Rightarrow \mathbf{s}_\Omega = \int_{\Omega_m} \hat{\mathbf{s}} d\Omega$$

$$= \int_{\Delta\theta_m}\int_{\Delta\phi_m} \hat{\mathbf{s}} \sin\theta \, d\theta d\phi = \sin\phi_m \sin\frac{\Delta\phi_m}{2}(\Delta\theta_m - \cos 2\theta_m \sin\Delta\theta_m)\mathbf{i}$$

$$+ \cos\phi_m \sin\tfrac{\Delta\phi_m}{2}(\Delta\theta_m - \cos 2\theta_m \sin\Delta\theta_m)\mathbf{j} + \tfrac{\Delta\phi_m}{2} \sin 2\theta_m \sin\Delta\theta_m \boldsymbol{k} \quad . \tag{3.88}$$

The discretization of the directional space is shown in Figure 3.7.

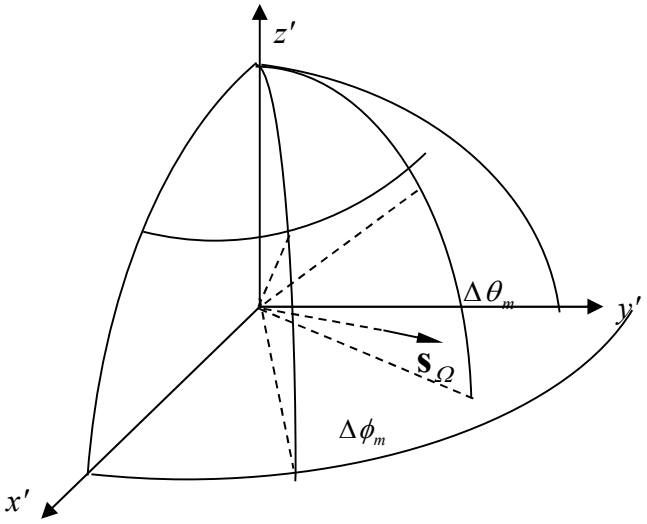

Figure 3.7 Discretization of the directional space.

The normal to the control volume faces, $\hat{n}_{Pi}$, is always oriented outward from the control volume and can be obtained from the coordinates of the face vertices.

3.7.1 Radiant Intensities at Control Volume Faces

The control volume facial intensities, $I_{Pi}^{m\eta}$, can computed in terms of the cell center values of intensities, $I_P^{m\eta}$ (including the neighboring cell centers) using various spatial differencing schemes. Among these, the step scheme (or the upwind scheme), though only of first order accuracy, provides stable non-negative intensities and is cost effective for large multi-dimensional problems. Under this scheme, the following is obtained:

$$I_i^{m\eta} = I_P^{m\eta}, \mathbf{s}_\Omega \bullet \hat{\mathbf{n}}_{Pi} > 0$$

$$I_i^{m\eta} = I_F^{m\eta}, \mathbf{s}_\Omega \bullet \hat{\mathbf{n}}_{Pi} < 0 \quad , \tag{3.89}$$

where F denotes the downstream neighbor of cell P, as shown in Figure 3.8. The above equation can be written in a compact form as

$$\mathbf{s}_\Omega \bullet \hat{\mathbf{n}}_{Pi} I_i^{m\eta} = [0, \mathbf{s}_\Omega \bullet \hat{\mathbf{n}}_{Pi}] I_P^{m\eta} - [0, -\mathbf{s}_\Omega \bullet \hat{\mathbf{n}}_{Pi}] I_F^{m\eta} \quad , \tag{3.90}$$

where [a,b] = max(a,b).

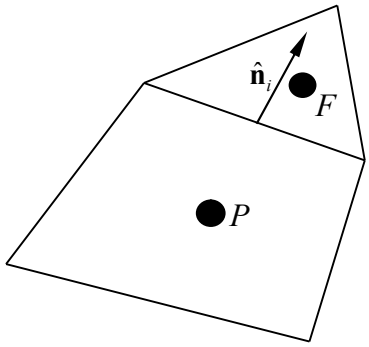

Figure 3.8 Discretization of the directional space.

3.7.2 Derivation of Discretized Linear System

The coefficients and sources in the equation for I are obtained from equation (3.86), using the face values given in equation (3.90). This represents an equation for the radiation intensity at a node P, along the discretized direction m and discretized wave band η, which is written as $I_P^{m\eta}$. For notational clarity, the m and η identifiers will be dropped, with the understanding that the equation for a given waveband and a given direction is being solved.

Expanding equation (3.86) gives the equation for the radiation intensity at node P, for direction m and wavelength η as

$$\sum_i A_{Pi}([0, s_i] I_P - [0, -s_i] I_F) = -\left(K_{s,p}^\eta + K_{a,p}^\eta\right) V_P \Omega_m I_P + S_P \quad , \tag{3.91}$$

where

$$s_i = \mathbf{s}_\Omega \bullet \hat{\mathbf{n}}_{Pi} \quad . \tag{3.92}$$

The source term in equation (3.91) is given by

$$S_P = K_{a,P}^\eta I_{b,P} V_P \Omega_m + \frac{K_{s,P}^\eta}{4\pi} V_P \Omega_m \sum_{m'} I_P^{m'} \bar{p}(m, m') \quad . \tag{3.93}$$

In equation (3.93), the term $I_P^{m'}$ represents the radiation intensity at node *P*, along direction *m′*.

Equation (3.91) represents a linear equation for the radiation intensity at node *P*, direction *m*, and wavelength η, written in terms of the of the radiation intensity at the immediate neighbors of node *P*. It may be expressed more compactly as

$$a_P I_P = \sum_{nb} a_{nb} I_{nb} + S_P \quad . \tag{3.94}$$

In equation (3.94), the subscript *nb* refers to the neighbor of node *P*. The source term is given in equation (3.93). The diagonal coefficient (a_P) and off-diagonal coefficients (a_{nb}) are given by

$$a_P = \sum_i A_{Pi}[0, s_i] + \left(K_{s,P}^{\eta} + K_{a,P}^{\eta}\right) V_P \Omega_m \tag{3.95}$$

$$a_{nb} = A_{Pi}[0, -s_i] \quad . \tag{3.96}$$

In equations (3.95) and (3.96), the index *i* refers to the face between node *P* and neighbor node *nb*. The terms in the coefficient matrix are functions of both wavelength and direction. The wavelength dependence arises because the absorptivity and scattering coefficient are dependent on η, while the directional dependence arises because s_i is a function of direction *m*.

3.8 Calculation of Heat Equation Source Term

As shown in equation (3.2), the source term in the heat equation coming from radiation is given by

$$S_h(r) = \int_0^{\infty} K_a^{\eta} \int_{4\pi} [I(\mathbf{r}, \hat{\mathbf{s}}, \eta) - I_b(\mathbf{r}, \eta)] d\Omega d\eta \quad . \tag{3.97}$$

The integral in equation (3.97) is over the total solid angle, Ω, of 4π steradians and over wavelength. $I(\mathbf{r},\mathbf{s},\eta)$ is the radiation intensity at the spatial location **r,** along the direction

s, and at wavelength η. The term $I_b(\mathbf{r},\eta)$ is the black body intensity at the local temperature.

Inside the code, this integral is performed numerically: the wavelength integral and the direction integral are discretized into discrete values of wavelength band (a) and direction (m). The numerical integral for the source term at node P is given by

$$S_h(P) = \sum_a K_a(a) \sum_m w(a,m)[I(P,a,m) - I_b(P,a)] \quad . \qquad (3.98)$$

In equation (3.98), the term *w(a,m)* is a numerical integration weighting factor for wavelength band (a) and direction (m). The term *I(P,a,m)* represents the radiation intensity at node P, for wavelength band (a) and direction (m). The weighting function is given as $w(a,m) = \Omega_m = \int_{\Omega_m} d\Omega = \int_{\Delta\theta}\int_{\Delta\phi} sin\,\theta\, d\theta d\phi$. The value of *w(a,m)* is computed for each of the control angles by analytically evaluating the above integral.

- ***A note for gray bodies in computing $S_h(P)$ from equation (3.98) above*:** For gray bodies, the summation over wavelengths drops out as there is no wavenumber dependence. The blackbody intensity $I_b(a,P)$ for a gray body simulation is simply $I_b(P) = \frac{\sigma T^4}{\pi}$.
- ***A note for non-gray bodies in computing $S_h(P)$ from equation (3.98) above*:** The blackbody intensity cannot be $I_b(a,P) = \frac{\sigma T^4}{\pi}$. Instead, for a non-gray body simulation, the fraction of blackbody intensity that lies in a band represented by a, *i.e.*, I_b^{η}, which can be calculated from $I_b^{\eta} = \frac{\frac{c_1}{\pi}}{\eta^5(exp[c_2/(\eta T)]-1)}$ must be considered.
- ***A note on solid angle integration for the blackbody intensity term (both gray and non-gray)*:** Both $I_b(P)$ (for a gray gas) and $I_b(a,P)$ (for a non-gray gas) are

independent of solid angle (*i.e.,* direction). Therefore, the integration over Ω simply reduces to $4\pi^* I_b(P)$ or $4\pi^* I_b(a,P)$ as may be the case.

3.9 Conclusion

Referring back to Equation (3.86), which is reproduced below:

$$\sum_{A_{Pi}} I_i^{m\eta} A_{Pi} \mathbf{s}_\Omega \bullet \hat{\mathbf{n}}_{Pi} = \left[-\left(K_{s,P}^{\eta} + K_{a,P}^{\eta}\right) I_P^{m\eta} + K_{a,P}^{\eta} I_{b,P}^{\eta}\right] V_P \Omega_m + \frac{K_{s,P}^{\eta}}{4\pi} V_P \Omega_m \sum_{m'} I_P^{m'\eta} \bar{p}(m,m') \quad , \tag{3.86}$$

where

$$\Omega_m = \int_{\Omega_m} d\Omega = \int_{\Delta\theta_m} \int_{\Delta\phi_m} \sin\theta \, d\theta d\phi$$

$$\mathbf{s}_\Omega = \int_{\Omega_m} s d\Omega$$

$$\bar{p}(m,m') = \int_{\Omega_m} p(m,m') d\Omega = \int_{\Delta\theta_m} \int_{\Delta\phi_m} p(m,m') \sin\theta \, d\theta d\phi \quad .$$

After obtaining $\mathbf{s}_\Omega \bullet \hat{\mathbf{n}}_{Pi}$, the facial values of the radiant intensity, I_{Pi}^m, are obtained using an upwind or step scheme as

$$I_{Pi}^m = I_P^m, \mathbf{s}_\Omega \bullet \hat{\mathbf{n}}_{Pi} > 0$$

$$= I_F^m, \mathbf{s}_\Omega \bullet \hat{\mathbf{n}}_{\boldsymbol{P}i} < 0 \quad . \tag{3.99}$$

After dividing the top equation in Equation (3.86) with Ω_m, the discretized algrebraic equation for the cell centered radiation intensity in the direction *m* can be written as

$$a_P^m I_P^m = \sum a_{nb}^m I_{nb}^m + S_P^m V_P \quad , \tag{3.100}$$

which can be solved using any convenient solver.

Assuming the physical boundary to emit and reflect radiation diffusively, the radiant intensity leaving the boundary surface at location $\mathbf{r}_w$ can be written as

$$I^{\eta}(\mathbf{r}_w, \mathbf{s}) = \varepsilon I_b^{\eta}(\mathbf{r}_w) + \frac{1-\varepsilon}{\pi} q_i^{\eta}(r_w), \ \forall \mathbf{s} \ni s \bullet n < 0 \quad . \tag{3.101}$$

Here, ε is the surface emissivity, $\mathbf{n}$ is the unit normal vector at the surface oriented outward into the medium and q_i is the incident radiative flux, which can be obtained by integrating the incoming intensities over a hemisphere on the boundary surface with

$$q_i^{\eta}(\mathbf{r}_w) = \int_{2\pi} I^{\eta}(\hat{\mathbf{s}}, \mathbf{r}) A_{Pi} \hat{\mathbf{s}} \bullet \mathbf{n} d\Omega \,, \ \forall \hat{\mathbf{s}} \ni \hat{s} \bullet n > 0 \quad . \tag{3.102}$$

Here, A_{Pi} is the the area of the boundary face of the boundary control volume. Remember that $\mathbf{s}$ is the direction vector corresponding to a given solid angle Ω and is obtained from

$$\hat{\mathbf{s}} = sin\,\theta\, sin\,\phi \mathbf{i} + sin\,\theta\, cos\,\phi \mathbf{j} + cos\,\theta\, \mathbf{k} \quad . \tag{3.103}$$

Chapter 4. Line-By-Line Absorption Coefficient Methodologies

4.1 Introduction

To understand the radiative heat transfer and the associated trends and behaviors, it is useful to understand the phenomena starting at the molecular level, line structure, and broadening mechanisms, which is beyond the scope of this study. However, references [8, 41, 42, 43, 44, 45] are detailed references to visit regarding molecular energy states, molecular structure and line structure and shape. Further, for this study, references on the LBL databases for HITRAN and HITEMP are useful to reference, specially [7], which covers the development of HITRAN and HITEMP and the composition of the databases. The remainder of the chapter will focus on the calculation and validation of the absorption coefficient values.

4.2 Calculation of the Line-by-Line Absorption Coefficient

To calculate radiative properties of interest, including absorption coefficient, several calculations from the HITRAN and HITEMP databases must be performed. Calculations performed in this section are based on the work in [5, 7, 8, 46]. The first step is taking the parameters in the HITRAN and HITEMP databases to calculate the absorption cross-section. Then, the absorption cross-section, along with the molar density, is used in the calculation of the absorption coefficient. In calculating the absorption coefficient, it is important to understand the LBL input files, the formats, and

the variables each line in the files. Table 4.1 is an example of the information contained in each LBL file.

Table 4.1. Example of HITRAN and HITEMP line-transition format [46].

Mol/ Iso	$\nu_{\eta\eta'}$	$S_{\eta\eta'}$	$R_{\eta\eta'}$	γ_{air}	γ_{self}	E"	n	δ	iv'	iv"	q'	q"	ierr	iref		
21	800.4511	3.197E-26	6.579E-05	0.0676	0.0818	2481.562	0.78	0.00000	14	6	P	37	465	2	2	1
291	800.4547	9.724E-22	1.896E-02	0.0845	0.175	369.6303	0.94	0.00000	9	1	341619	331519	0	4	4	1
291	800.4547	3.242E-22	2.107E-03	0.0845	0.175	369.6303	0.94	0.00000	9	1	341519	331419	0	4	4	1

The table contains several variables, where $\frac{Mol}{Iso}$ is the molecular number/isotope number; $\upsilon_{\eta\eta'}$ is the frequency, cm^{-1}; $S_{\eta\eta'}$ is the intensity, cm^{-1}/(molecule*cm^{-2}) at 296K, $R_{\eta\eta'}$is the weighted transition moment-squared; $\gamma_{air}$is the air-broadened half-width, cm^{-1}/atm at 296K; γ_{self} is the self-broadened half-width, cm^{-1}/atm at 296K; E'' is the lower state energy, cm^{-1}; n is the coefficient of temperature dependence of air-broadened half-width; δ is the air-broadened pressure shift of line transition, cm^{-1}/atm at 296K; iv', iv'' are the upper and lower state global quanta indexes; q', q'' are the upper and lower state local quanta indexes; $ierr$ is the accuracy indices for frequency, intensity, and air-broadened half-width; and $iref$ is the indices for table of references corresponding to frequency, intensity, and half-width [46].

In using the parameters from the LBL file, some adjustments need to be made to accommodate for the desired pressure and temperature in addition to calculating the broadening mechanisms. These calculations follow the methods used in [5]. The pressure shifted wavenumber is defined as

$$\eta_0 = \eta_{vac} + p\delta \quad . \tag{4.1}$$

The Lorentz broadening is defined as

$$\gamma_{Lj}(p,T) = p\left(\frac{T_0}{T}\right)^n \left[\gamma_{air}(1-Y_i) + \gamma_{self}(Y_i)\right] \quad . \tag{4.2}$$

The Doppler broadening is defined as

$$\gamma_{Dj}(p,T) = \frac{\eta_0}{c}\sqrt{\frac{2kT}{M_i} ln2} \quad . \tag{4.3}$$

Finally, the line intensity shifted due to temperature of interest is defined as

$$S_j(p,T) = S(T_0)\frac{Q(T_0)}{Q(T)} exp\left[\frac{hcE''}{k}\left(\frac{1}{T_0}-\frac{1}{T}\right)\right]\frac{1-exp\left[{}^{-hc\eta_0}/_{kT}\right]}{1-exp\left[{}^{-hc\eta_0}/_{kT_0}\right]} \quad . \tag{4.4}$$

Line intensity has a weak dependence upon total pressure through the line location, η_0 [5]. The line intensity corresponds to the product of the quantum mechanical probability for the transition and population difference between initial (absorption) and final (emission) states [43].

The Voigt profile, which is used in this study's absorption coefficient calculations, is then used with the Lorentz Broadening, Doppler Broadening, and shifted line intensity, which becomes

$$C_{\eta,j}(p,T,Y_i) = \frac{S_j(p,T)\gamma_{Lj}(p,T)}{\pi^{3}/_{2}} \times \int_{-\infty}^{\infty} \frac{e^{-x^2}dx}{\left[\eta_{vac}-\eta_{0,j}(p)-\left(\frac{x\gamma_{D,j}(p,T)}{\sqrt{ln2}}\right)\right]^2 + \gamma^2{}_{Lj}(p,T)} \quad , \tag{4.5}$$

where $S_j(p,T)$ is the line intensity, cm^{-1}/(molecule*cm^{-2}); $\gamma_{Lj}$is the Lorentz broadening half-width, cm^{-1}; γ_{Dj} is the Doppler broadening half-width, cm^{-1}; η_0 is the pressure shifted wavenumber, cm^{-1}; η_{vac} is the wavenumber in vacuum, cm^{-1}; x is $\nu\sqrt{{}^{M_i}/_{2kT}}$, T is the user-defined temperature, K; M_i is the mass of the molecule, kg; k is Boltzmann's constant, J/K; ν is the relative velocity of molecule; η_{vac} is the original HITRAN/HITEMP wavenumber, cm^{-1}; δ is the air-broadened pressure shift, cm^{-1}/atm; n

is the coefficient of temperature dependence; p is the user-defined pressure, atm; T_0=296K, which is the reference temperature for HITRAN/HITEMP; γ_{air} is the air-broadened half-width, cm^{-1}/atm; γ_{self} is the self-broadened half-width, cm^{-1}/atm; Y_i is the user-defined mole fraction; η_0 is the shifted wavenumber, cm^{-1}; $S(T_0)$ is the line intensity at reference temperature, cm^{-1}/(molecule*cm^{-2}); E'' is the lower state energy (probability of molecule at lower state); $\frac{Q(T_0)}{Q(T)}$ is the internal partition function, calculated and dependent on T; h is Planck's constant, Js; and c is the speed of light, m/s [5]. Once the absorption cross-section is calculated, the absorption cross-section is summed for each line with

$$C_\eta(p,T,Y_i) = \sum_{j=1}^{m} C_{\eta,j}(p,T,Y_i) \quad . \tag{4.6}$$

The absorption coefficient can be calculated as the absorption cross-section multiplied by the molar density as

$$\kappa_\eta(p,T,Y_i) = C_\eta \left(\frac{pN_A}{R_u T}\right) Y_i \quad , \tag{4.7}$$

where κ_η is the spectral absorption coefficient, cm^{-1} or m^{-1}, depending on if conversion factor is used; C_η is the absorption cross-section, cm^2/molecule; Y_i is the user-defined mole fraction; p is the user-defined pressure, atm; T is the user-defined temperature, K; N_A is Avogadro's number, molecules/mole; and R_u is the universal gas constant, cm^3atm/K mole [5].

The schematic below details the flow of calculating the absorption cross-section, along with a LBL-based model absorption coefficient.

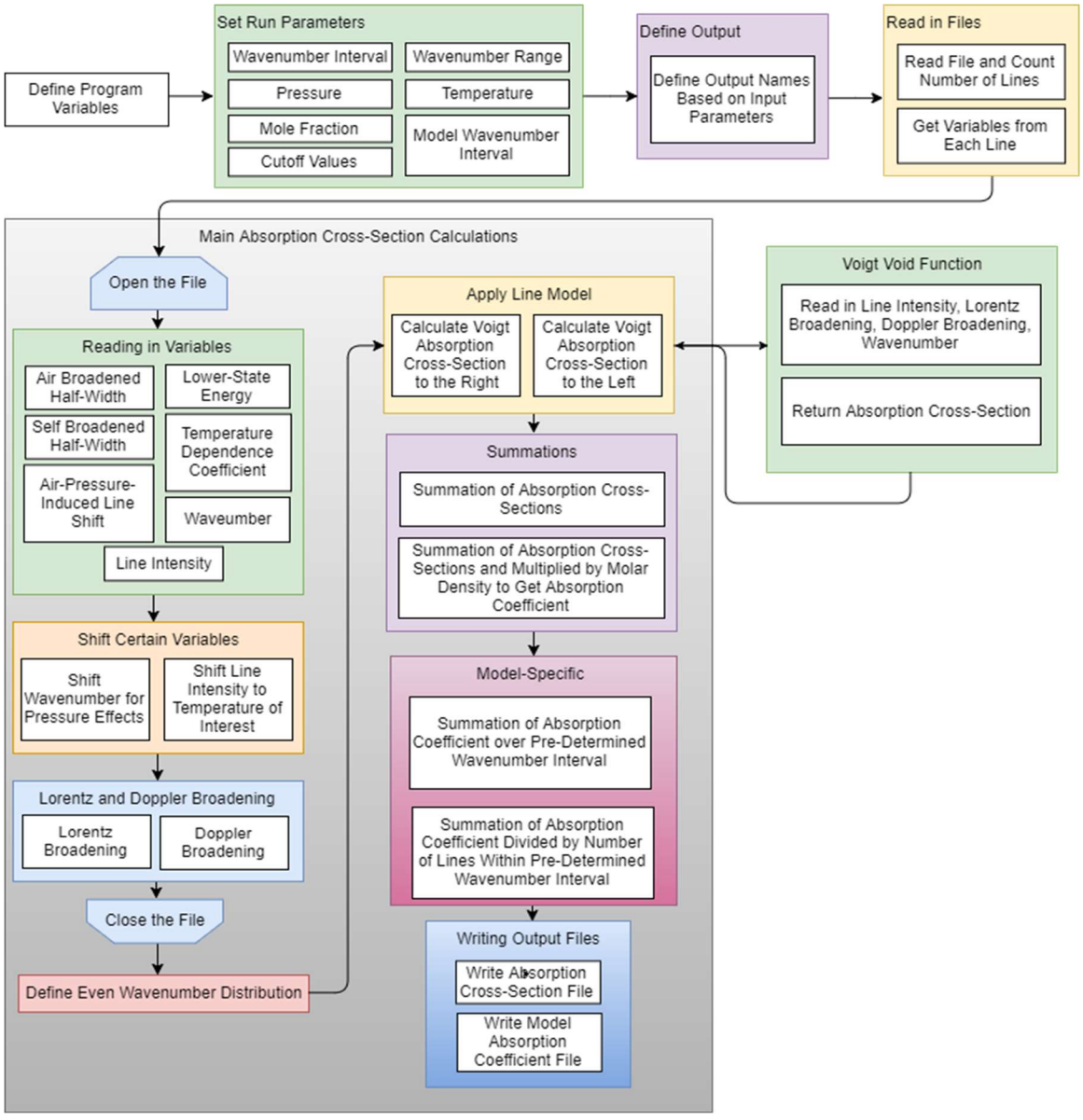

Figure 4.1 Schematic on calculating the absorption cross-section from LBL databases.

4.3 Validation of Line-by-Line Absorption Coefficients

To ensure the calculations for the absorption coefficient are correct, it is important to ensure the absorption cross-section values are correct, such as the study performed by [5]. Figure 4.2 presents a comparison of the H_2O absorption cross-section spectra measured in Ptashnik *et al.*'s [32] experiments with the corresponding LBL cross-section spectra calculated from HITEMP 2010 in the current study. Specifically, Figure 4.2 (a)

compares the experimental and LBL spectra at the temperature $T = 289$ K, total pressure $p = 1$ atm., and H_2O mole fraction of unity, while Figure 4.2 (b) presents the two spectra at a slightly higher temperature $T = 318$ K (with p and H_2O mole fraction remaining the same). It is observed that the bands and band centers of the measured and LBL spectra are in reasonable agreement. Additionally, close to the band peaks, the experimental spectra suffer from a poor resolution of spectral lines, whereas the LBL spectra demonstrate the advantage of HITEMP in achieving extremely fine spectral resolution.

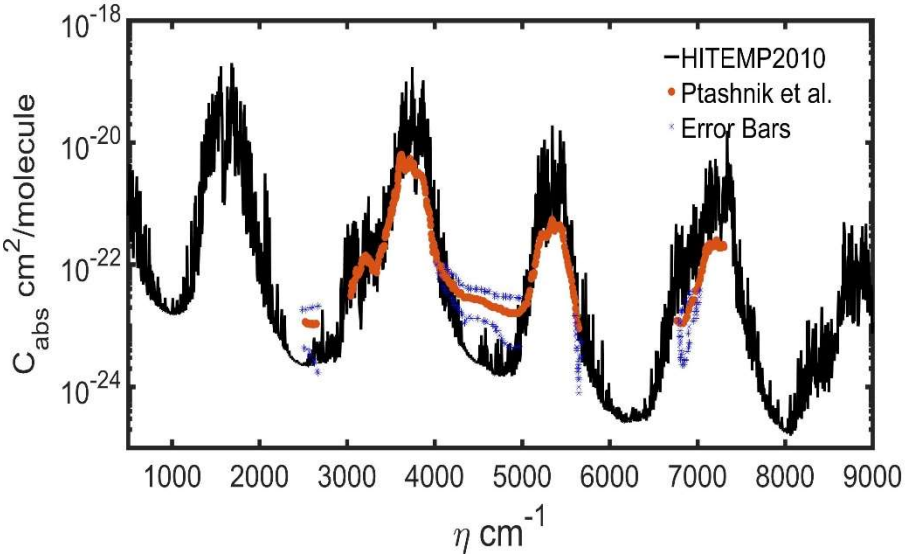

(a)

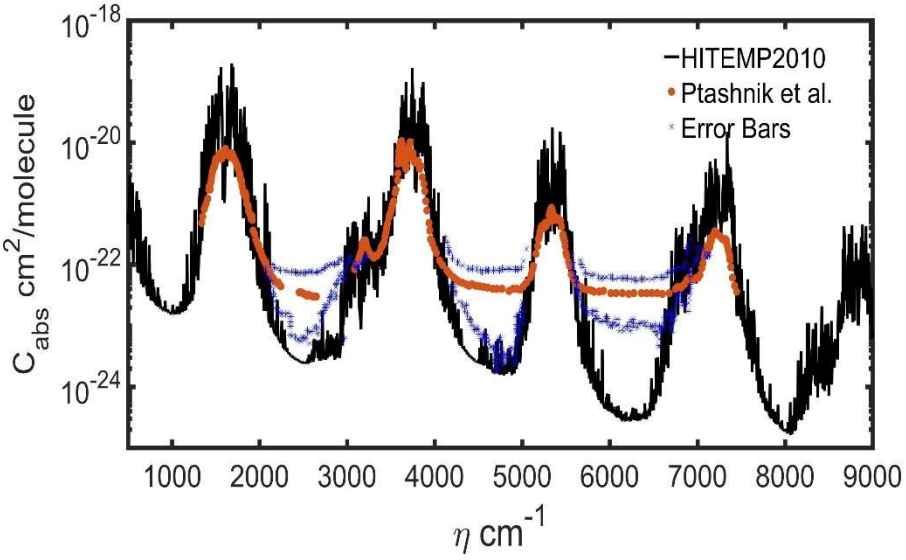

(b)

Figure 4.2 Comparison of experimental [32] and LBL absorption cross-section spectra of H_2O. (a) $T = 289$ K, and (b) $T = 318$ K. The purple data points denote the upper and lower bounds of the error bars in the Ptashnik *et al.*'s [32] experiments.

Another comparison to ensure accuracy of the absorption coefficient is to compare the transmissivity. In Figure 4.3, the transmissivity spectra from experiments from [33] with the current LBL spectra is compared. The LBL spectrum of

transmissivity τ_η cannot be directly calculated using HITEMP, as τ_η is a function of path length. Hence, the transmissivity spectrum is obtained through the relation $\tau_\eta = e^{-\kappa_\eta L}$, where L is the path length (or the beam length). In experiments in [33], the medium temperature $T = 1550$ K, total pressure $p = 1$ atm., H_2O mole fraction is unity, and path length $L = 0.4$ m. It can be seen in Figure 4.3 that the experimental and LBL spectra show good agreement in capturing both the bands and the windows of the H_2O transmissivity spectrum. However, the experiments in [33] suffer from low spectral resolution in the vicinity of band troughs (or peaks in absorption coefficient).

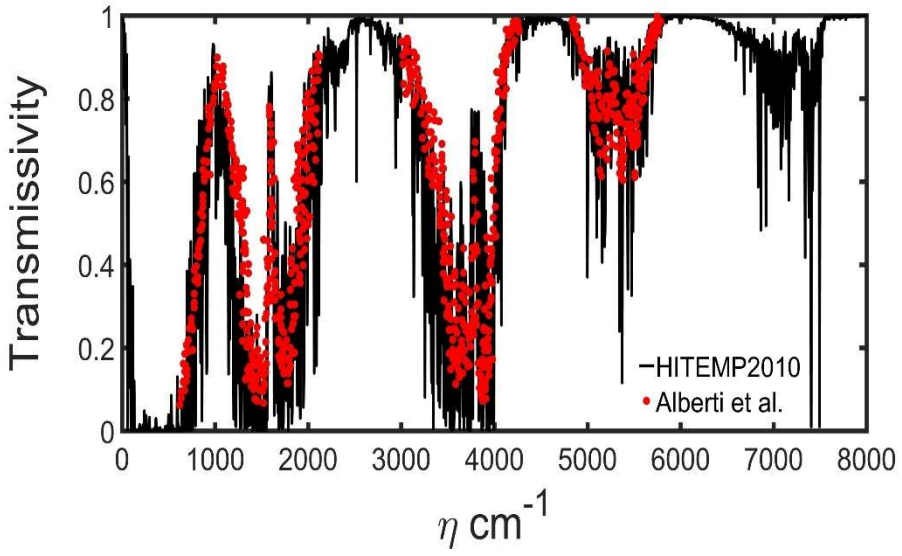

Figure 4.3 Comparison of experimental [24] and LBL transmissivity spectra of H2O at $T = 1550$ K, $p = 1$ atm., H2O mole fraction of unity, and path length $L = 0.4$ m.

4.4 Line-by-Line Absorption Coefficient Calculation Results

Based on the calculations in section 4.2, the following figures show the spectral absorption coefficient as a function of wavenumber. The figures not only present the spectral absorption coefficient from HITEMP 2010 (referred to as LBL in the plots), but also shows the comparison of each model as described in Chapter 1.

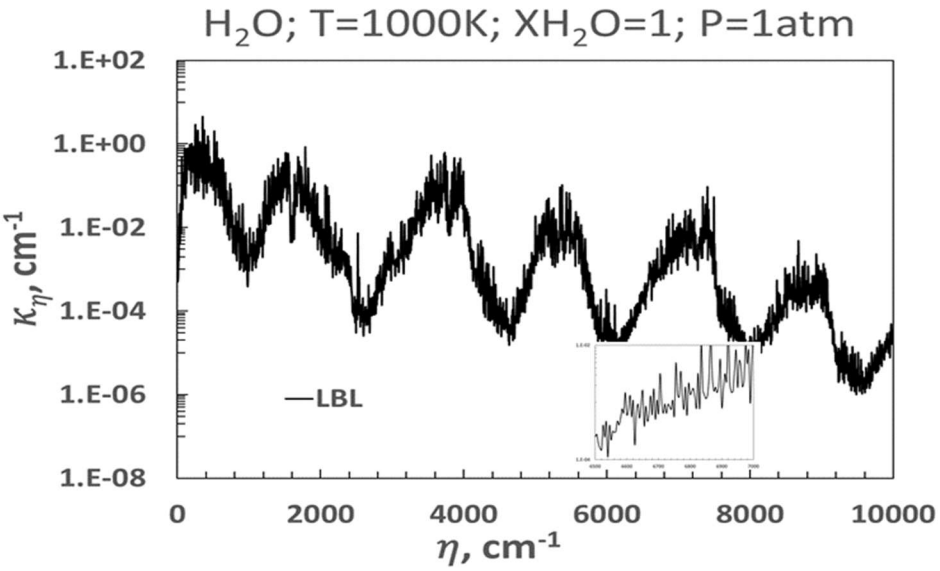

Figure 4.4 Spectral absorption coefficient of H_2O at $T = 1000$ K, mole fraction of 1, and $p = 1$ atm. calculated from HITEMP 2010 with $\Delta\eta$ = 0.005 cm^{-1}. Inset is a zoomed-in portion of the spectrum to show the details of the spectrum.

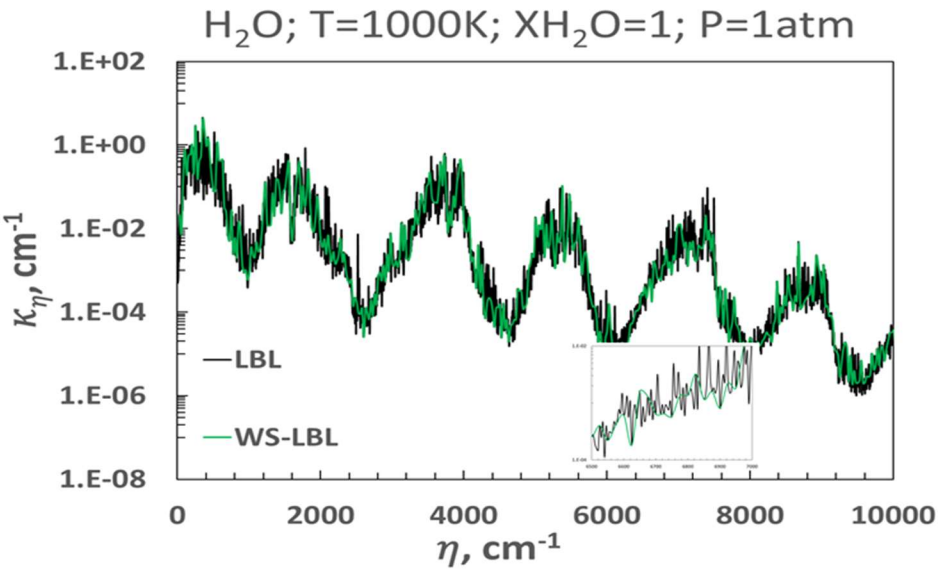

Figure 4.5 Comparison of the spectral absorption coefficient (black line) and the WS-LBL method (green line) of H_2O at $T = 1000$ K, mole fraction of 1, and $p = 1$ atm. calculated from HITEMP 2010 with $\Delta\eta$ = 0.005 cm^{-1}. Green line shows the WS-LBL method, with discrete points taken at every 25 cm^{-1}. Inset is a zoomed-in portion of the spectrum to show the details of the spectrum.

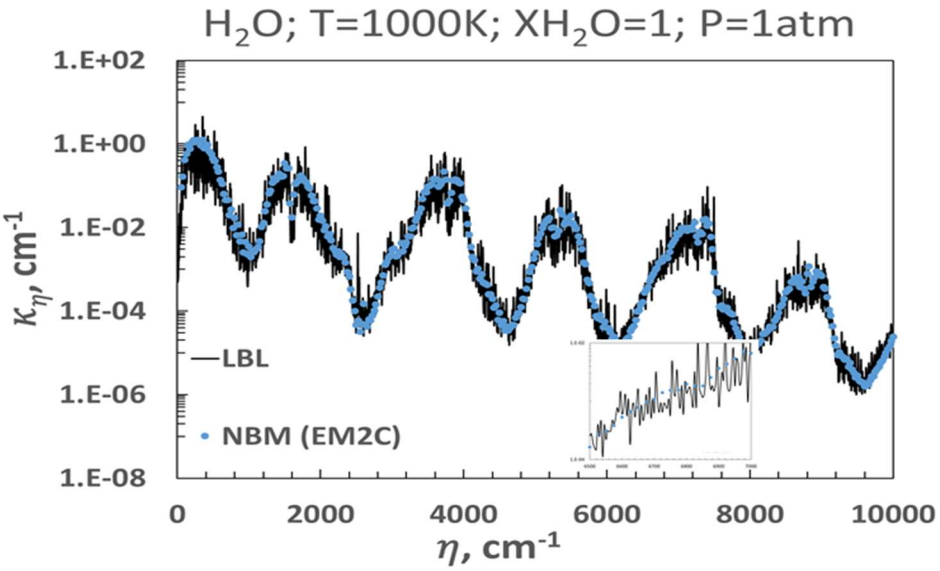

Figure 4.6 Comparison of the spectral absorption coefficient (black line) and the EM2C NBM (blue dots) of H_2O at $T = 1000$ K, mole fraction of 1, and $p = 1$ atm. calculated from HITEMP 2010 with $\Delta\eta$ = 0.005 cm^{-1}. Inset is a zoomed-in portion of the spectrum to show the details of the spectrum.

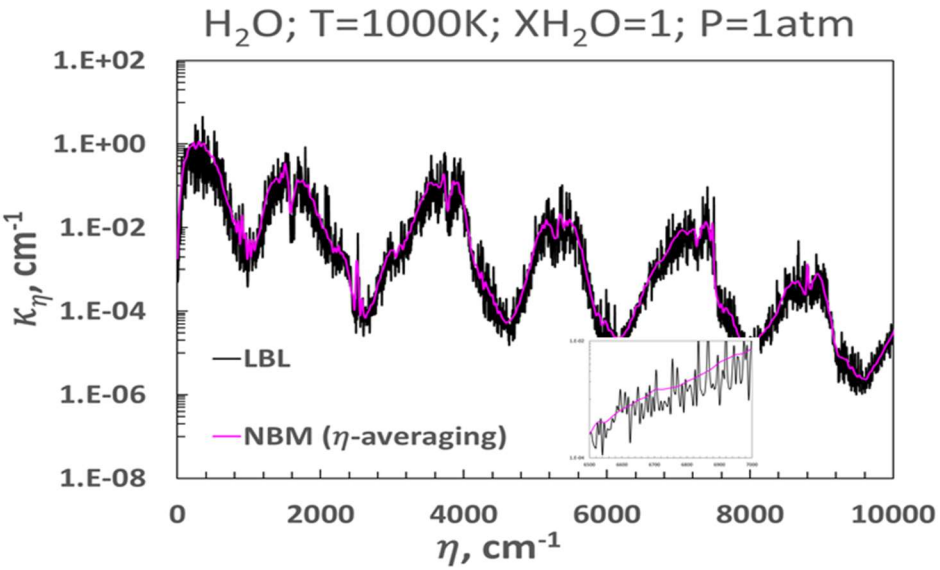

Figure 4.7 Comparison of the spectral absorption coefficient (black line) and the η-averaging NBM (pink line) of H_2O at $T = 1000$ K, mole fraction of 1, and $p = 1$ atm. calculated from HITEMP 2010 with $\Delta\eta$ = 0.005 cm^{-1}. Pink line shows the η-averaging NBM at every 25 cm^{-1}. Inset is a zoomed-in portion of the spectrum to show the details of the spectrum.

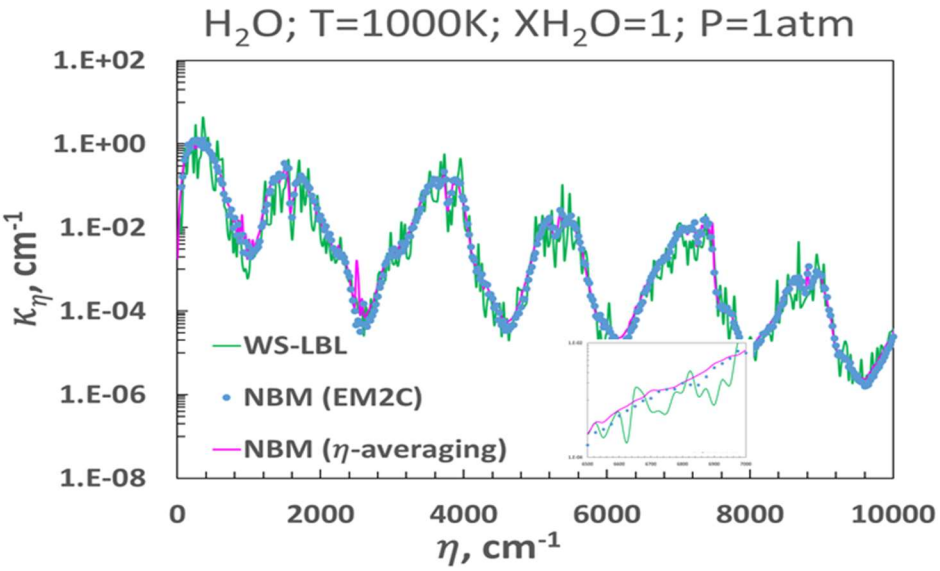

Figure 4.8 Comparison of the spectral absorption coefficient from the models and WS-LBL method of H_2O at $T = 1000$ K, mole fraction of 1, and $p = 1$ atm. Inset is a zoomed-in portion to show the details of the spectrum.

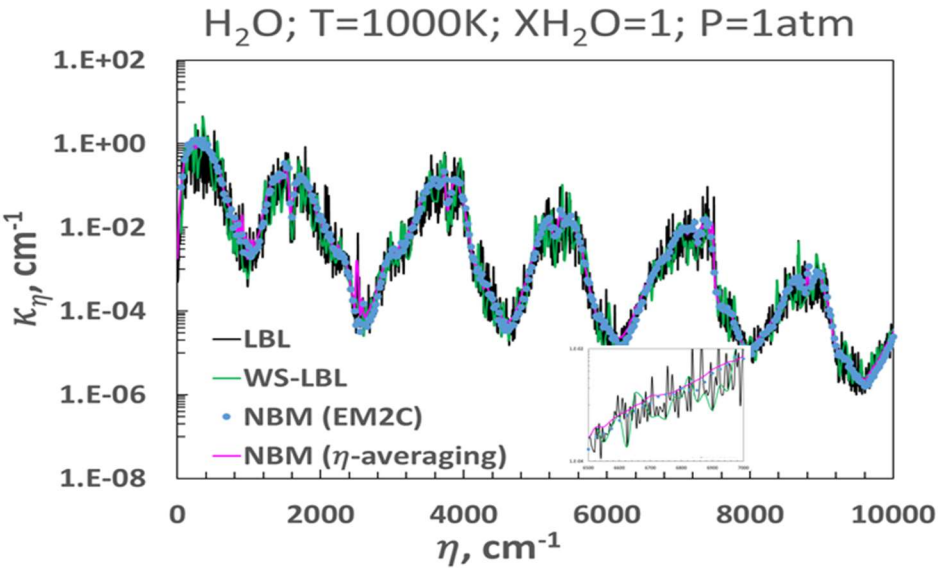

Figure 4.9 Comparison of the spectral absorption coefficient from LBL, WS-LBL method, and models of H_2O at $T = 1000$ K, mole fraction of 1, and $p = 1$ atm. Inset is a zoomed-in portion to show the details of the spectrum.

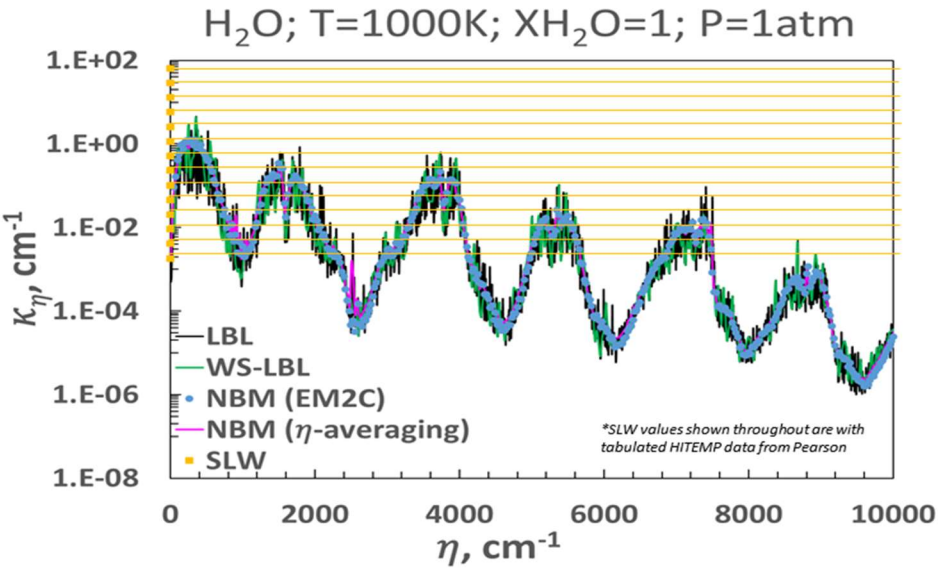

Figure 4.10 Comparison of the spectral absorption coefficient from LBL, WS-LBL method, models, and SLW of H_2O at $T = 1000$ K, mole fraction of 1, and $p = 1$ atm.

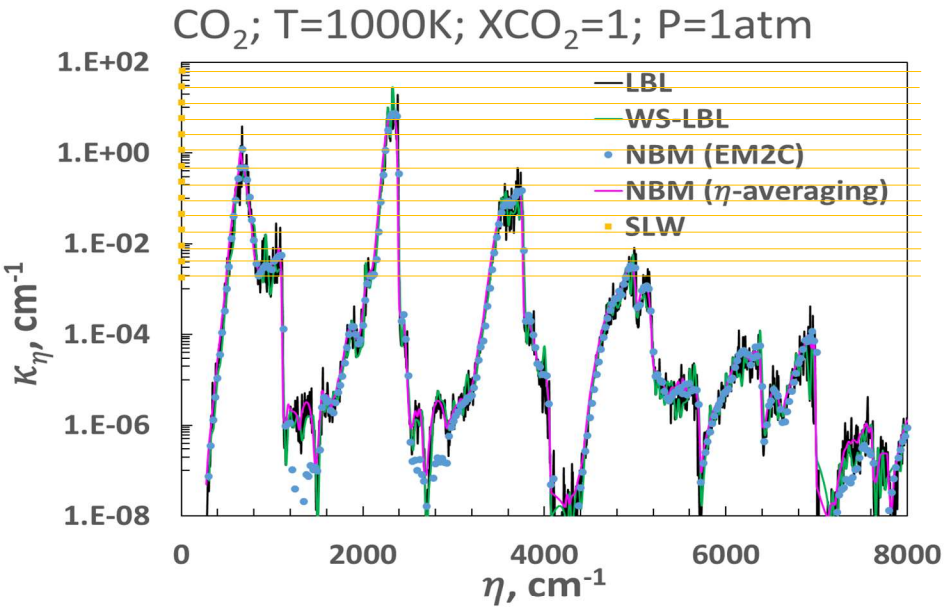

Figure 4.11 Comparison of the spectral absorption coefficient from LBL, WS-LBL method, models, and SLW of CO_2 at $T = 1000$ K, mole fraction of 1, and $p = 1$ atm.

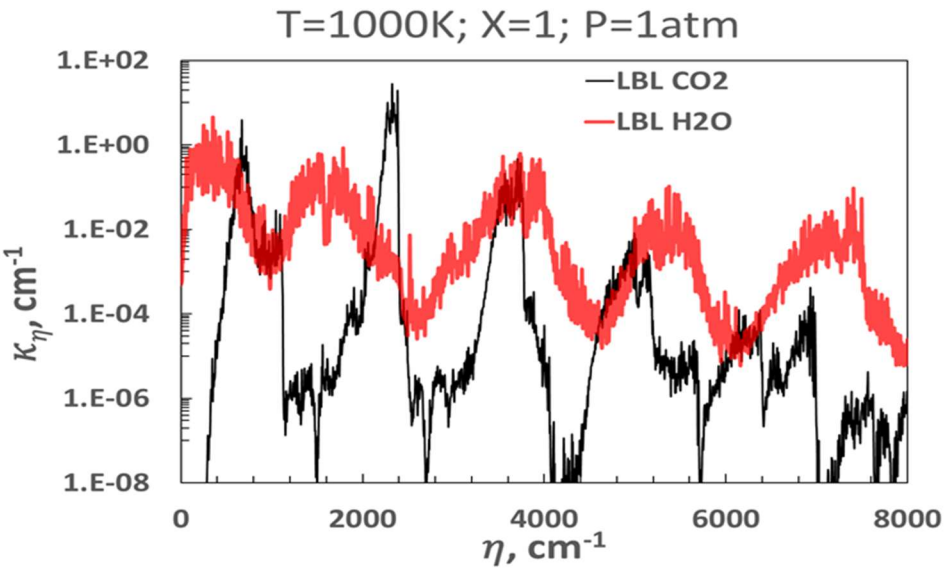

Figure 4.12 Comparison of the spectral absorption coefficient from HITEMP 2010 of H_2O (red line) and CO_2 (black line) at $T = 1000$ K, mole fraction of 1, and $p = 1$ atm.

4.5 Dependencies of Temperature, Pressure, and Mole Fraction

The absorption coefficient is dependent on temperature, pressure, and mole fraction, as seen in section 4.2. The absorption coefficient is also linearly dependent on the absorption cross-section, therefore in the following section, the absorption coefficient will be presented with varying temperature, pressure, and mole fraction.

4.5.1 Effects of Temperature

In general, the absorption cross-section and absorption coefficient increases with increasing gas temperature, which indicates gas absorption increases with increasing gas temperature. At a molecular level, [43, 45] explains this phenomenon and why this occurs, specifically in relation with the broadening effects.

In the following figures, it is noted that, the higher the temperature, the lower the peaks, but also the more spread out the data are. This effect is because of the band peaks decreasing due to higher vibrational states that become more probable with higher temperatures. The broadening increases with higher temperature because the largest

population of rotational energy states shift higher as temperature increases, and vibrational energy transition at higher energy states happens at higher temperatures [43]. More detailed explanations at the molecular level and the broadening mechanisms on the temperature dependance can be found in [43].

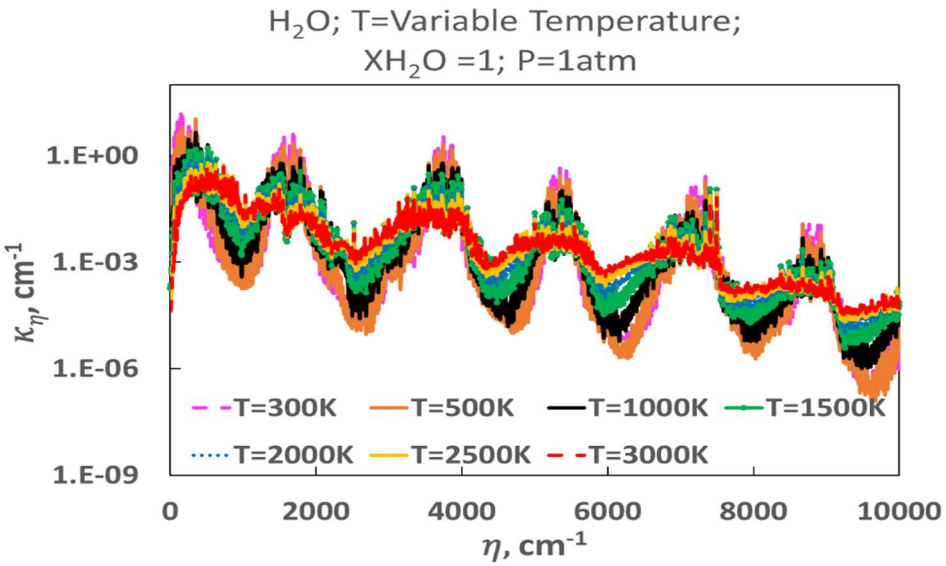

Figure 4.13 Comparison of the spectral absorption coefficient from HITEMP 2010 of H_2O at variable temperatures, mole fraction of 1, and $p = 1$ atm.

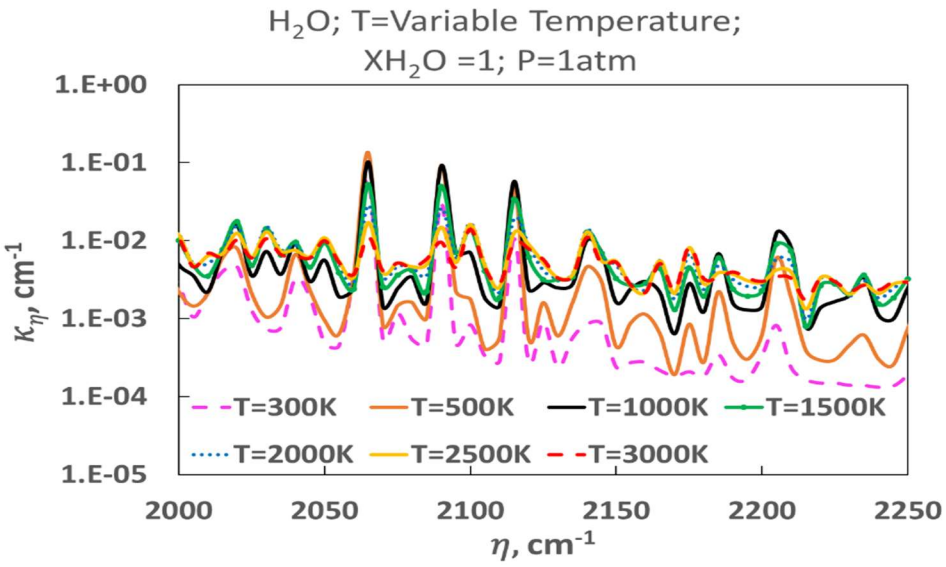

Figure 4.14 Zoomed-in comparison of the spectral absorption coefficient from HITEMP 2010 of H_2O at variable temperatures, mole fraction of 1, and $p = 1$ atm.

4.5.2 Effects of Pressure

In the following figures, it can be seen that the higher the pressure, the more smoothed/broadened the line. The effects of pressure on the absorption coefficient are detailed in [5]. From the calculations in section 4.2, the total pressure dependence of the absorption cross-section is felt through the Lorentz half-width, and, while less, through line location. The dependence of the spectral absorption coefficient on total pressure is dependent on the influence of total pressure on the absorption cross-section [5].

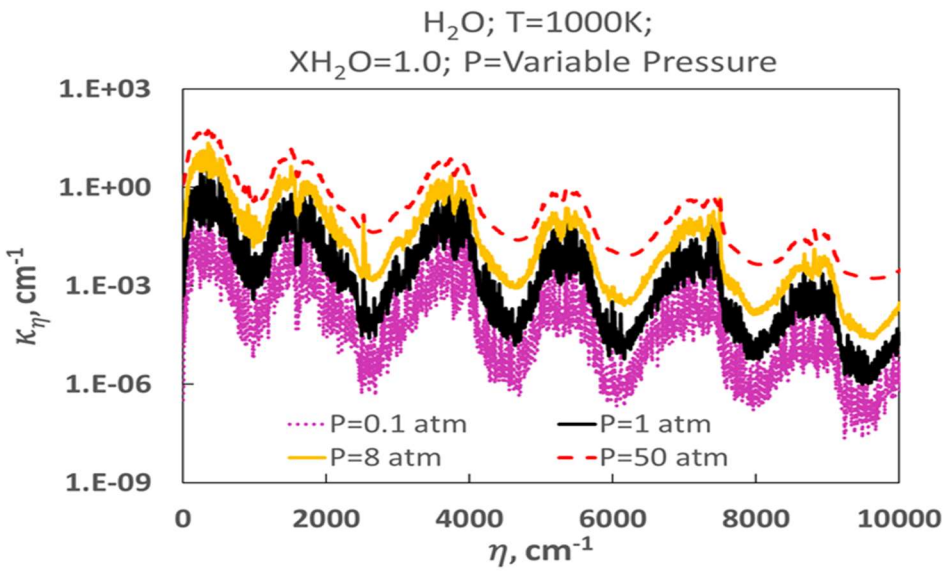

Figure 4.15 Comparison of the spectral absorption coefficient from HITEMP 2010 of H_2O at $T = 1000$ K, mole fraction of 1, and variable pressure.

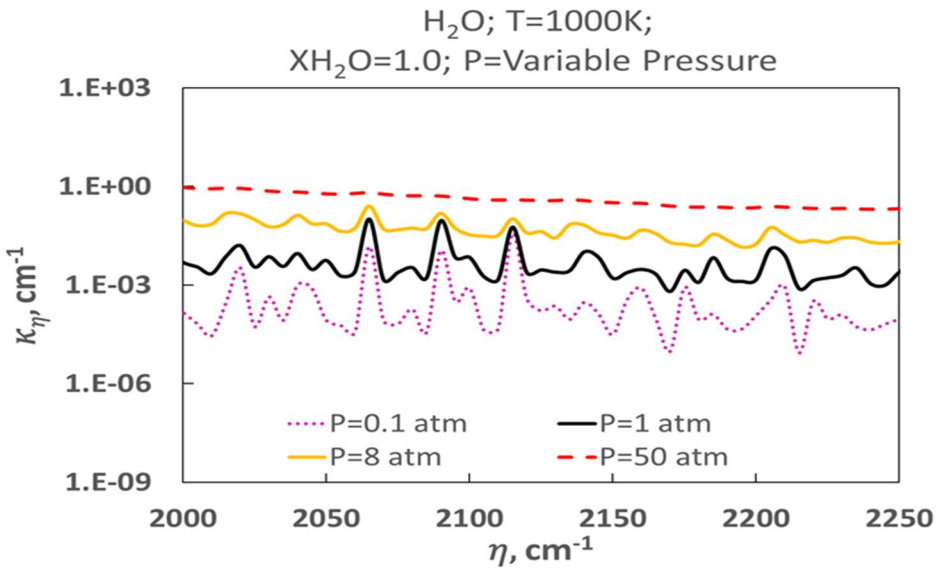

Figure 4.16 Zoomed-in comparison of the spectral absorption coefficient from HITEMP 2010 of H_2O at $T = 1000$ K, mole fraction of 1, and variable pressure.

4.5.3 Effects of Mole Fraction

The product of molar density and mole fraction is dependent only on partial pressure [5]. In observing the mole fraction variances, the absorption coefficient results do not seem to significantly change, although there is larger variation with the smaller mole fraction absorption coefficient.

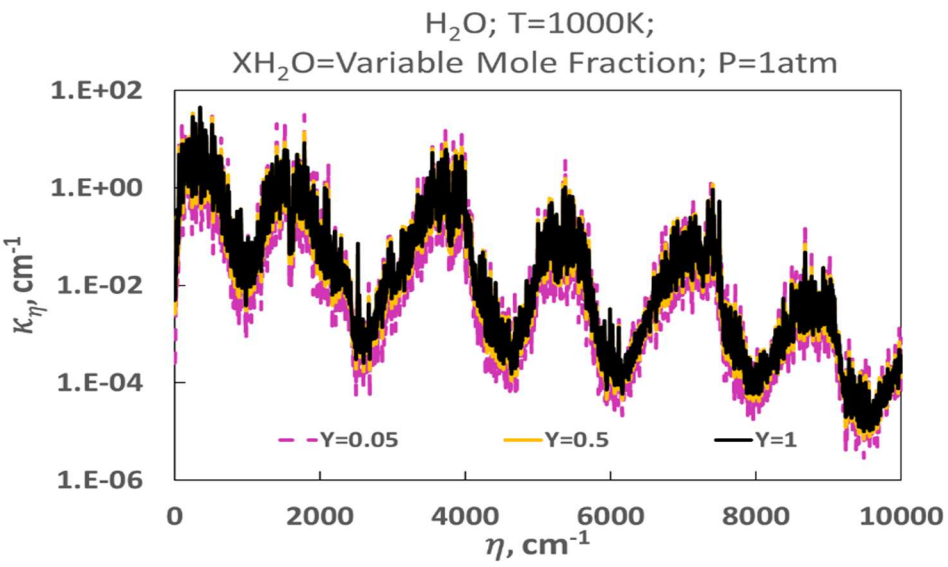

Figure 4.17 Comparison of the spectral absorption coefficient from HITEMP 2010 of H_2O at $T = 1000$ K, variable mole fraction, and $p = 1$ atm.

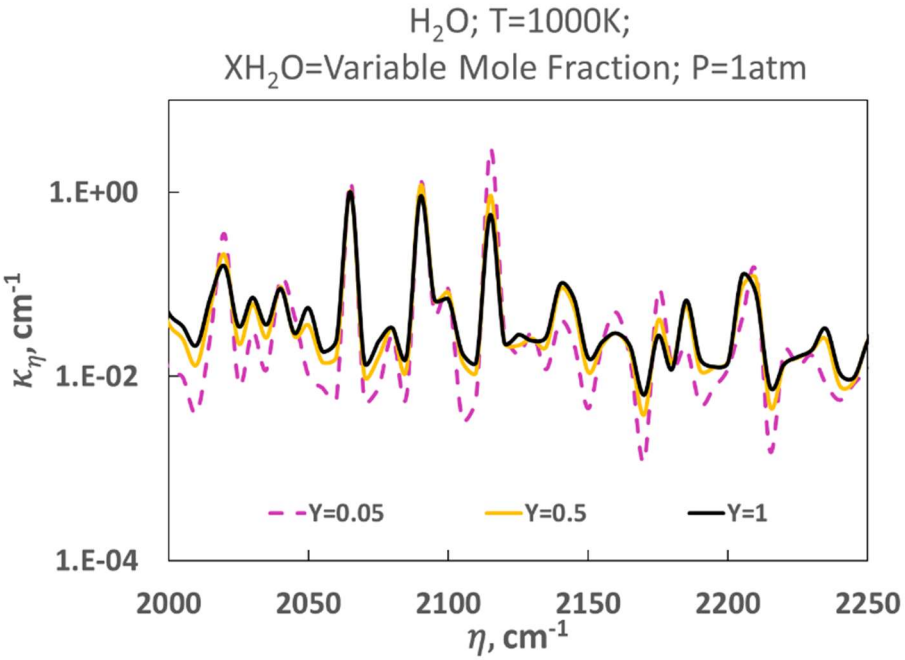

Figure 4.18 Zoomed-in comparison of the spectral absorption coefficient from HITEMP 2010 of H_2O at $T = 1000$ K, variable mole fraction, and $p = 1$ atm.

References

[1] H. Harde, "Radiation and Heat Transfer in the Atmosphere: A Comprehensive Approach on a Molecular Basis," *International Journal of Atmospheric Sciences,* vol. 2013, 2013.

[2] D. Frankman, B. W. Webb, B. W. Butler, D. Jimenez, J. M. Forthofer, P. Sopko, K. S. Shannon, J. K. Hiers and R. D. Ottmar, "Measurements of convective and radiative heating in wildland fires," *International Journal of Wildland Fire,* vol. 22, no. 2, 2013.

[3] H. Chu, F. Liu and H. Zhou, "Calculations of Gas Thermal Radiation Transfer in One-Dimensional Planar Enclosure Using LBL and SNB Models," *International Journal of Heat and Mass Transfer,* vol. 54, pp. 4736-4745, 2011.

[4] A. Fisher, "Development of Absorption Coefficient-Based Narrow Band Model and its Application to the Calculation of Radiative Heat Transfer in One- and Two- Dimensional Enclosures," Ph.D. Dissertation, Huntsville, Alabama, 2018.

[5] J. T. Pearson, "The Development of Updated and Improved SLW Model Parameters and Its Applications to Comprehensive Combustion Predictions," Brigham Young University, Provo, Utah, 2013.

[6] L. S. Rothman, "The HITRAN2012 molecular spectroscopic database," *Journal of Quantitative Spectroscopy & Radiative Transfer,* vol. 130, pp. 4-50, 2013.

[7] L. S. Rothman, "HITEMP, the high-temperature molecular spectroscopic database," *Journal of Quantitative Spectroscopy & Radiative Transfer,* vol. 111, pp. 2139-2150, 2010.

[8] M. F. Modest, Radiative Heat Transfer, 3rd ed., Academic Press, 2013.

[9] W. M. Elsasser, Heat transfer by infrared radiation in the atmosphere, Cambridge, MA: Harvard University Press, 1943.

[10] R. M. Goody, "A statistical model for water-vapour absorption," *Quarterly Journal of the Royal Meteorological Society,* vol. 78, no. 336, pp. 165-169, 1952.

[11] W. Malkmus, "Random Lorentz Band Model with Exponential-Tailed S^-1 Line Intensity Distribution Function," *Journal of the Optical Society of America,* vol. 57, no. 3, pp. 323-329, 1967.

[12] K.-Y. Chien, "Application of the mean absoprtion coefficient in nonisothermal infrared radiating gases," *Journal of Quantitative Spectroscopy and Radiative Transfer,* vol. 12, pp. 379-386, 1972.

[13] D. K. Edwards, "Molecular Gas Band Radiation," *Advances in Heat Transfer,* vol. 12, pp. 115-193, 1976.

[14] F. Andre and R. Vaillon, "A nonuniform narrow band correlated-k approximation using the k-moment method," *Journal of Quantitative Spectroscopy & RadiativeTransfer,* vol. 111, pp. 1900-1911, 2010.

[15] S. J. Young, Band Model Theory of Radiation Transport, El Segundo, California: The Aerospace Press, 2013.

[16] J. Chai, S. Patankar and H. Lee, "Evaluation of Spatial Differencing Practices for the Discrete-Ordinates Method," *Journal of Thermophysics and Heat Transfer,* vol. 8, no. 1, pp. 140-144, 1994.

[17] A. Soufiani and E. Djavdan, "A Comparison between Weighted Sum of Gray Gases and Statistical Narrow-Band Radiation Models for Combustion Applications," *Combustion and Flame,* vol. 97, pp. 240-250, 1994.

[18] P. Riviere, S. Langlois, A. Soufiani and J. Taine, "An Approximate Database of H2O Infrared Lines for High Temperature Applications at Low Resolution Statistical Narrow-Band Model Parameters," *Journal of Quantitative Spectroscopic Radiative Transfer,* vol. 53, no. 2, pp. 221-224, 1995.

[19] P. Riviere and A. Soufiani, "Updated Band Model Parameters for H2O, CO2, CH4, and CO Radiation at High Temperature," *International Journal of Heat and Mass Transfer,* vol. 55, pp. 3348-3358, 2012.

[20] C. B. Ludwig, W. Malkmus, J. E. Reardon and J. A. L. Thomson, Handbook of Infrared Radiation from Combustion Gases, Washington, D. C.: National Aeronautics and Space Administration, 1973.

[21] M. K. Denison and B. W. Webb, "A Spectral Line-Based Weighted-Sum-of-Gray-Gases Model for Arbitrary RTE Solvers," *Journal of Heat Transfer,* vol. 115, pp. 1004-1012, 1993.

[22] M. K. Denison and B. W. Webb, "The Spectral Line-Based Weighted-Sum-of-Gray-Gases Model in Nonisothermal Nonhomogeneous Media," *Journal of Heat Transfer,* vol. 117, pp. 359-365, 1995.

[23] J. T. Pearson, B. W. Webb, V. P. Solovjov and J. Ma, "Updated correlation of the absorption line blackbody distribution function for H2O based on the HITEMP 2010 database," *Journal of Quantitative Spectroscopy and Radiative Transfer,* vol. 128, pp. 10-17, 2013.

[24] J. T. Pearson, B. W. Webb, V. P. Solovjov and J. Ma, "Efficient representation of the absorption line blackbody distribution function for H2O, CO2, and CO at variable temperature, mole fraction, and total pressure," *Journal of Quantitative Spectroscopy and Radiative Transfer,* vol. 138, pp. 82-96, 2014.

[25] V. Solovjov and F. Andre, "Global Models for Gas Radiation," 2017.

[26] V. P. Solovjov and B. W. Webb, "SLW modeling of radiative transfer in multicomponent gas mixtures," *Journal of Quantitative Spectroscopy & Radiative Transfer,* vol. 65, pp. 655-672, 2000.

[27] M. K. Denison and B. W. Webb, "The Spectral-Line Weighted-Sum-of-Gray-Gases Model for H2O/CO2 Mixtures," *ASME Journal of Heat Transfer,* vol. 117, no. 3, pp. 788-792, 1995.

[28] B. V. S. A. F. Webb, "The Spectral Line Weighted-sum-of-gray-gases (SLW) Model for Prediction of Radiative Transfer in Molecular Gases," in *Advances in Heat Transfer*, Academic Press, 2019, pp. 207-298.

[29] F. Liu, H. A. Becker and A. Pollard, "Spatial Differencing Schemes of the Discrete-Ordinates Method," *Numerical Heat Transfer: Part B,* vol. 30, pp. 23-43, 1996.

[30] J. C. Chai, H. S. Lee and S. V. Patankar, "Finite Volume Method for Radiation Heat Transfer," *Journal of Thermophysics and Heat Transfer,* vol. 8, no. 3, pp. 419-425, 1994.

[31] T. Kim, J. Menart and H. Lee, "Nongray Radiative Gas Analysis Using the S-N Discrete Ordinates Method," *Journal of Heat Transfer,* vol. 113, pp. 946-952, 1991.

[32] Ptashnik, "Near-infrared water vapour self-continuum at close to room temperature," *Journal of Quantitative Spectroscopy & Radiative Transfer,* vol. 120, pp. 23-25, 2013.

[33] M. Alberti, "Comparison of models for predicting band emissivity of carbon dioxide and water vapour at high temperatures," *International Journal of Heat and Mass Transfer,* vol. 64, pp. 910-925, 2013.

[34] H. Chu, F. Liu and H. Zhou, "Calculations of Gas Thermal Radiation Transfer in Two-Dimensional Rectangular Enclosure Using the Line-by-Line Approach and the Statistical Narrow-Band Correlated-k Model," *International Journal of Thermal Sciences,* vol. 59, pp. 66-74, 2012.

[35] V. Goutiere, F. Liu and A. Charette, "An Assessment of Real-Gas Modelling in 2-D Enclosures," J*ournal of Quantitative Spectroscopy and Radiative Transfer,* vol. 64, pp. 299-326, 2000.

[36] N. Lallemant and R. Weber, "A computationally efficient procedure for calculating gas radiative properties using the exponential wide band model," *Int. J. Heat Mass Transfer,* vol. 39, no. 15, pp. 3273-3286, 1996.

[37] P. Coelho, "Numerical simulation of radiative heat transfer from non-gray gases in three-dimensional enclosures," *J. Quant. Spectrosc. Radiat. Transfer,* vol. 74, no. 3, pp. 307-328, 2002.

[38] V. Goutiere, A. Charette and L. Kiss, "Comparative performance of nongray gas modeling techniques," *Numer. Heat Transfer, Part B Fundam.,* vol. 41, no. 3-4, pp. 361-381, 2002.

[39] A. Fisher and S. L. Rani, "A Narrow Band Model Based on the Absorption Coefficient and its Application to the Calculation of Radiative Transfer in One Dimensional Enclosures," *Journal of Quantitative Spectroscopy and Radiative Transfer,* vol. 277, 2022.

[40] Caliot, C., "Numerical Methods in Radiative Transfer: Introduction to DOM, FVM, and MCM," PROMES-CNRS Lab, 2010.

[41] T. G. Kyle, Atmospheric Transmission, Emission, and Scattering, Pergamon Press, 1991.

[42] G. W. Petty, A First Course in Atmospheric Radiation, 2nd ed., Sundog Publishing, 2006.

[43] K. Wakatsuki, "High Temperature Radiation Absorption of Fuel Molecules and an Evaluation of Its Influence on Pool Fire Modeling," University of Maryland, College Park, College Park, Maryland, 2005.

[44] M. Alberti, R. Weber, M. Mancini, A. Fateev and S. Clausen, "On the Accuracy of HITEMP-2010 Calculated Emisivities of Water Vapor and Carbon Dioxide," Proceedings of the 10th European Conference on Industrial Furnaces and Boilers, 2015.

[45] M. K. Denison, "A Spectral Line-Based Weighted-Sum-of-Gray-Gases Model for Arbitrary RTE Solvers," Brigham Young University, Provo, Utah, 1994.

[46] L. S. Rothman, C.P. Rinsland, A. Goldman S.T. Massie, D.P. Edwards, J-M. Flaud, A. Perrin, C. Camy-Peyret, V. Dane, J.-Y. Mandin, J. Schroeder, A. McCann, R.R. Gamache, R.B. Wattson, K. Yoshino, K.V. Chance, K.W. Jucks, L.R. Brown, V. Nemthinov, P. Varansai,. "The HITRAN Molecular Spectroscopic Database and Hawks (HITRAN Atmospheric Workstation): 1996 Edition," Journal of Quantitative Spectroscopy & Radiative Transfer, vol. 60, issue 5, pp. 665-710, 1998.